Color figures from Rappaport et al., *Millimeter Wave Wireless Communications* (ISBN-13: 9780132172288)

Note: Only selected figures in the book are available in color. Black and white figures have been omitted from this file.

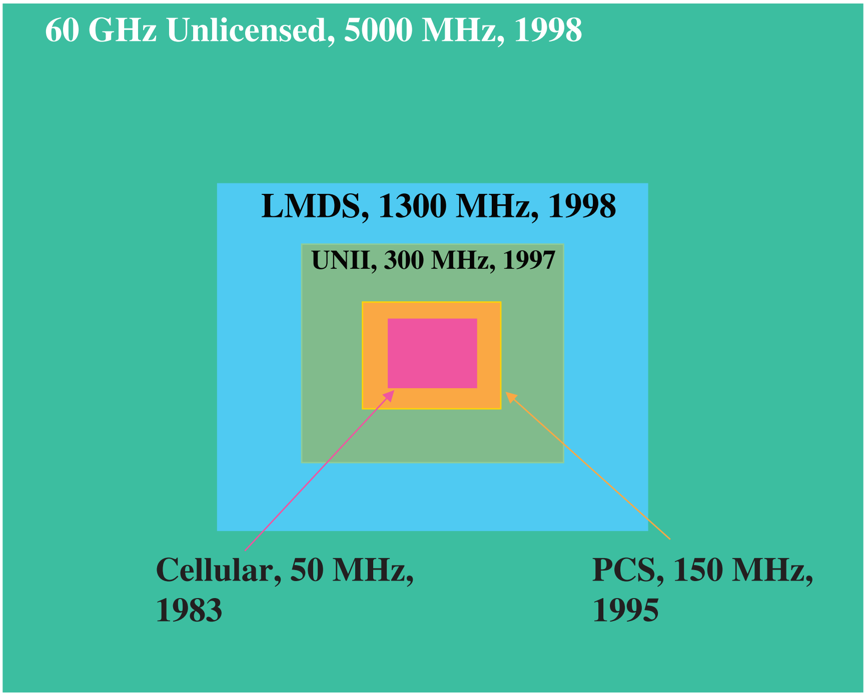

Figure 1.1 Areas of the squares illustrate the available licensed and unlicensed spectrum bandwidths in popular UHF, microwave, 28 GHz LMDS, and 60 GHz mmWave bands in the USA. Other countries around the world have similar spectrum allocations [from [Rap02]].

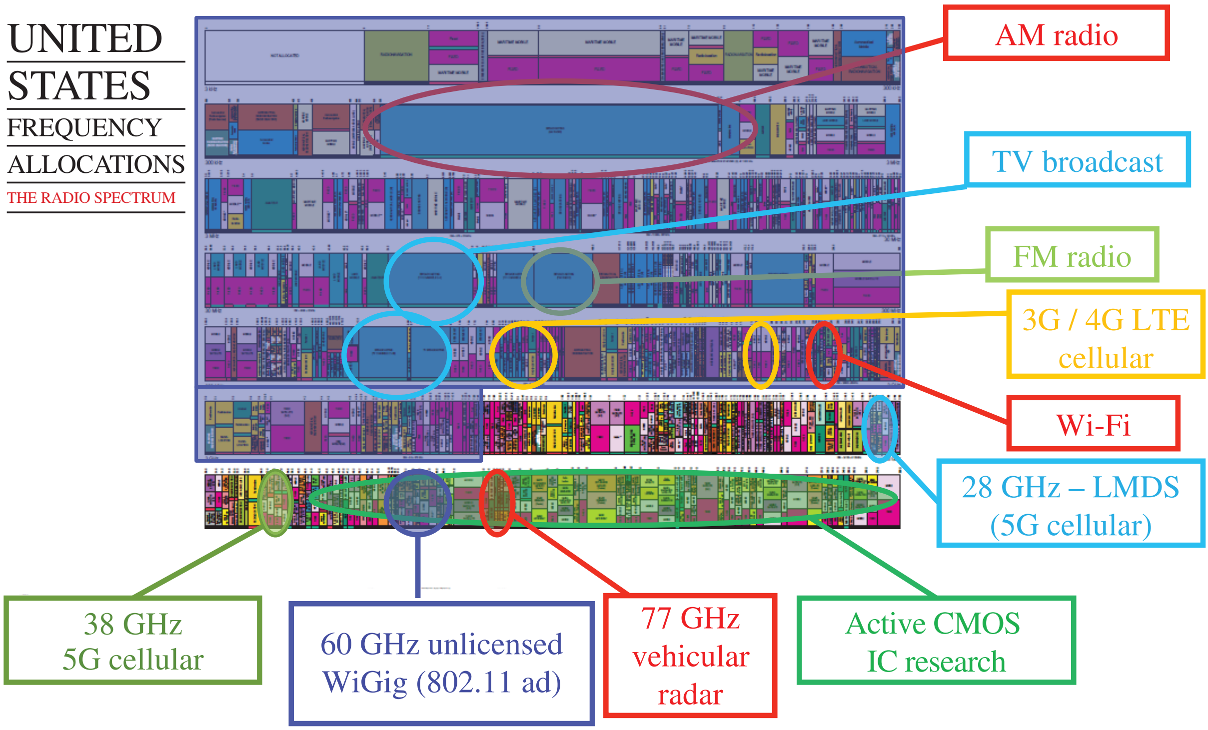

Figure 1.2 Wireless spectrum used by commercial systems in the USA. Each row represents a decade in frequency. For example, today's 3G and 4G cellular and WiFi carrier frequencies are mostly in between 300 MHz and 3000 MHz, located on the fifth row. Other countries around the world have similar spectrum allocations. Note how the bandwidth of all modern wireless systems (through the first 6 rows) easily fits into the unlicensed 60 GHz band on the bottom row [from [Rap12b] U.S. Dept. of Commerce, NTIA Office of Spectrum Management].

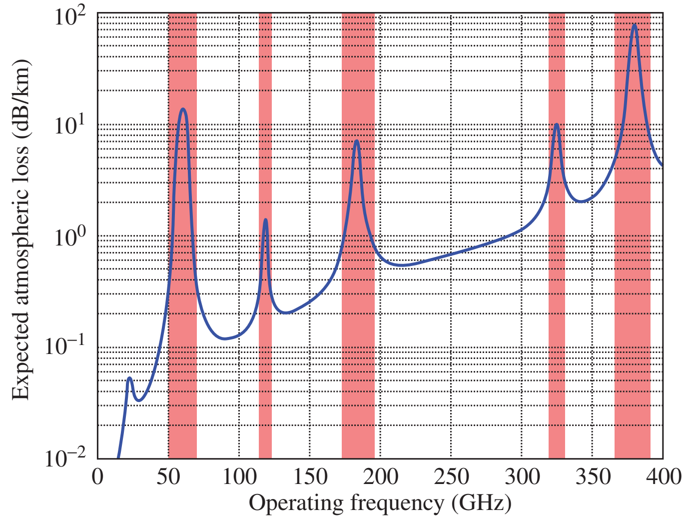

Figure 1.3 Expected atmospheric path loss as a function of frequency under normal atmospheric conditions (101 kPa total air pressure, 22° Celsius air temperature, 10% relative humidity, and 0 g/m^3 suspended water droplet concentration) [Lie89]. Note that atmospheric oxygen interacts strongly with electromagnetic waves at 60 GHz. Other carrier frequencies, in dark shading, exhibit strong attenuation peaks due to atmospheric interactions, making them suitable for future short-range applications or "whisper radio" applications where transmissions die out quickly with distance. These bands may service applications similar to 60 GHz with even higher bandwidth, illustrating the future of short-range wireless technologies. It is worth noting, however, that other frequency bands, such as the 20-50 GHz, 70-90 GHz, and 120-160 GHz bands, have very little attenuation, well below 1 dB/km, making them suitable for longer-distance mobile or backhaul communications.

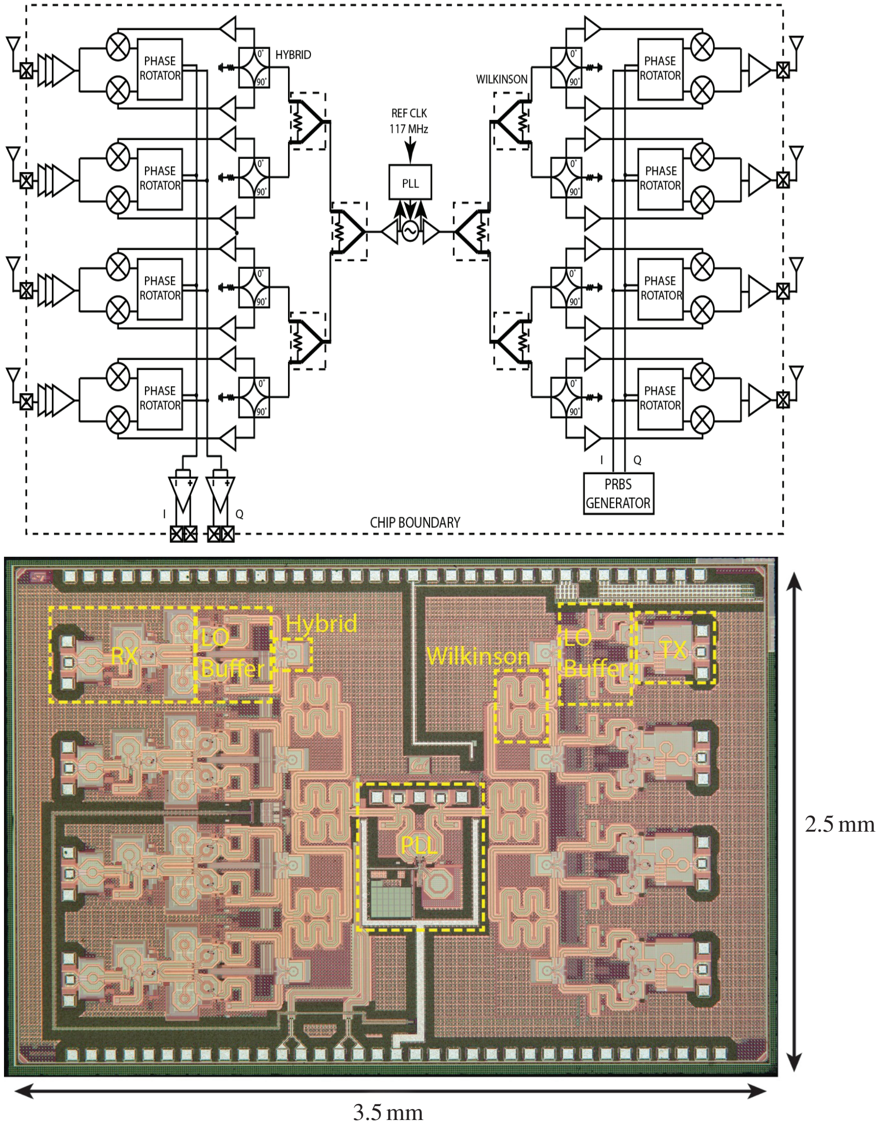

Figure 1.4 Block diagram (top) and die photo (bottom) of an integrated circuit with four transmit and receive channels, including the voltage-controlled oscillator, phase-locked loop, and local oscillator distribution network. Beamforming is performed in analog at baseband. Each receiver channel contains a low noise amplifier, inphase/quadrature mixer, and baseband phase rotator. The transmit channel also contains a baseband phase rotator, up-conversion mixers, and power amplifiers. Figure from [TCM+11], courtesy of Prof. Niknejad and Prof. Alon of the Berkeley Wireless Research Center [© IEEE].

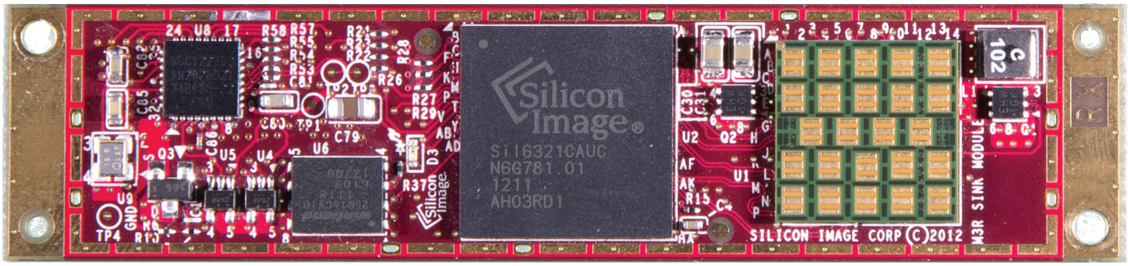

Figure 1.5 Third-generation 60 GHz WirelessHD chipset by Silicon Image, including the SiI6320 HRTX Network Processor, SiI6321 HRRX Network Processor, and SiI6310 HRTR RF Transceiver. These chipsets are used in real-time, low-latency applications such as gaming and video, and provide 3.8 Gbps data rates using a steerable 32 element phased array antenna system (courtesy of Silicon Image) [EWA+11] [© IEEE].

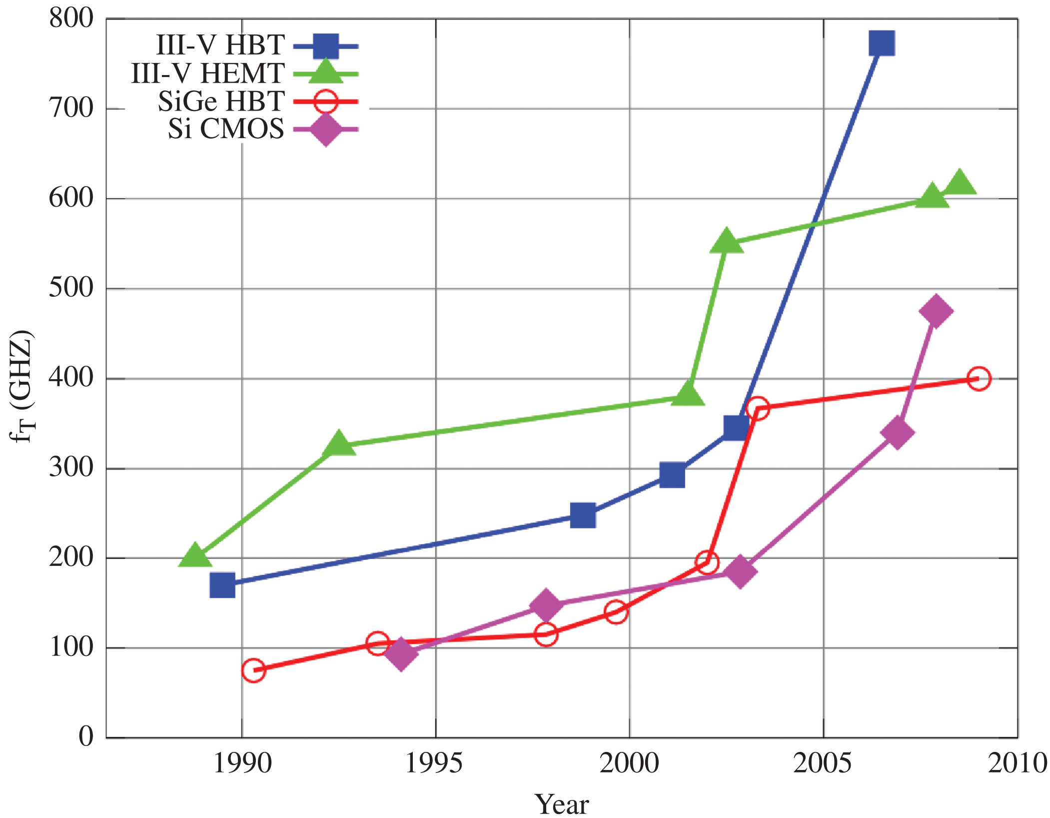

Figure 1.6 Achievable transit frequency (f_T) of transistors over time for several semiconductor technologies, including silicon CMOS transistors, silicon germanium heterojunction bipolar transistor (SiGe HBT), and certain other III-V high electron mobility transistors (HEMT) and III-V HBTs. Over the last decade CMOS (the current technology of choice for cutting edge digital and analog circuits) has become competitive with III-V technologies for RF and mmWave applications [figure reproduced from data in [RK09] © IEEE].

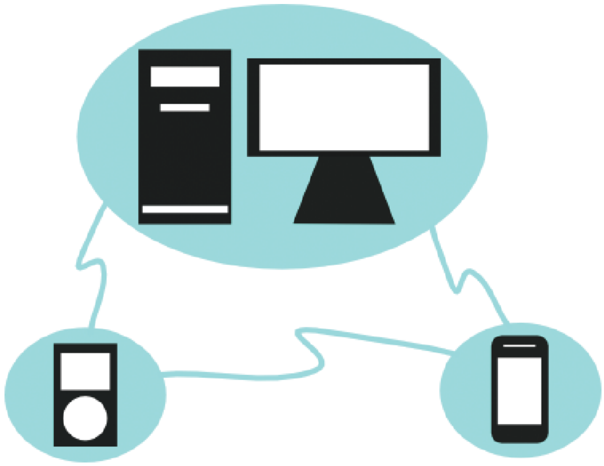

Figure 1.7 Wireless personal area networking. WPANs often connect mobile devices such as mobile phones and multimedia players to each other as well as desktop computers. Increasing the data-rate beyond current WPANs such as Bluetooth and early UWB was the first driving force for 60 GHz solutions. The IEEE 802.15.3c international standard, the WiGig standard (IEEE 802.11ad), and the earlier WirelessHD standard, released in the 2008–2009 time frame, provide a design for short-range data networks (≈ 10 m). All standards, in their first release, guaranteed to provide (under favorable propagation scenarios) multi-Gbps wireless data transfers to support cable replacement of USB, IEEE 1394, and gigabit Ethernet.

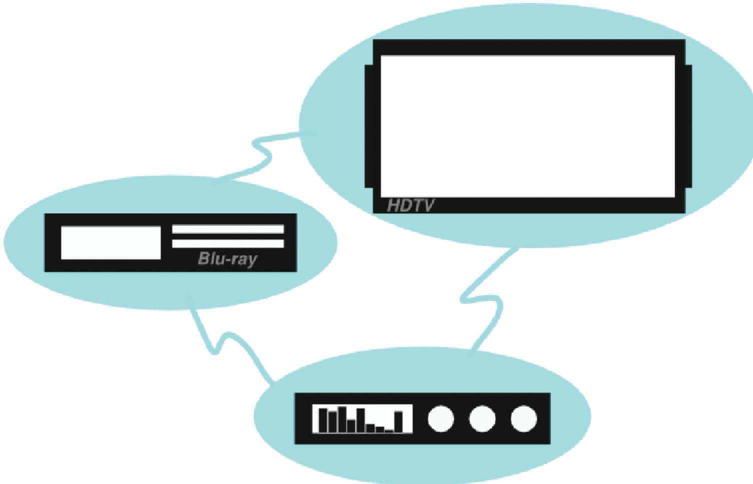

Figure 1.8 Multimedia high-definition (HD) streaming. 60 GHz provides enough spectrum resources to remove HDMI cables without sophisticated joint channel/source coding strategies (e.g., compression), such as in the wireless home digital interface (WHDI) standard that operates at 5 GHz frequencies. Currently, 60 GHz is the only spectrum with sufficient bandwidth to provide a wireless HDMI solution that scales with future HD television technology advancement.

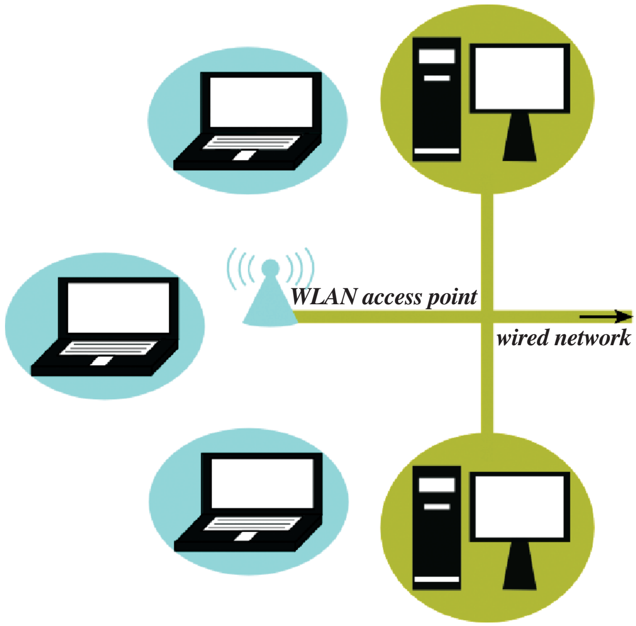

Figure 1.9 Wireless local area networking. WLANs, which typically carry Internet traffic, are a popular application of unlicensed spectrum. WLANs that employ 60 GHz and other mmWave technology provide data rates that are commensurate with gigabit Ethernet. The IEEE 802.11ad and WiGig standards also offer hybrid microwave/mmWave WLAN solutions that use microwave frequencies for normal operation and mmWave frequencies when the 60 GHz path is favorable. Repeaters/relays will be used to provide range and connectivity to additional devices.

Figure 1.10 Wireless backhaul and relays may be used to connect multiple cell sites and subscribers together, replacing or augmenting copper or fiber backhaul solutions.

Band	Uplink (MHz)	Downlink (MHz)	Carrier bandwidth (MHz)
700 MHz	746–763	776–793	1.25 5 10 15 20 
AWS	1710–1755	2110–2155	1.25 5 10 15 20 
IMT extension	2500–2570	2620–2690	1.25 5 10 15 20 
GSM 900	880–915	925–960	1.25 5 10 15 20 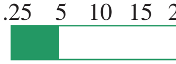
UMTS core	1920–1980	2110–2170	1.25 5 10 15 20 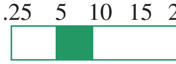
GSM 1800	1710–1785	1805–1880	1.25 5 10 15 20 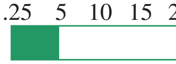
PCS 1900	1850–1910	1930–1990	1.25 5 10 15 20 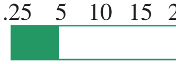
Cellular 850	824–849	869–894	1.25 5 10 15 20 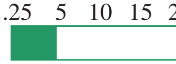
Digital dividend	470–854		1.25 5 10 15 20 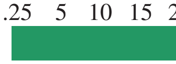

Figure 1.11 United States spectrum and bandwidth allocations for 2G, 3G, and 4G LTE-A (long-term evolution advanced). The global spectrum bandwidth allocation for all cellular technologies does not exceed 780 MHz. Currently, allotted spectrum for operators is dissected into disjoint frequency bands, each of which possesses different radio networks with different propagation characteristics and building penetration losses. Each major wireless provider in each country has, at most, approximately 200 MHz of spectrum across all of the different cellular bands available to them [from [RSM+13] © IEEE].

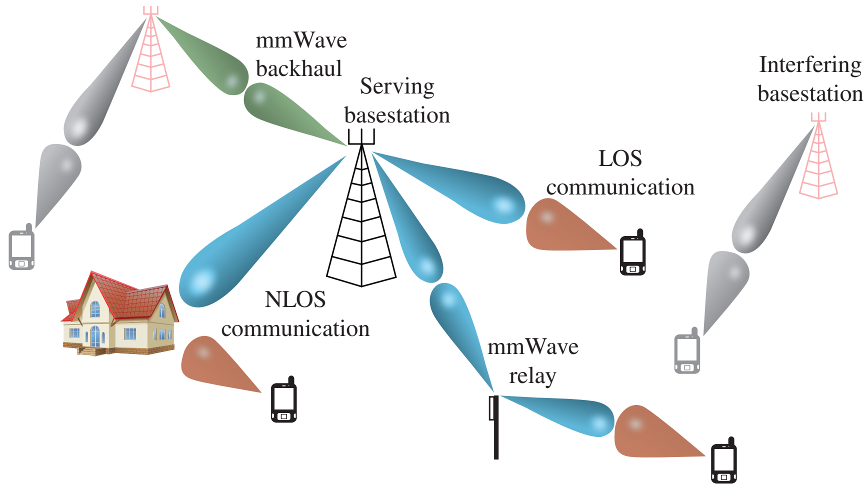

Figure 1.12 Illustration of a mmWave cellular network. Base stations communicate to users (and interfere with other cell users) via LOS, and NLOS communication, either directly or via heterogeneous infrastructure such as mmWave UWB relays.

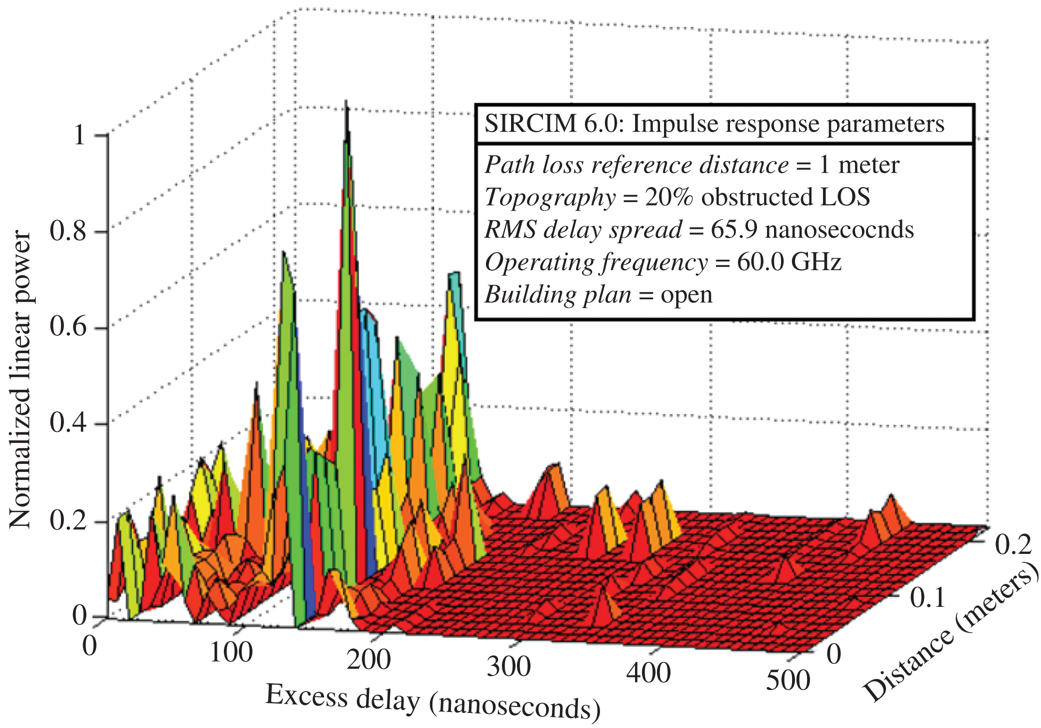

Figure 1.13 Long delay spreads characterize wideband 60 GHz channels and may result in severe inter-symbol interference, unless directional beamforming is employed. Plot generated with Simulation of Indoor Radio Channel Impulse Response Models with Impulse Noise (SIRCIM) 6.0 [from [DMRH10] © IEEE].

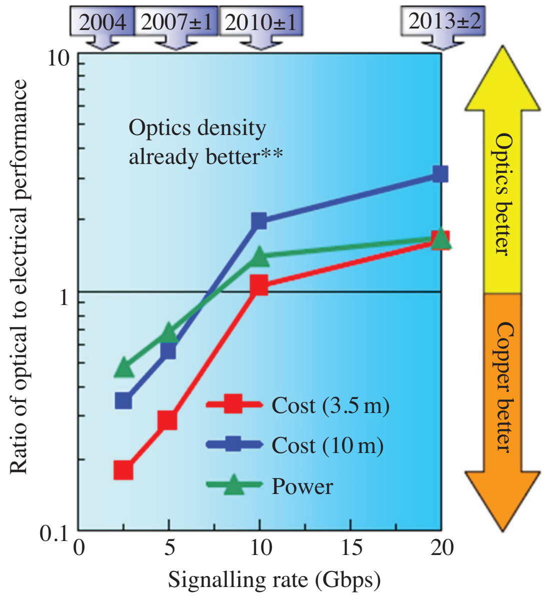

Figure 1.14 Comparison between optical and electrical performance in terms of cost and power for short cabled interconnects. The results show that optical connections are preferred to electrical copper connections for higher data rates, assuming wires are used [adapted from [PDK$^+$07] © IEEE].

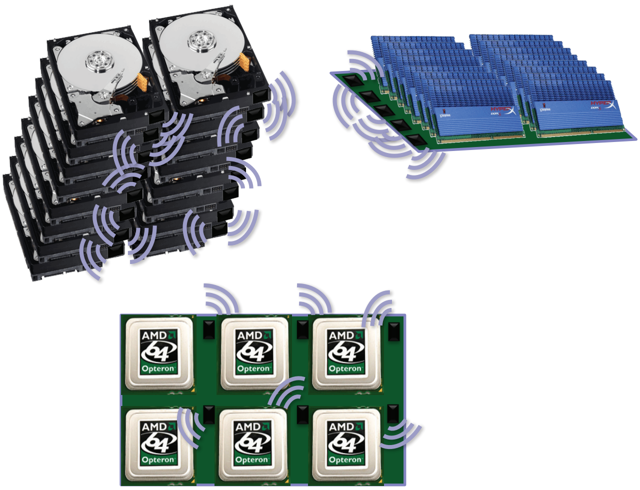

Figure 1.15 MmWave wireless will enable drastic changes to the form factors of today's computing and entertainment products. Multi-Gbps data links will allow memory devices and displays to be completely tetherless. Future computer hard drives may morph into personal memory cards and may become embedded in clothing [Rap12a][Rap09][RMGJ11].

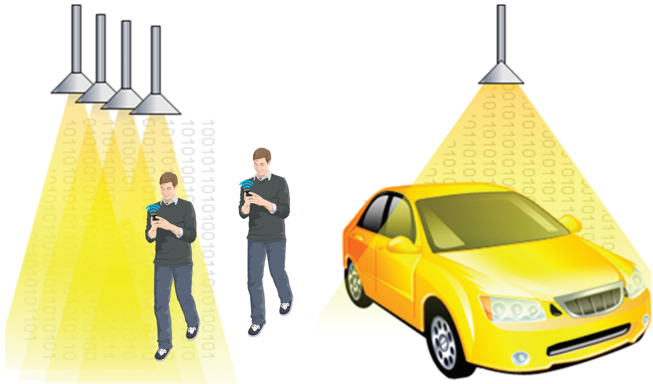

Figure 1.16 Future users of wireless devices will greatly benefit from the pervasive availability of massive bandwidths at mmWave frequencies. Multi-Gbps data transfers will enable a lifetime of content to be downloaded on-the-fly as users walk or drive in their daily lives [Rap12a][Rap09][RMGJ11].

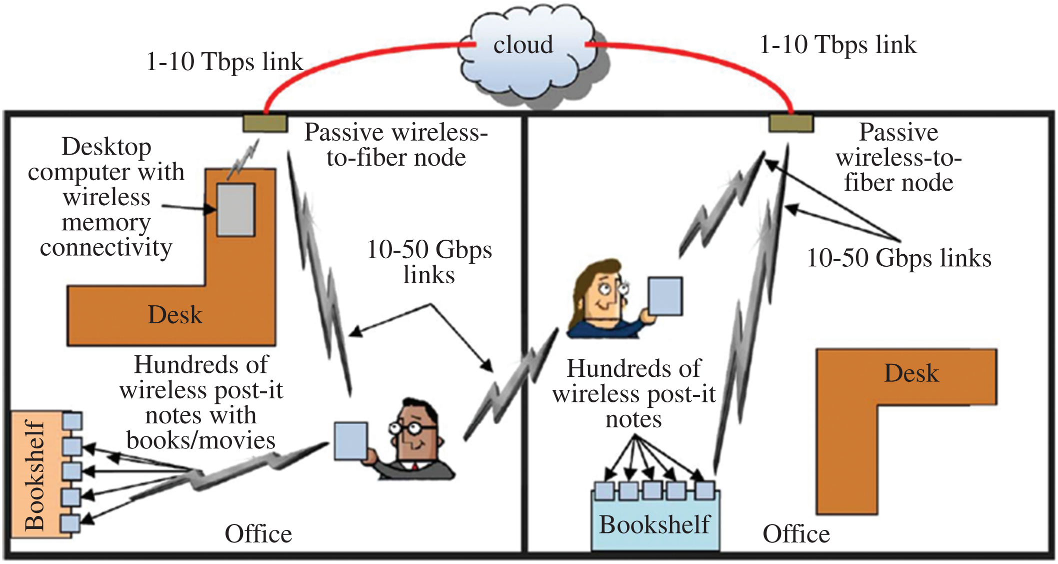

Figure 1.17 The office of the future will replace wiring and wired ports with optical-to-RF interconnections, both within a room and between rooms of a building. UWB relays and new distributed wireless memory devices will begin to replace books and computers. Hundreds of devices will be interconnected with wide-bandwidth connections through mmWave radio connections using adaptive antennas that can quickly switch their beams [Rap11] [from [RMGJ11] © IEEE].

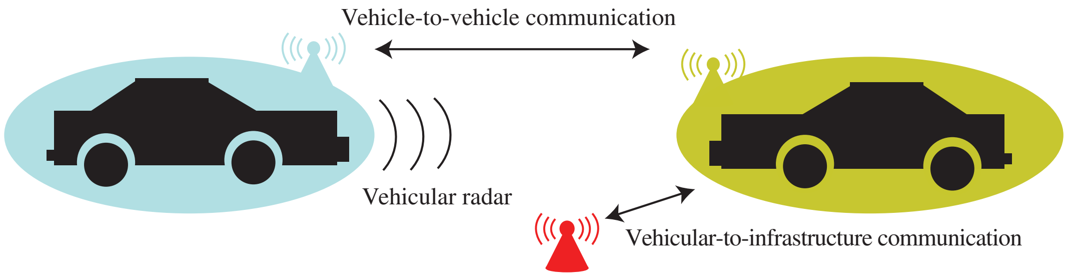

Figure 1.18 Different applications of mmWave in vehicular applications, including radar, vehicle-to-vehicle communication, and vehicle-to-infrastructure communication.

Figure 1.19 Different applications of mmWave in aircraft including providing wireless connections for seat-back entertainment systems and for wireless cellular and local area networking. Smart repeaters and access points will enable backhaul, coverage, and selective traffic control.

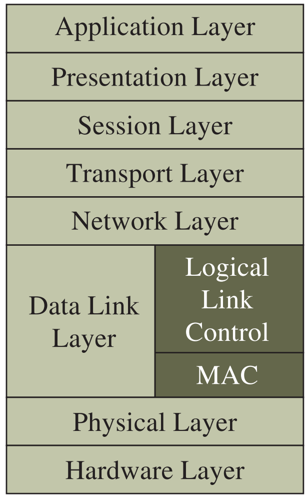

Figure 2.32 Reference system architecture for a communication network. The Physical Layer (PHY) is considered the lowest layer, and the Application Layer is the highest layer. We propose a new layer, called the *Hardware Layer*, that is below PHY, in order to account for complexities involved with the creation of new hardware and devices for mmWave communications.

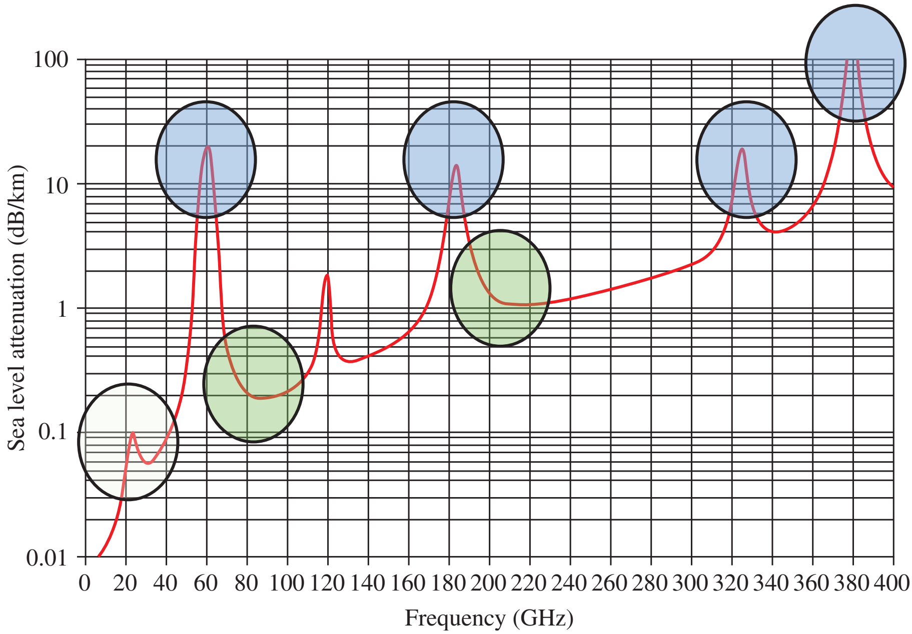

Figure 3.1 The attenuation (dB/km) in excess of free space propagation due to absorption in air at sea level across the sub-terahertz frequency bands. The far left (unshaded) bubble shows extremely small excess attenuation in air for today's UHF and microwave consumer wireless networks, and other bubbles show interesting excess attenuation characteristics that are dependent on carrier frequency [from [RMGJ11], © IEEE].

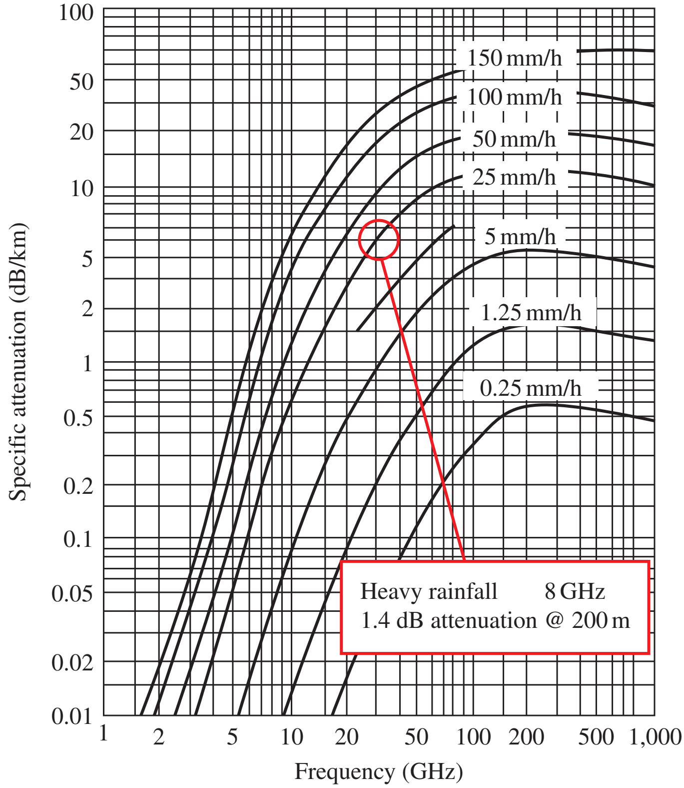

Figure 3.2 Rain attenuation as a function of frequency and rain rate in the mmWave spectrum [from [AWW+13][RSM+13][ZL06] © IEEE].

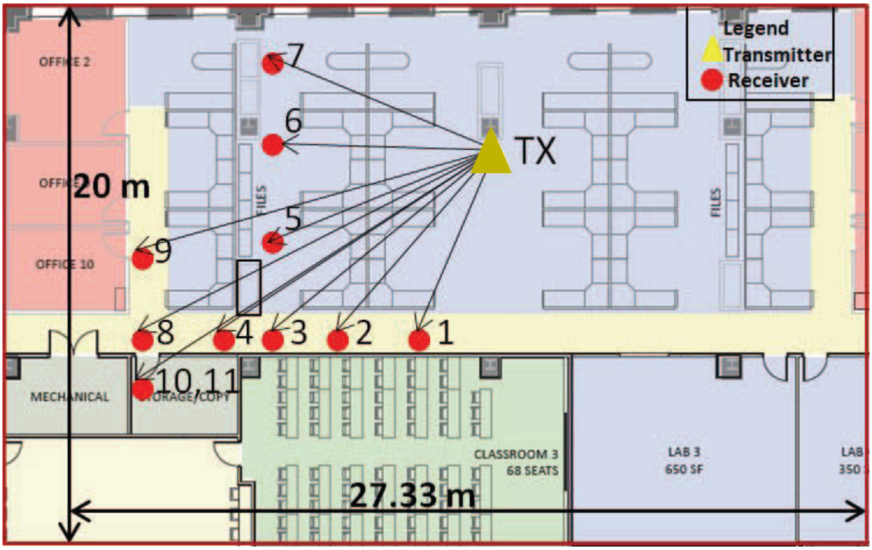

Figure 3.5 Indoor penetration measurements at 72 GHz in a building in Brooklyn, New York. The TX location is marked by a triangle, the RX locations are shown as numbered dots. The primary ray paths for signal penetration are shown with arrows [reproduced from [NMSR13] © IEEE].

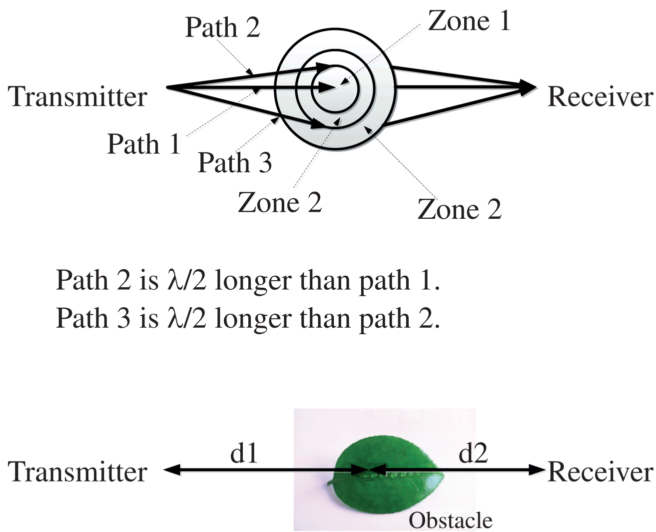

Figure 3.6 Example of a diffraction object blocking the line-of-sight (LOS) path between transmitter and receiver. At millimeter wave frequencies, objects such as trees and people may induce fading and scattering as they move.

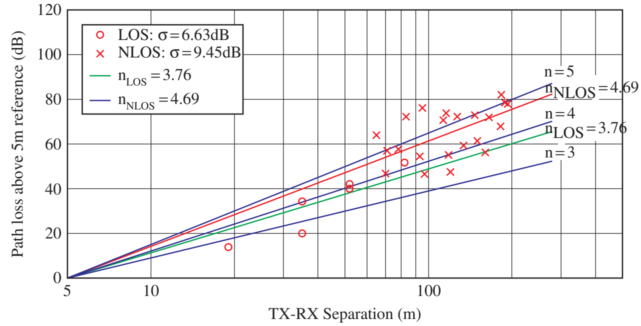

(b) Path loss corresponding to non-coherently combined two best powers versus distance

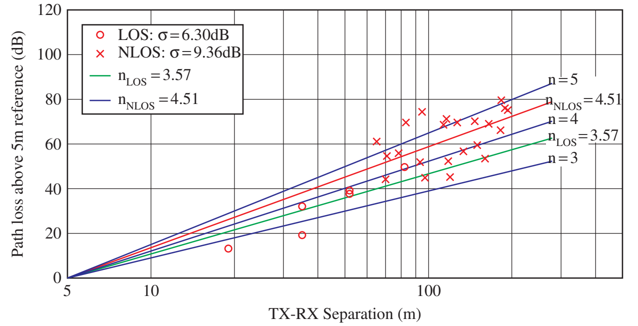

(c) Path loss corresponding to coherently combined two best powers versus distance

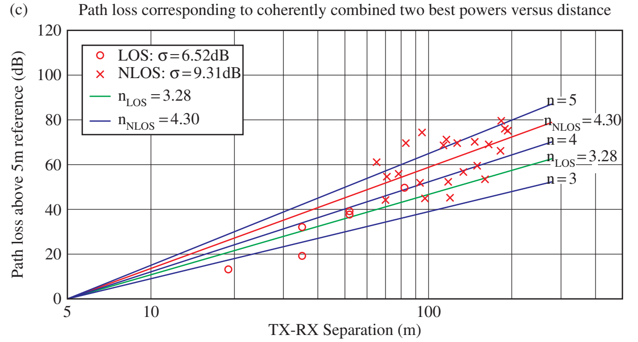

(d) Path loss corresponding to coherently combined three best powers versus distance

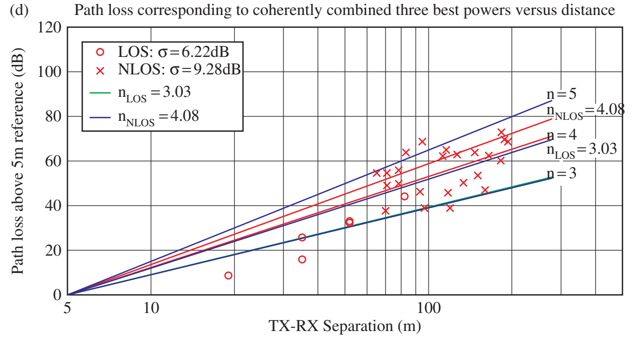

Figure 3.11 Scatter plots of measured 28 GHz cellular path loss in New York City [SR13][RSM+13][AWW+13][SWA+13]. The plots illustrate the reduction in path loss that can be achieved when a mobile handset using 10° steerable beams combines individual multipath signals arriving at different angles from the same transmitter. In (a), the single best beam pointing direction is used to make a link at each RX location. In (b), the two best beam pointing directions are non-coherently combined (where the powers in each unique beam are simultaneously added). In (c) and (d), the two and three best beams, respectively, are coherently added (where the total voltage in each unique beam is simultaneously added and then squared to produce power).

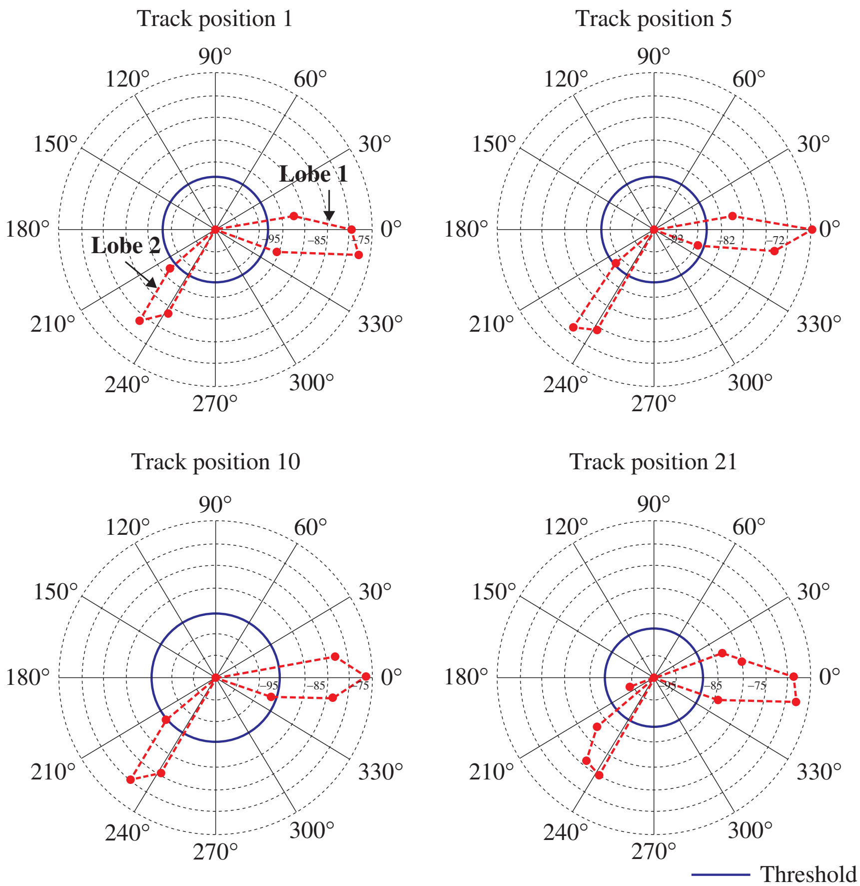

Figure 3.12 Four polar plots of 28 GHz propagation at track positions 1, 5, 10, and 21 along a 21-step linear track with $\lambda/2$ step sizes show two lobes of received power across azimuth. Measurements are for a partially obstructed NLOS RX environment in downtown Brooklyn using 24.5 dBi horn antennas at both the TX and RX. The TX was placed on the rooftop of NYU's Rogers Hall 135 m away from the RX. Each dot represents the received power level at a particular RX azimuth angle. For NLOS RX locations, a threshold of 20 dB below maximum power level was defined for a threshold (shown as a solid-line circle) to determine lobe statistics, whereas 10 dB was used for the LOS threshold [reproduced from [SWA+13] © IEEE].

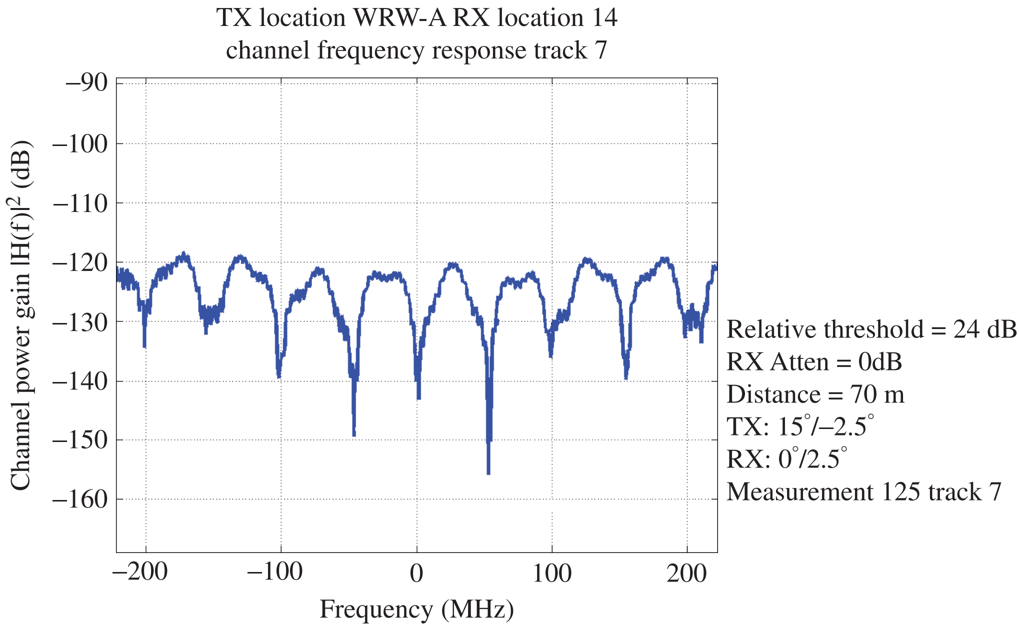

Figure 3.13 Frequency-selective fading occurs about the 38 GHz carrier frequency in outdoor urban NLOS channels. Note the periodic 50 MHz fades in frequency about the carrier correspond to a RMS delay spread that is approximately 20 ns. Here we see a channel that has deep fades as low as 30 dB from the peak channel gain.

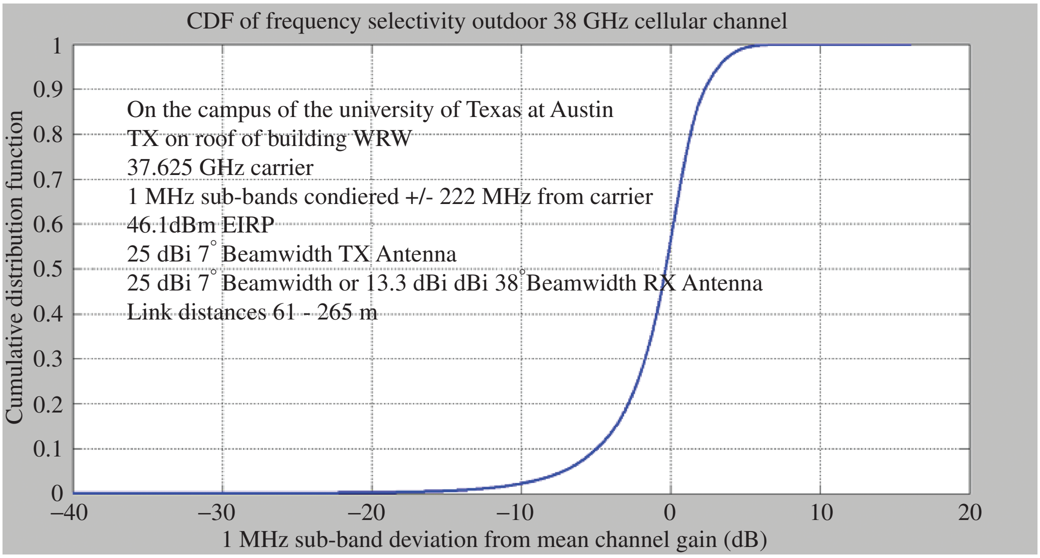

Figure 3.14 When a channel frequency representation such as that shown in Fig. 3.13 is considered over 1 MHz subbands (i.e., we evaluate the average channel gain at 1 MHz intervals and compare these small intervals to the overall average channel gain across the band), we see that fading is not severe for outdoor urban cellular mmWave channels. The time delay spread and the number of resolvable multipath components directly contribute to the fading characteristics across the occupied spectrum. Directional antennas change small-scale fading from today's common Rayleigh fading characteristics (for omnidirectional antennas) into much narrower fade depths over much wider frequency bands.

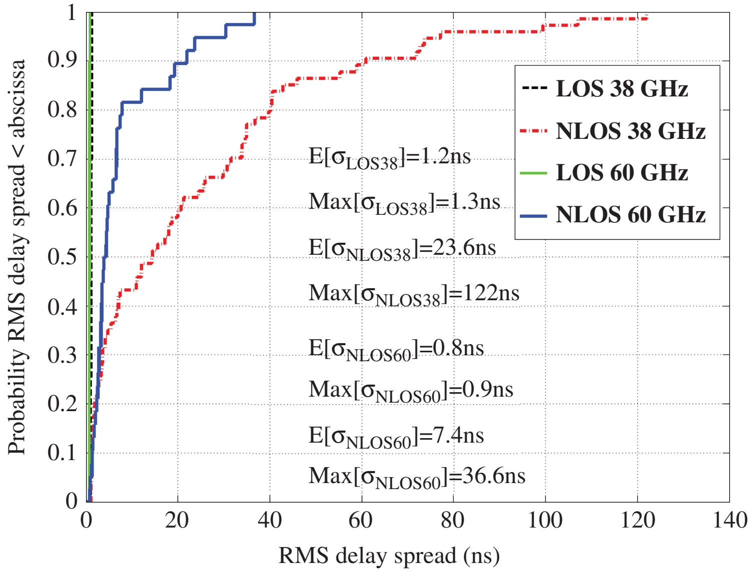

Figure 3.15 Differences in RMS delay spread and their distribution at 38 and 60 GHz in various outdoor environments [from [RBDMQ12] © IEEE].

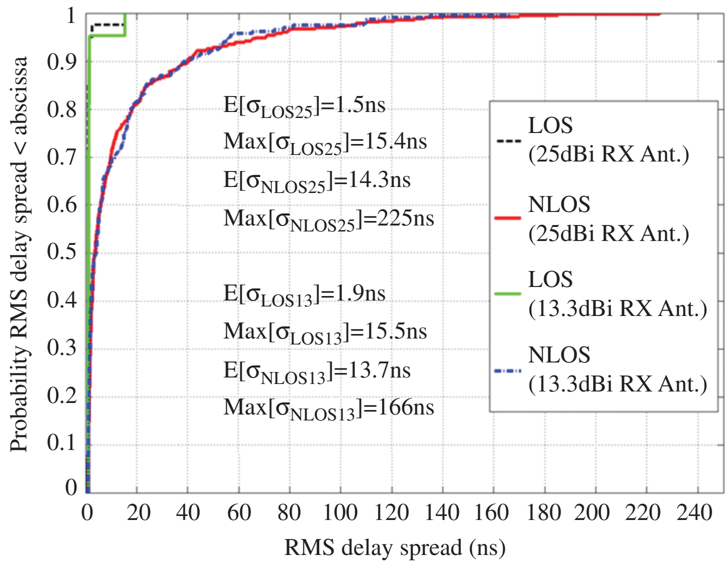

Figure 3.16 Greater transmitter antenna heights resulted in decreased 90% RMS delay spread compared with situations in which the 38 GHz transmitter is near the ground, and the worst-case RMS delay spread was found to be 225 ns on a Texas college campus using the tallest transmitter antenna height [from [RSM+13] [RGBD+13] © IEEE].

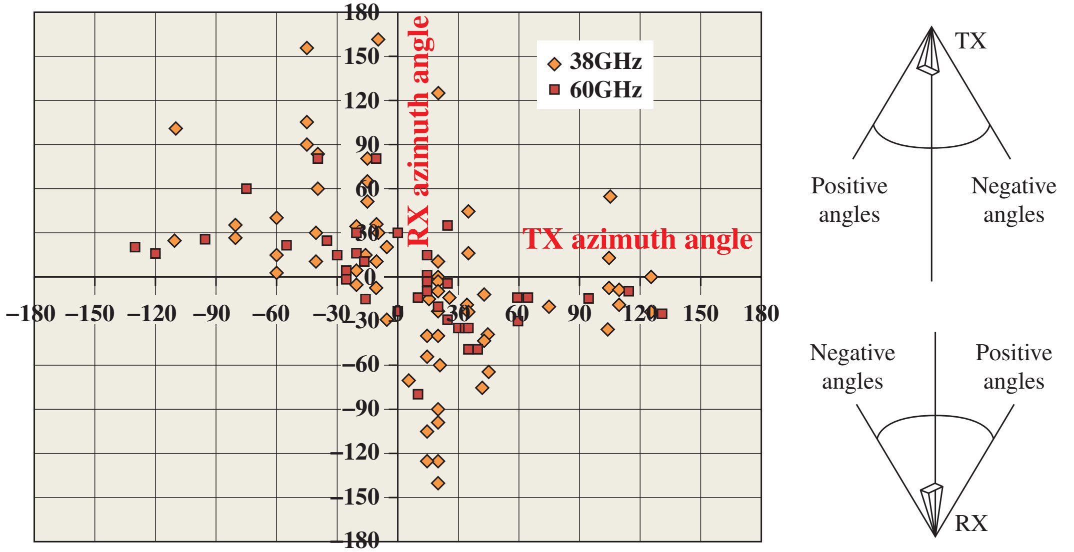

Figure 3.17 MmWave applications in which the transmitter and receiver are close to the ground (such as peer-to-peer or vehicle-to-vehicle) will provide a wide distribution of angles at which links may be established [from [RBDMQ12][RGBD+13] © IEEE].

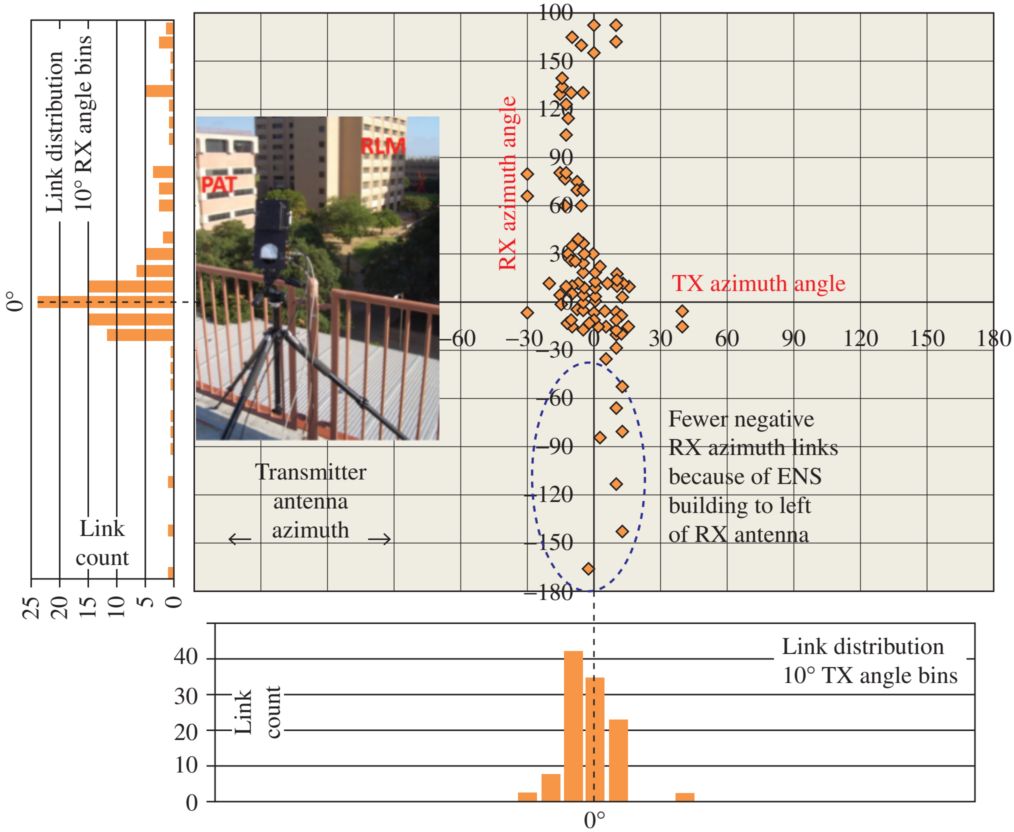

Figure 3.18 The antenna pointing angles found with a 37.625 GHz carrier and highly directional antennas at the receiver and transmitter. The transmitter was elevated to 18 m [from [RBDMQ12] [RGBD+13] © IEEE].

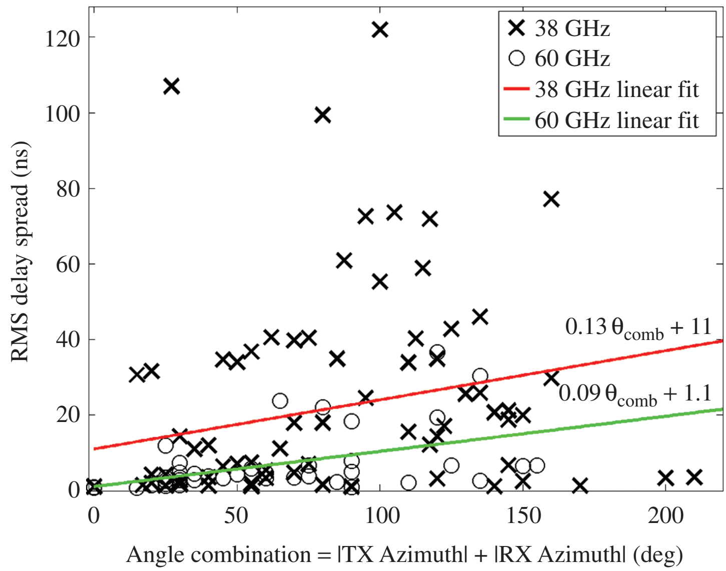

Figure 3.19 Steeper azimuth pointing angles are associated with higher RMS delay spreads for outdoor peer-to-peer channels. The measurements from this plot were taken with 25 dBi 7° beamwidth horns at the transmitter and receiver, and with link distances from 19 to 129 m [from [RBDMQ12] © IEEE].

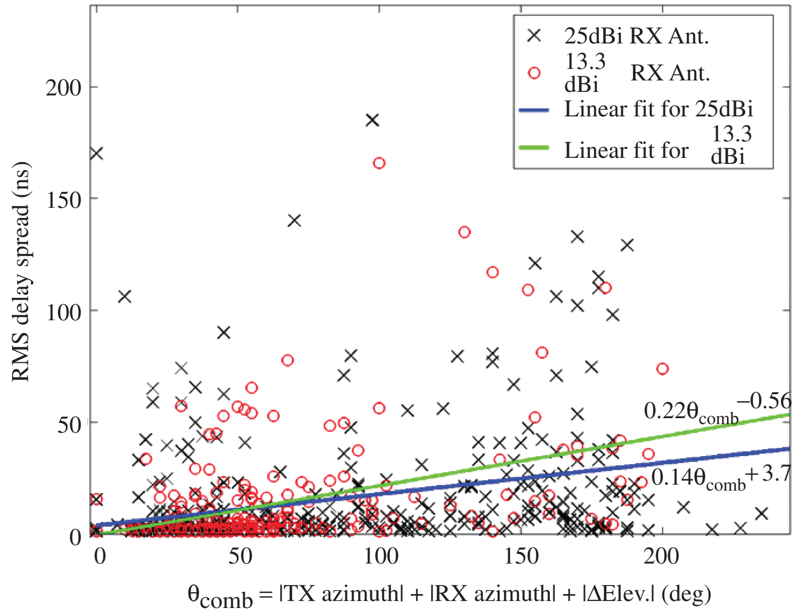

Figure 3.20 Steeper antenna pointing angles are associated with higher RMS delay spreads. These measurements were taken at 38 GHz with at 25 dBi TX antennas, and a 25 dBi or 13.3 dBi RX antennas. Link distances ranged just beyond 900 m [from [RQT+12] © IEEE].

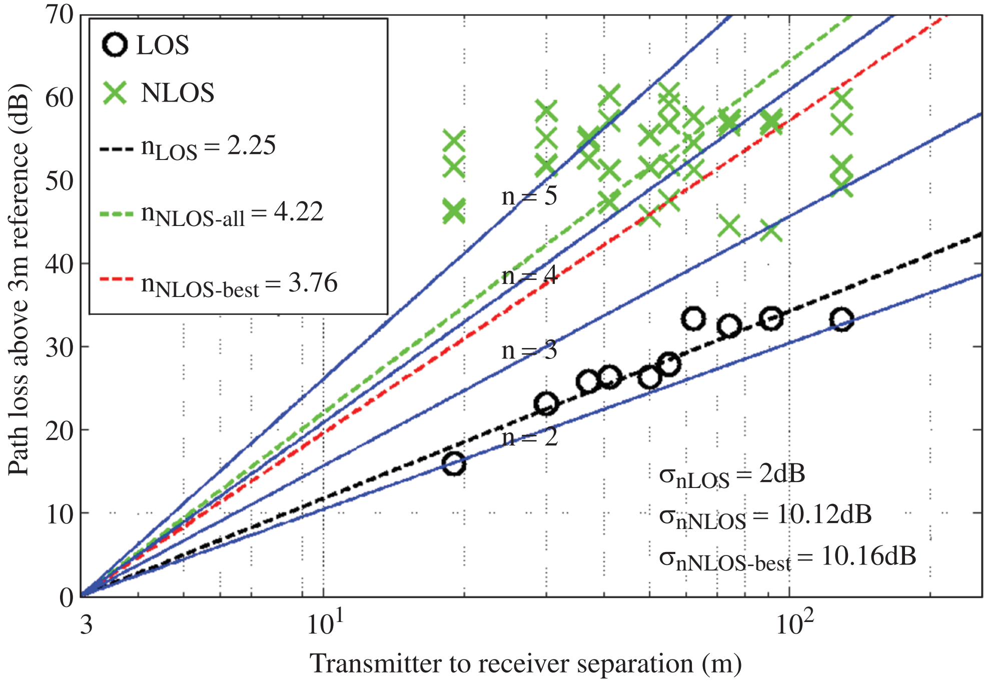

Figure 3.21 Due to the very high value for the break-point distance, LOS links at mmWave frequencies are very close to free space in terms of path loss. This plot was generated with highly directional antennas at the receiver and transmitter with 25 dBi gain and 7° beamwidths at 60 GHz [from [RBDMQ12] © IEEE]. Note that the oxygen absorption causes the path loss exponent to be slightly greater than 2.0.

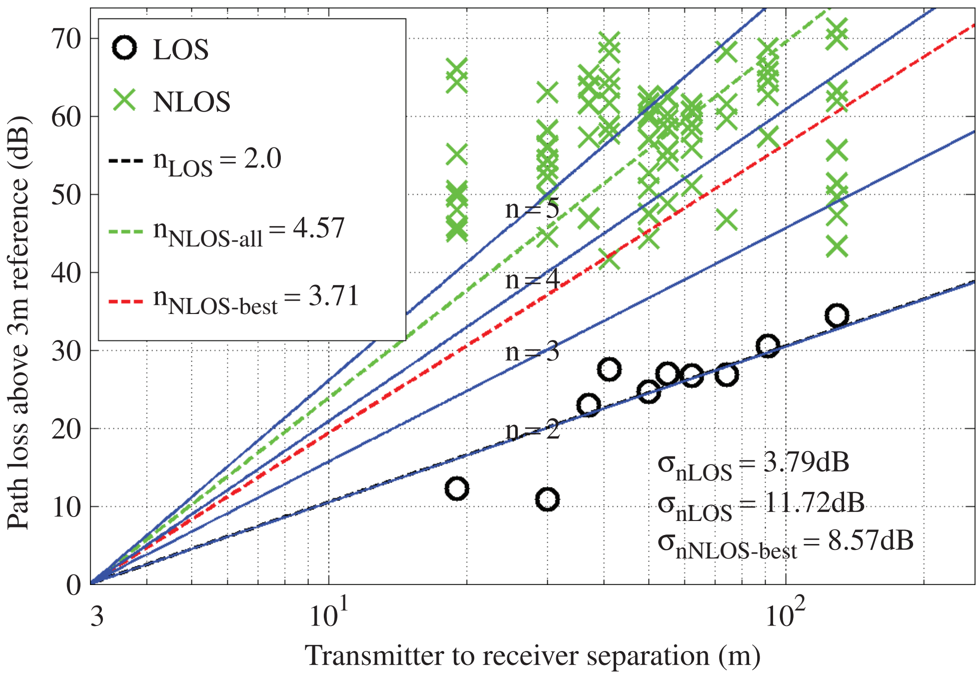

Figure 3.22 This plot shows measured path loss values for 38 GHz peer-to-peer applications with highly directional 25 dBi 7° beamwidth horn antennas [from [RBDMQ12] © IEEE].

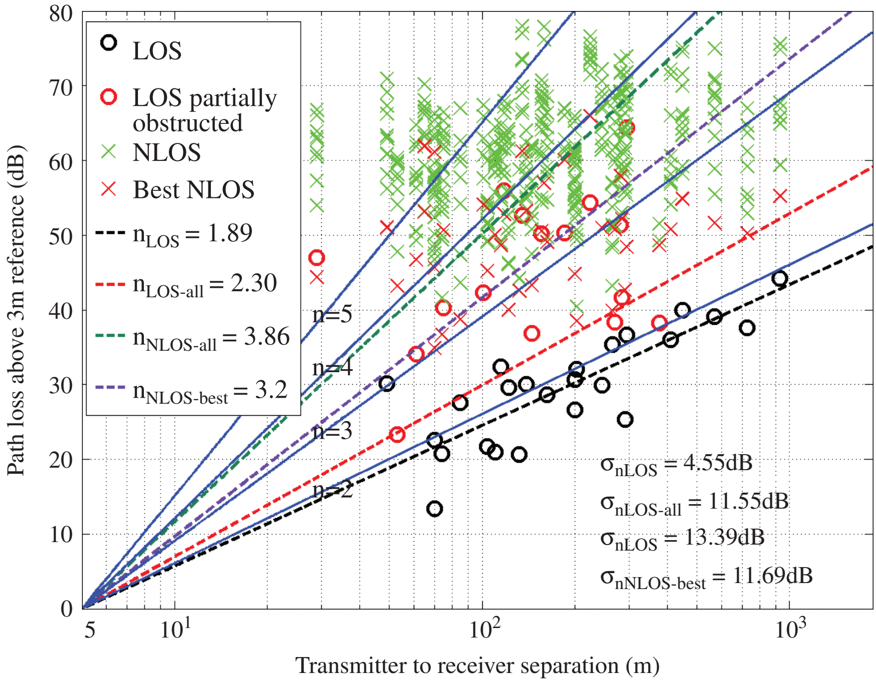

Figure 3.23 When a highly directional antenna is used at the receiver, LOS links will be very close to free space but NLOS links may be more heavily attenuated. This plot is for 38 GHz and the measurements used the same highly directional antennas at both the transmitter and receiver [from [RQT+12] © IEEE].

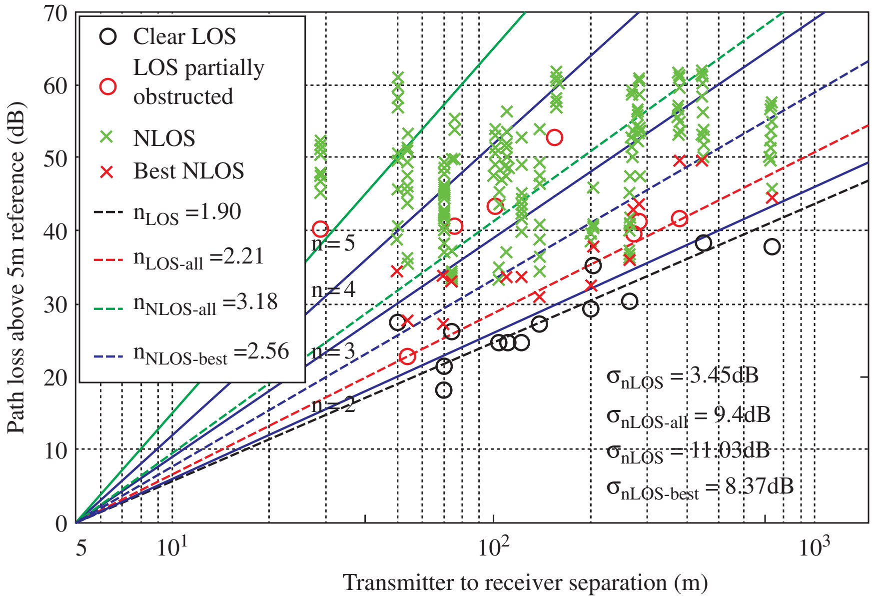

Figure 3.24 This plot was generated from measurements using a 25 dBi 7° beamwidth horn TX antenna and a less directional 13.3 dBi 40° beamwidth horn at the receiver. NLOS paths are significantly stronger as the receiver cannot filter out multipath as effectively as when a more directional antenna is used [RQT+12] © IEEE].

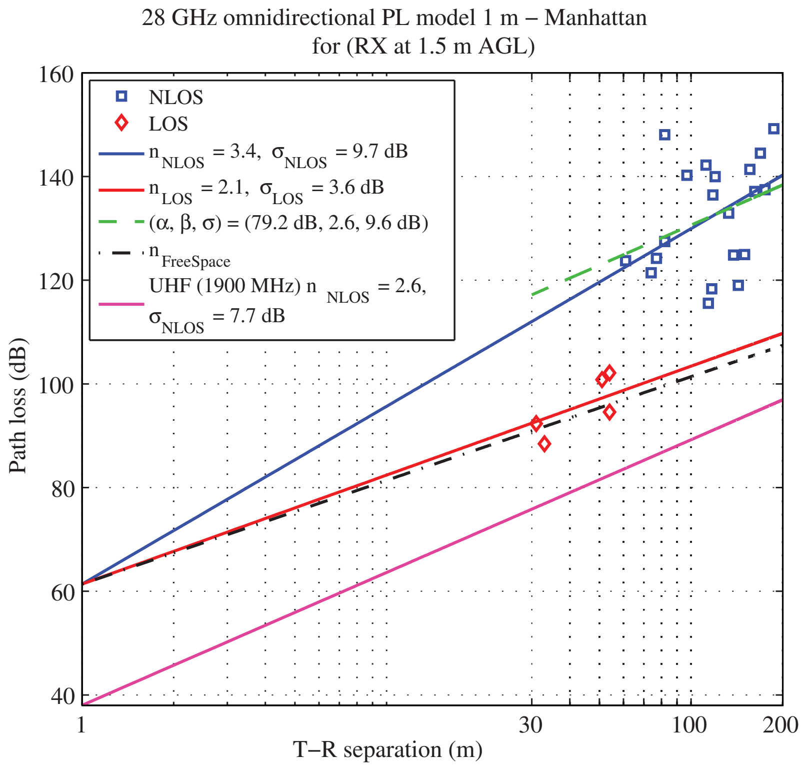

Figure 3.25 28 GHz omnidirectional close-in free space reference distance ($d_0 = 1$ m) and floating intercept path loss models for a non-line of sight (NLOS) urban environment with a receiver antenna 1.5 m above ground. A comparison is made to path loss in a 1.9 GHz urban NLOS environment as reported in [BFR+92] [FBRSX94].

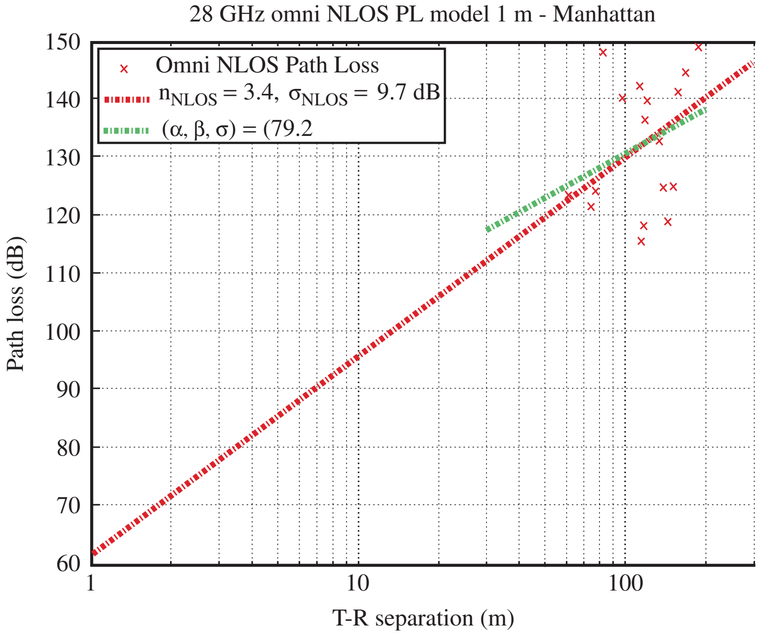

Figure 3.26 28 GHz omnidirectional path loss model from which the TX and RX antenna gains have been removed. The close-in free space reference distance model with respect to a 1 m free space reference distance, and the floating intercept (α, β) model from [RRE14] is shown for distances ranging from 30 to 200 m.

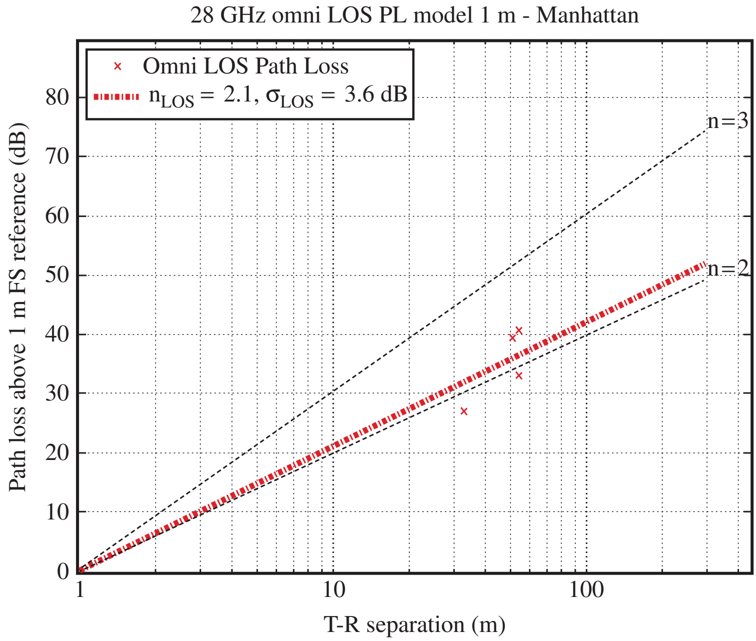

Figure 3.27 28 GHz omnidirectional path loss model from which the TX and RX antenna gains have been removed. The close-in free space reference distance model with respect to a 1 m free space reference distance is shown. Note that one point at 100 m had excessive path loss due to the fact that the antennas were not aligned on boresight at this location. By removing this single point, it is evident that the LOS path loss exponent is very close to 2.

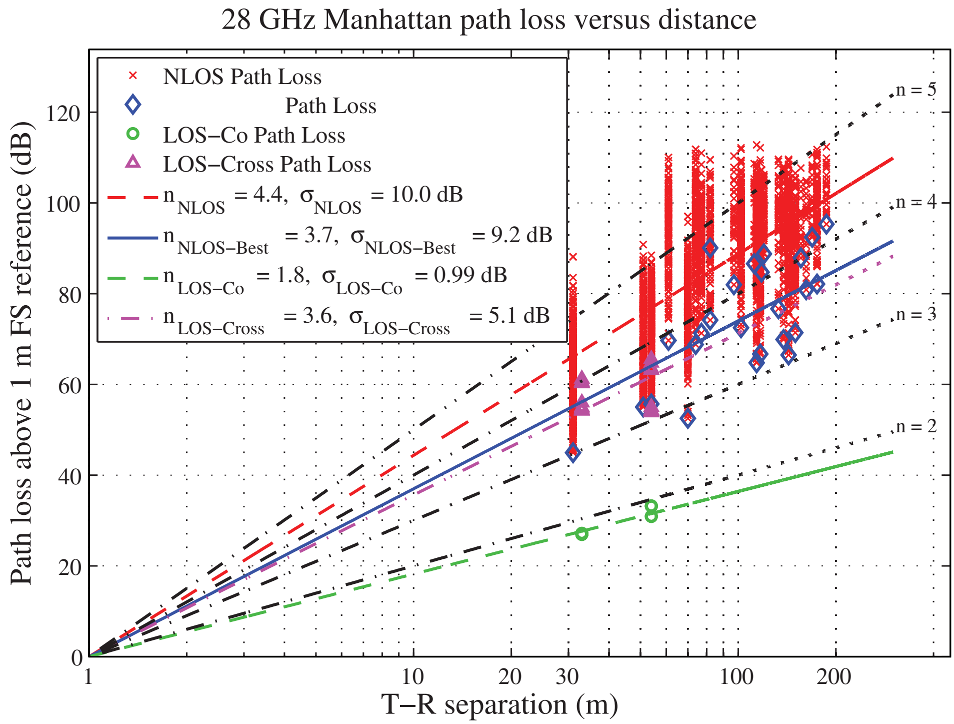

Figure 3.28 28 GHz Manhattan single beam path loss measurements as a function of T-R separation distance using 24.5 dBi horn antennas with 10.9° half-power beam width at both the TX and RX and 15 dBi (28.8 degree HPBW) horn antennas at both the TX and RX. NLOS path losses include LOS non-boresight and truly NLOS measurements. Co-polarized and cross-polarized LOS measured path losses are also shown. The close-in free space reference distance model with respect to a 1 m free space reference distance is shown. All data points represent path loss values calculated from recorded PDP measurements.

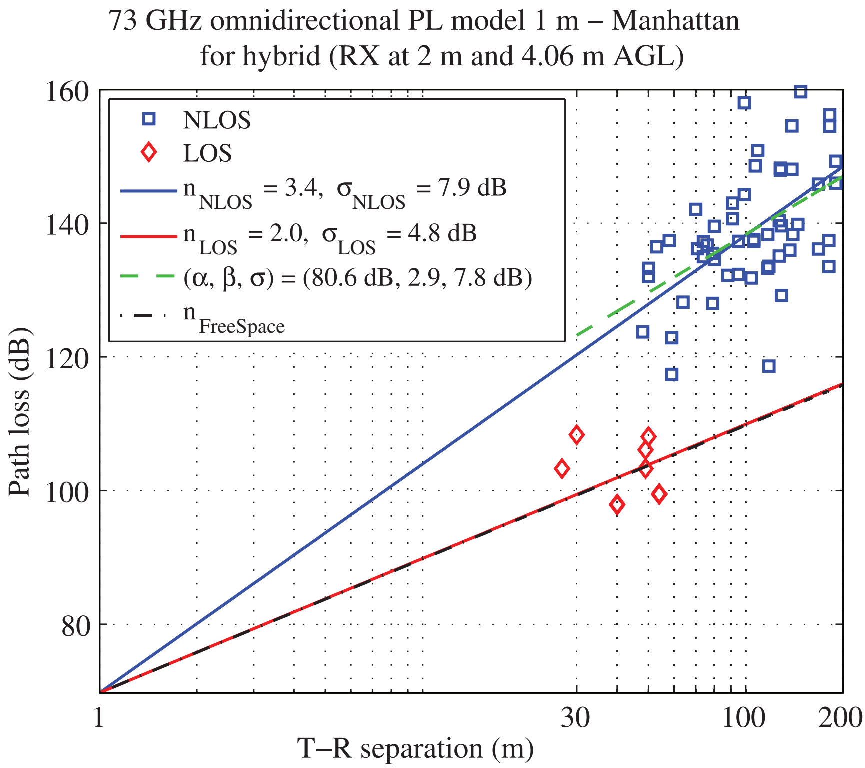

Figure 3.29 73 GHz omnidirectional path loss model from which the TX and RX antenna gains have been removed for a combination of cellular and backhaul (hybrid) RX antenna heights. The close-in free-space reference distance model for $d_0 = 1$ m and the floating intercept (α, β) model from [RRE14] over 30-200 m are shown.

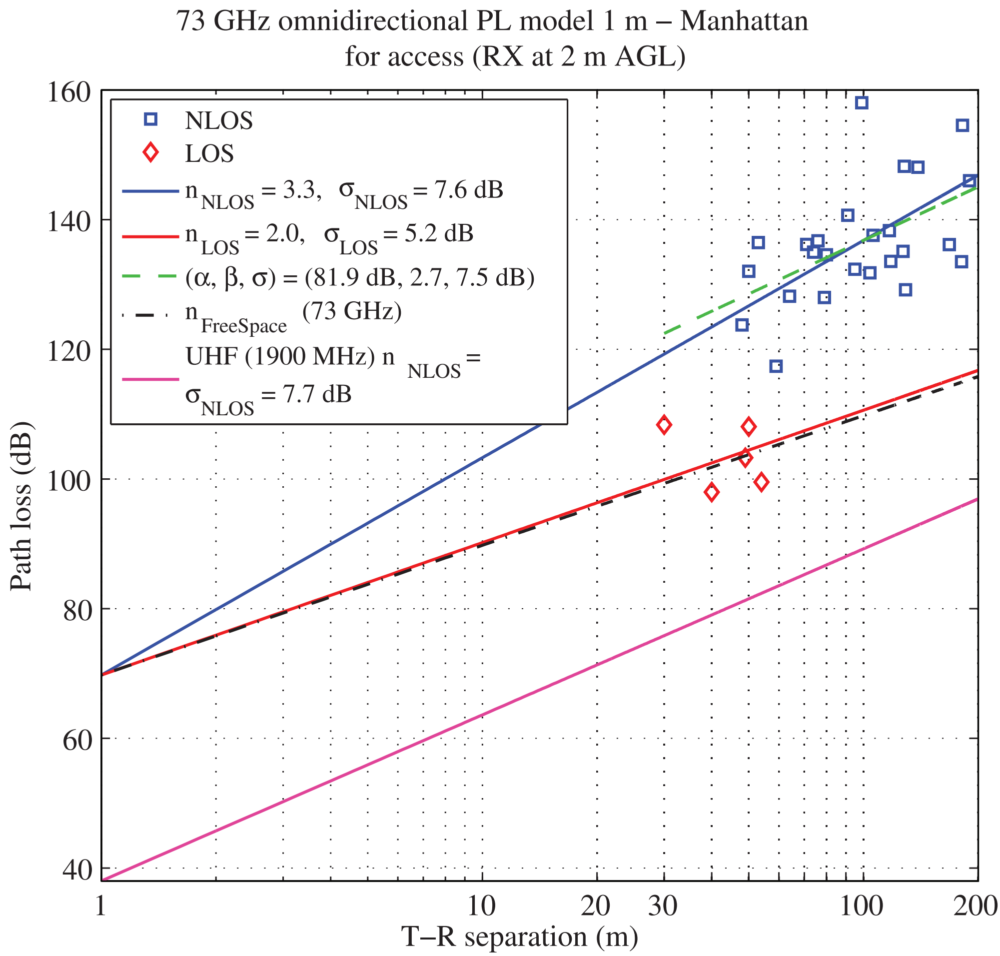

Figure 3.30 73 GHz omnidirectional path loss model from which the TX and RX antenna gains have been removed for mobile RX antenna heights of 2 m. The close-in free-space reference distance model for $d_0 = 1$ m and the floating intercept model (α, β) model from [RRE14] over 30-200 m are shown. A comparison is made to path loss in a 1.9 GHz urban NLOS environment as reported in [BFR+92].

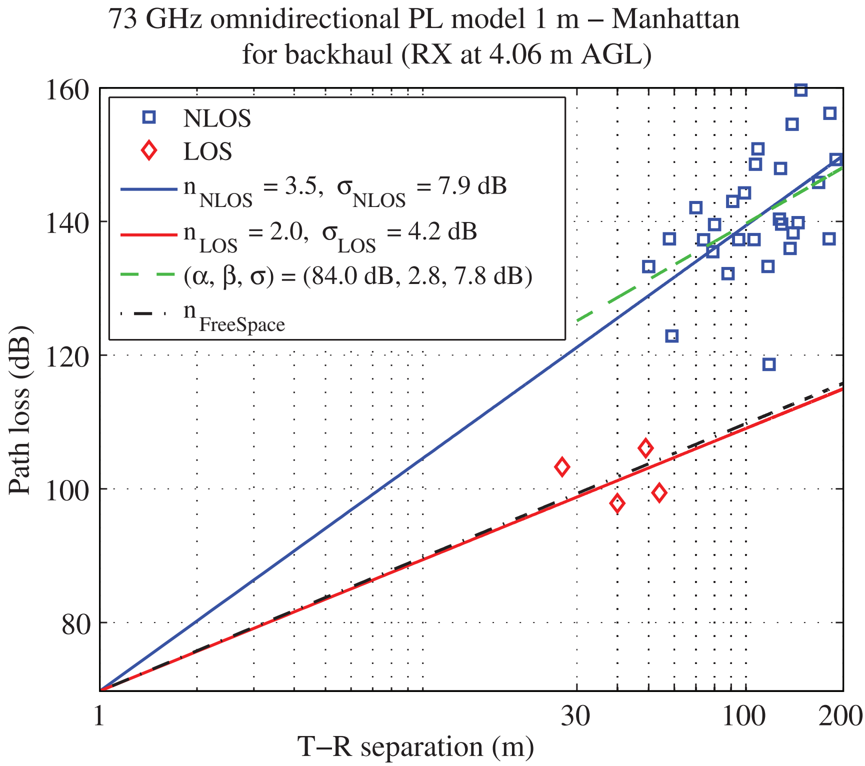

Figure 3.31 73 GHz omnidirectional path loss model from which the TX and RX antenna gains have been removed for backhaul RX antenna heights of 4.06 m. The close-in free-space reference distance model for $d_0 = 1$ m and the floating intercept $(\alpha,\ \beta)$ model from [RRE14] over 30-200 m are shown.

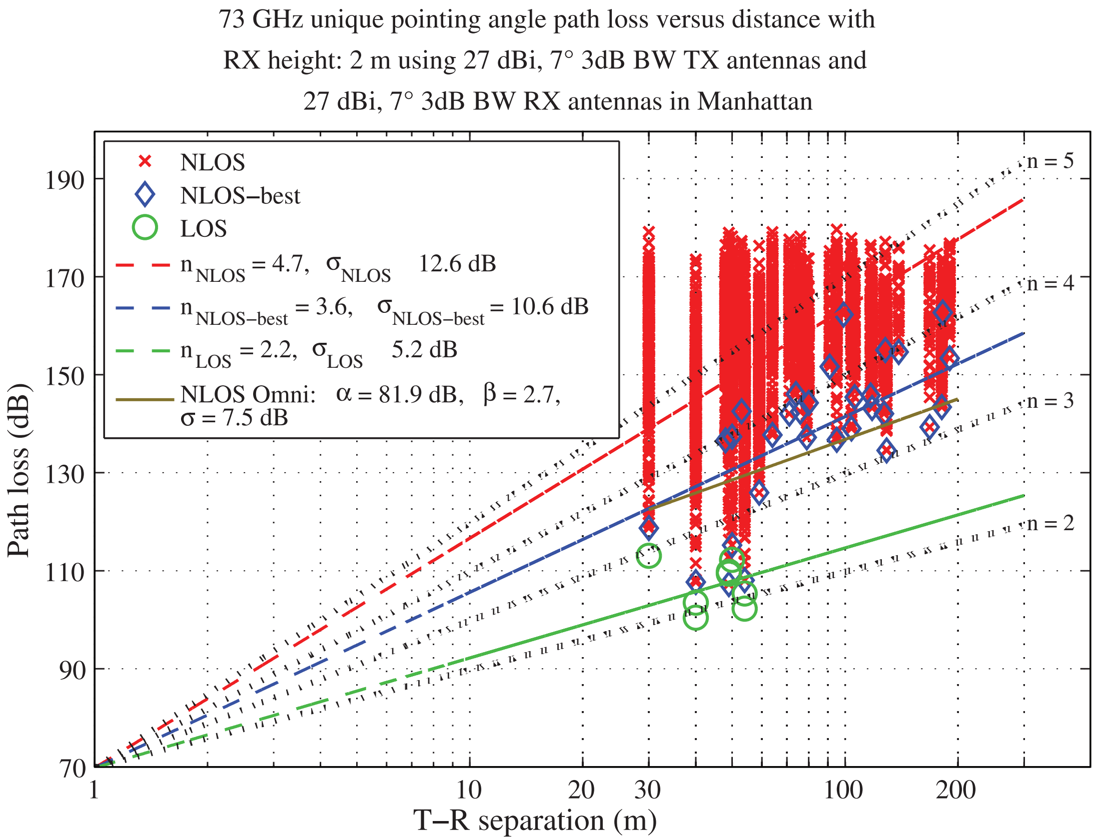

Figure 3.32 New York City cellular RX height (2 m) path loss measurements at 73 GHz as a function of T-R separation distance using vertically polarized 27 dBi, 7° half-power beam width TX and RX antennas. All data points represent path loss values calculated from recorded PDP measurements. Crosses indicate all NLOS pointing angle data points, diamonds indicate best NLOS pointing angle data points for each RX location and each T-R combination, and circles indicate LOS data points. The measured path loss values are relative to a 1 m free-space close-in reference distance. NLOS PLEs are calculated for the entire data set and also for the best recorded link. LOS PLEs are calculated for strictly boresight-to-boresight scenarios. n values are PLEs and σ values are shadow factors. The solid line spanning 30 to 200 m is the omnidirectional (α, β) model from [RRE14] [ALS$^+$14] depicted in Fig. 3.30.

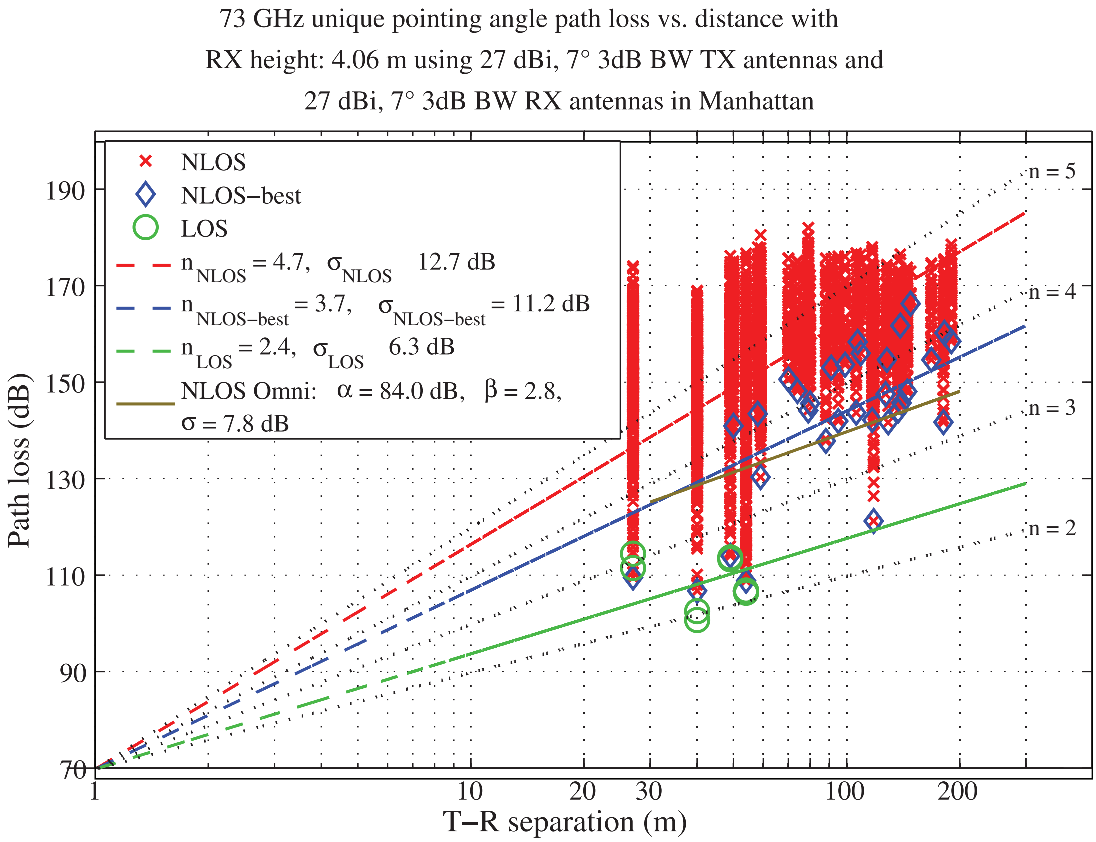

Figure 3.33 New York City backhaul measurements with RX heights of 4.06 m path losses at 73 GHz as a function of T-R separation distance using vertically polarized 27 dBi, 7° half-power beam width TX and RX antennas. All data points represent path loss values calculated from recorded PDP measurements. Crosses indicate all NLOS pointing angle data points, diamonds indicate best NLOS pointing angle data points for each RX location and each T-R combination, and circles indicate LOS data points. The measured path loss values are relative to a 1 m free-space close-in reference distance. NLOS PLEs are calculated for the entire data set and also for the best recorded link. LOS PLEs are calculated for strictly boresight-to-boresight scenarios. n values are PLEs and σ values are shadow factors. The solid line spanning 30 to 200 m is the omnidirectional (α, β) model from [RRE14] depicted in Fig. 3.31.

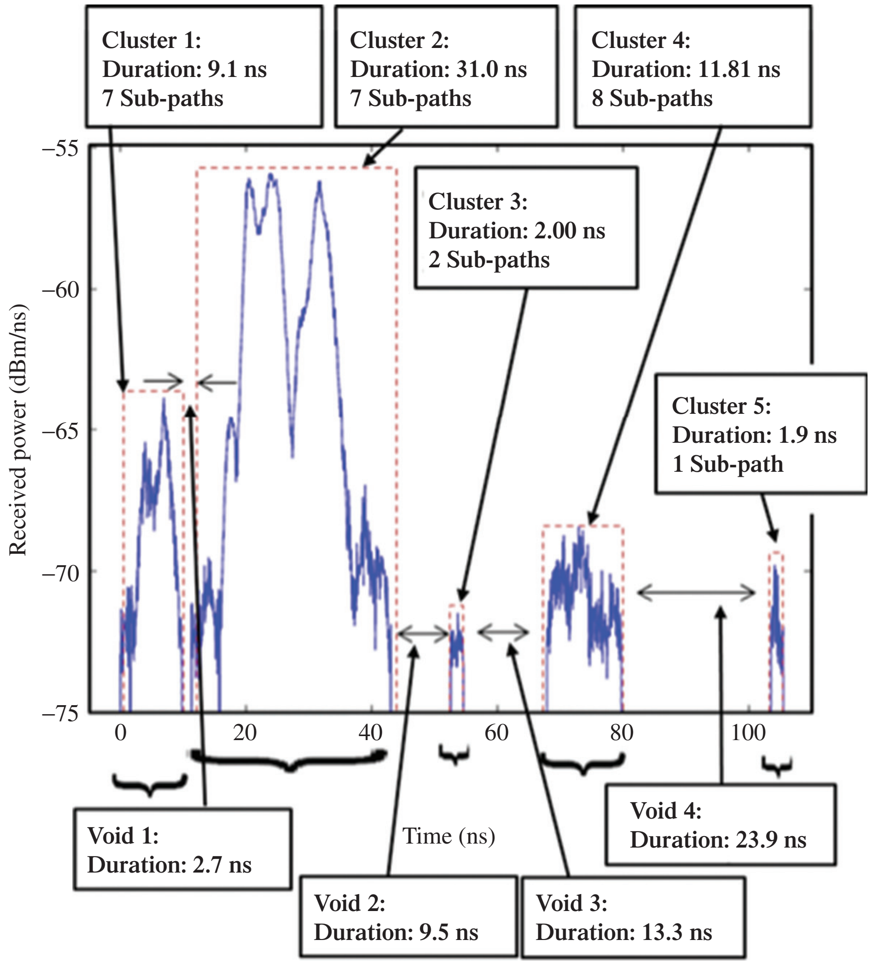

Figure 3.34 Illustration of some of the key temporal modeling parameters used for modeling the temporal clusters in an omnidirectional SSCM wideband mmWave channel. This example shows five time clusters, with time durations ranging from 2 to 31 ns, and voids between clusters ranging from 2.7 to 23.9 ns [SR14a].

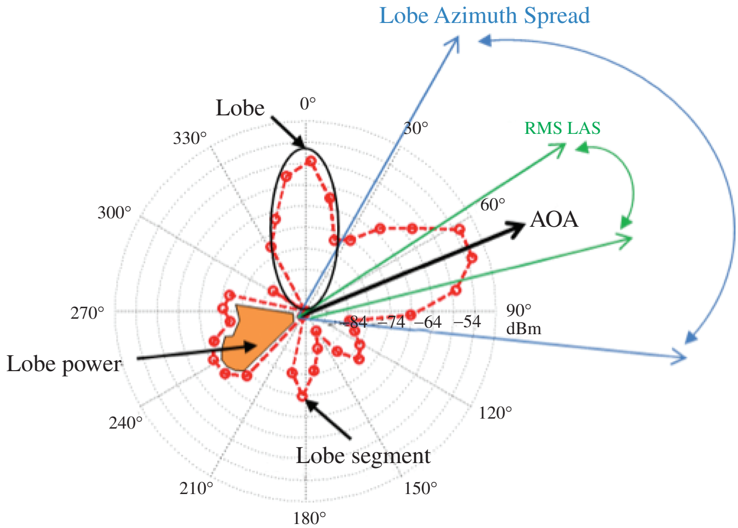

Figure 3.35 Illustration of some of the key spatial modeling parameters used to model the spatial lobes in an omnidirectional SSCM wideband mmWave channel. The polar plot (in the azimuthal/horizontal plane only) shows five distinct lobes with various lobe azimuth spreads and AOAs. Each dot is a lobe angular segment simulated for a particular discrete pointing angle and represents the total integrated received power over a particular beam width (and corresponds to the area under a PDP for the particular RX pointing angle). The lobe power is the sum of powers from each segment within the lobe (e.g., the sum of powers from each lobe segment in a lobe).

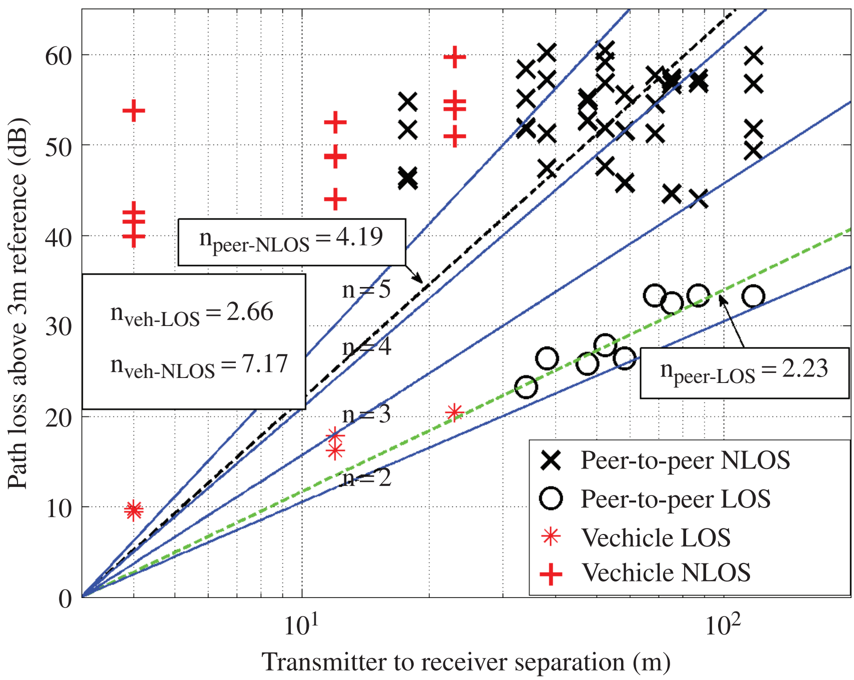

Figure 3.36 Path loss for 60 GHz for peer-to-peer applications and communication from a ground-based transmitter to a receiver in a vehicle. These measurements used highly directional 25 dBi 7° beamwidth antennas as the transmitter and receiver [from [BDRQL11] © IEEE].

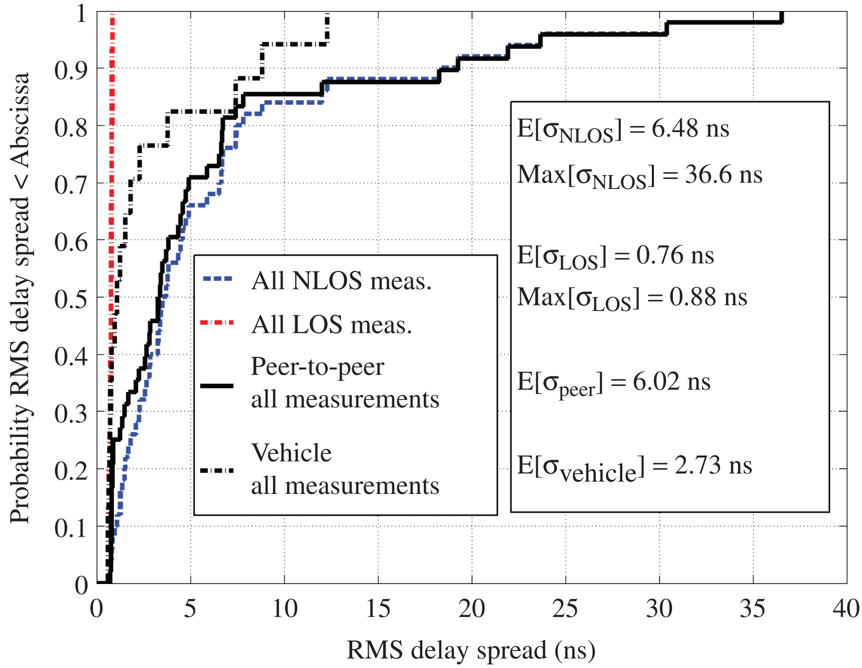

Figure 3.37 These measurements used highly directional 25 dBi 7° beamwidth antennas at the transmitter and receiver. When the transmitter communicates to a receiver inside a vehicle, much lower RMS delay spreads result than when the transmitter and receiver are in the open [from [BDRQL11] © IEEE].

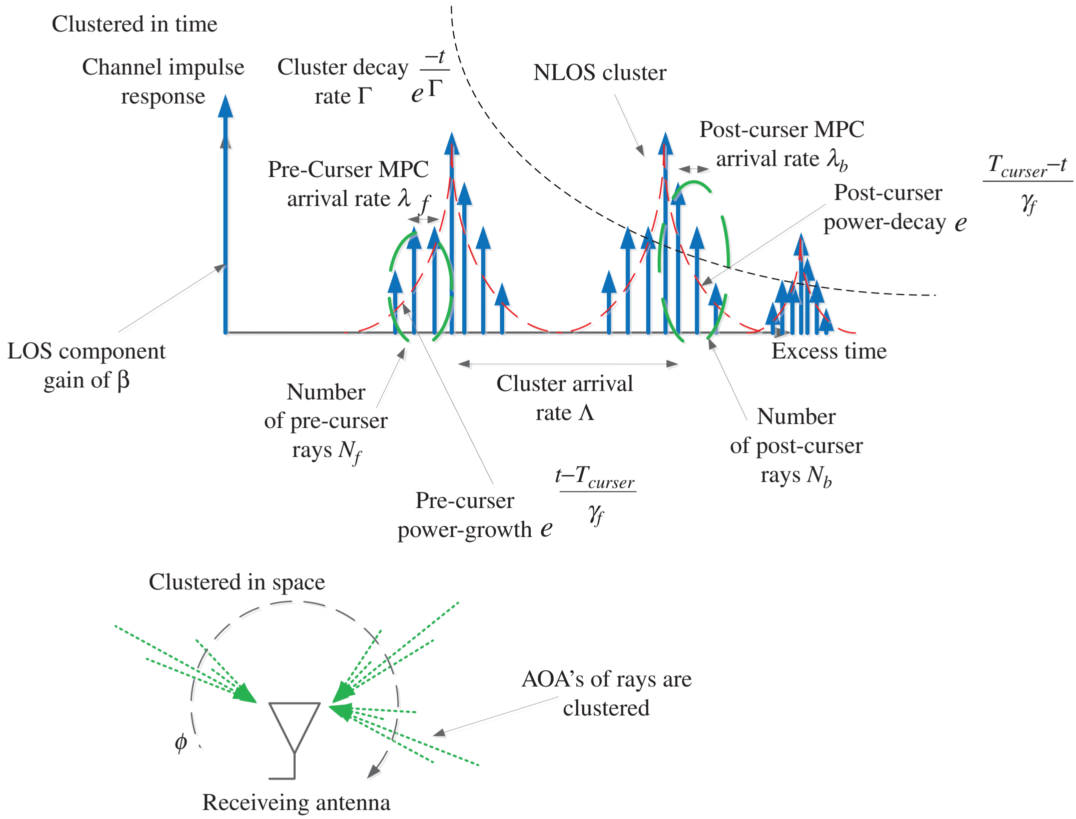

Figure 3.38 Representation of key parameters used to specify multipath channels. Statistics of the key channel parameters are generated from measured data, as collected by wideband channel sounders, to determine the temporal and spatial channel models that can be used by researchers and standard bodies for modem design and signaling protocols.

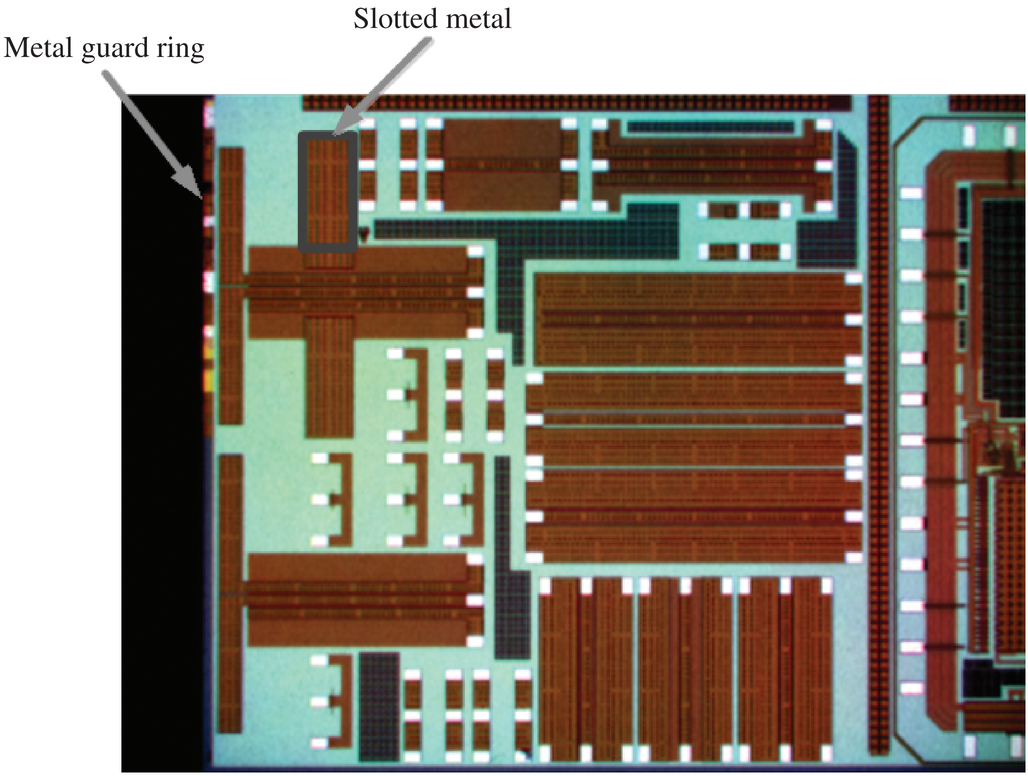

Figure 4.6 There are several considerations for on-chip antennas related to CMOS production rules: 1) All metal layers must meet a minimum fill requirement. This is reflected in the figure by the fact that there are no large portions of the chip left empty (the lighter-shaded portions of the figure). 2) A metal guard ring must often surround the chip to prevent damage during dicing. 3) Large areas of metal must be slotted to meet design rules. 4) Metal structures must meet a minimum size requirement, which in practice is usually satisfied by most designs.

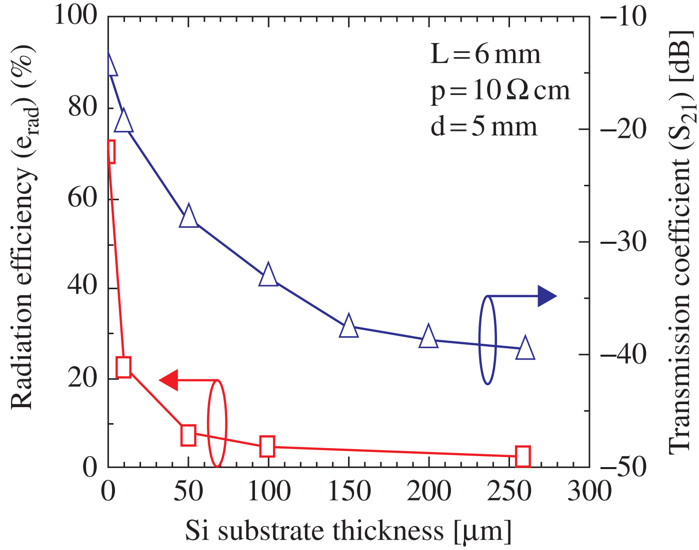

Figure 4.10 This figure indicates that the efficiency of on-chip antennas is reduced greatly by a thick substrate [from [KSK+09] © IEEE].

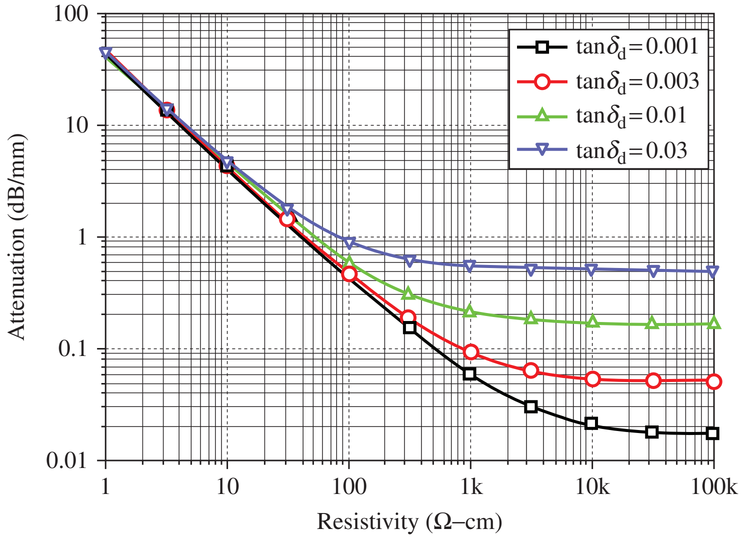

Figure 4.12 For low resistivity substrates, the loss due to currents carried by substrate dopants (i.e., conductive losses) is the major loss mechanism hurting performance [from [LKCY10] © IEEE].

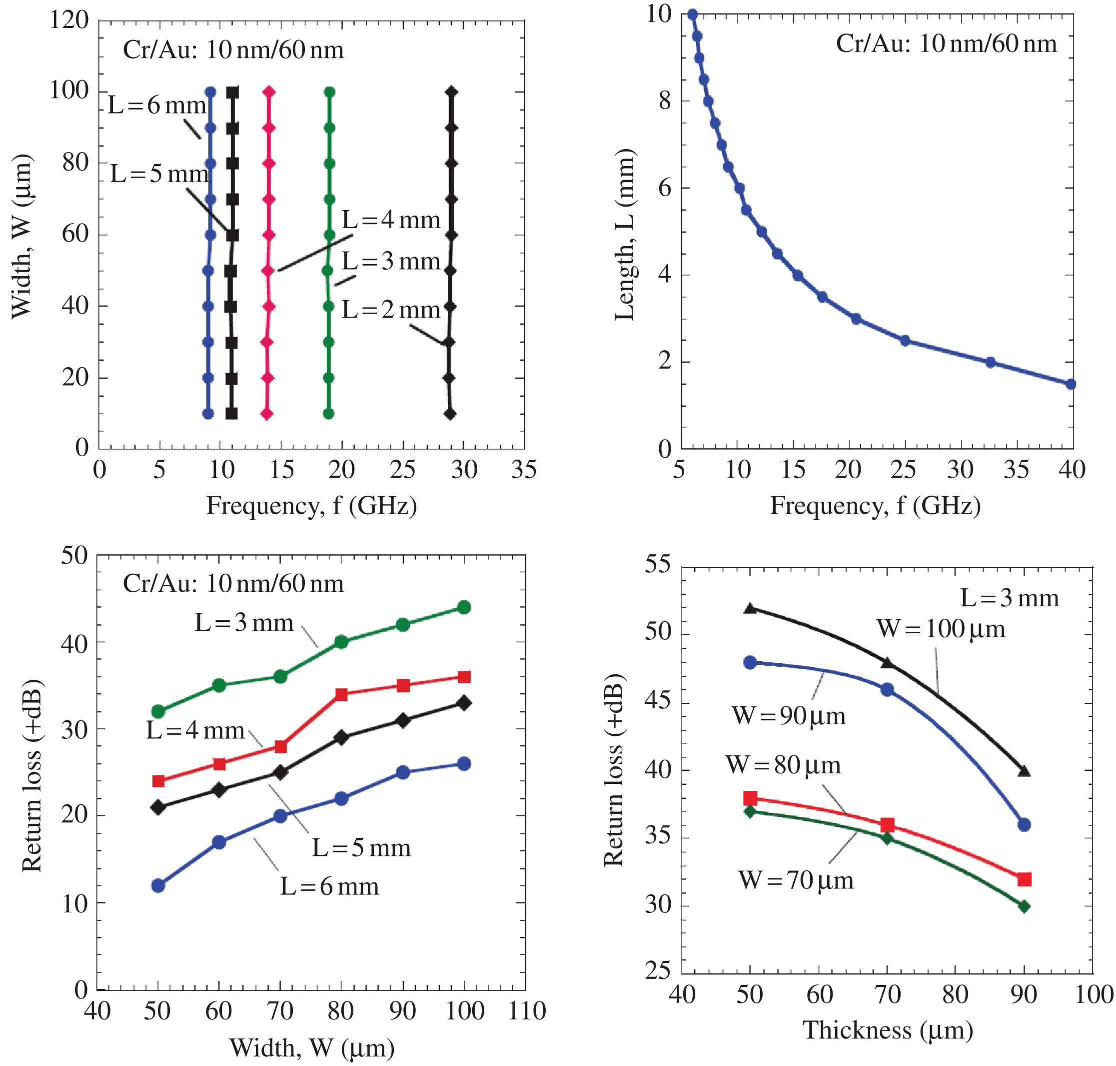

Figure 4.18 [MHP+09] presented these plots for the design of a planar dipole antenna on a 625 μm GaAs substrate with relative permittivity of 12.9 and 625 μm thick [reproduced from [MHP+09] © IEEE].

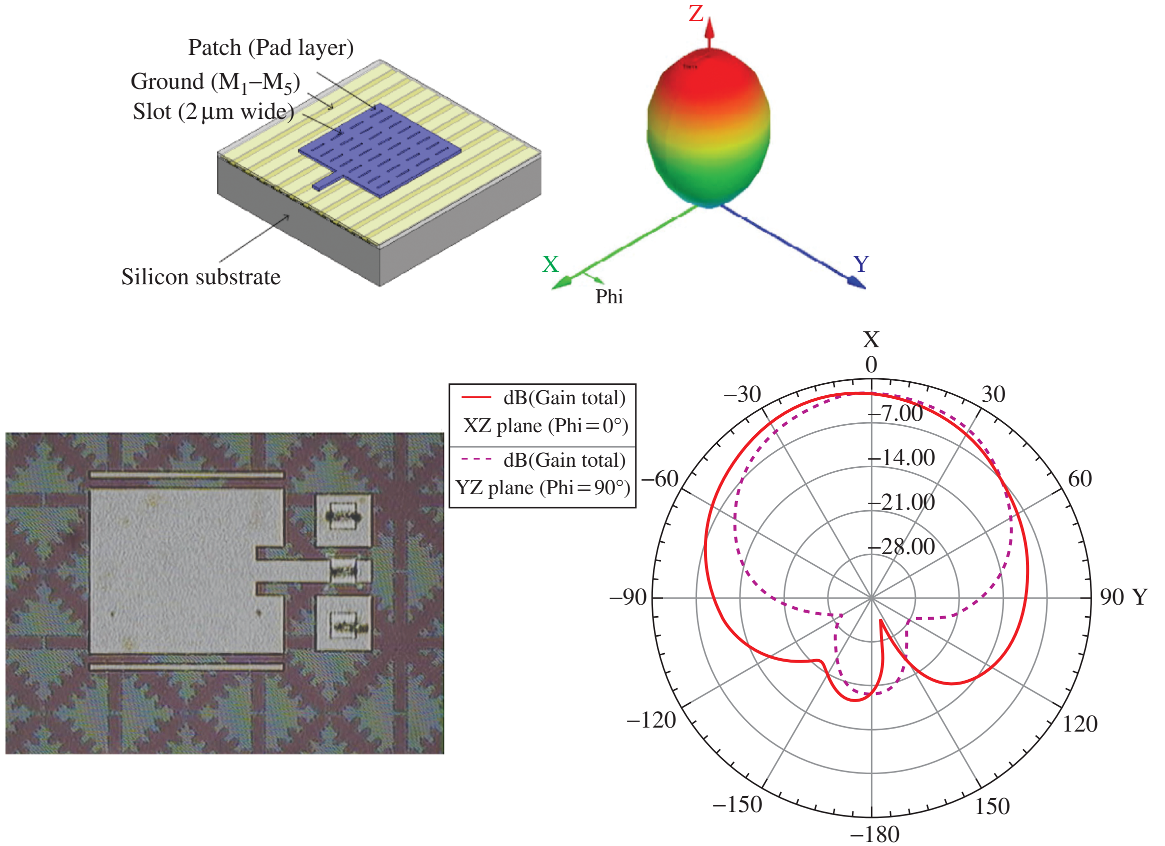

Figure 4.26 This figure shows that a patch antenna typically radiates above the top metal layer of the antenna. The top figure illustrates the metal slots that are usually required for on-chip patch antennas due to their large size. In the lower figure, [CGLS09] used two parallel metal strips on the edge of the patch to increase bandwidth. [This figure is a combination of figures from the literature ([SCS+08] above, [CGLS09] below) © IEEE.]

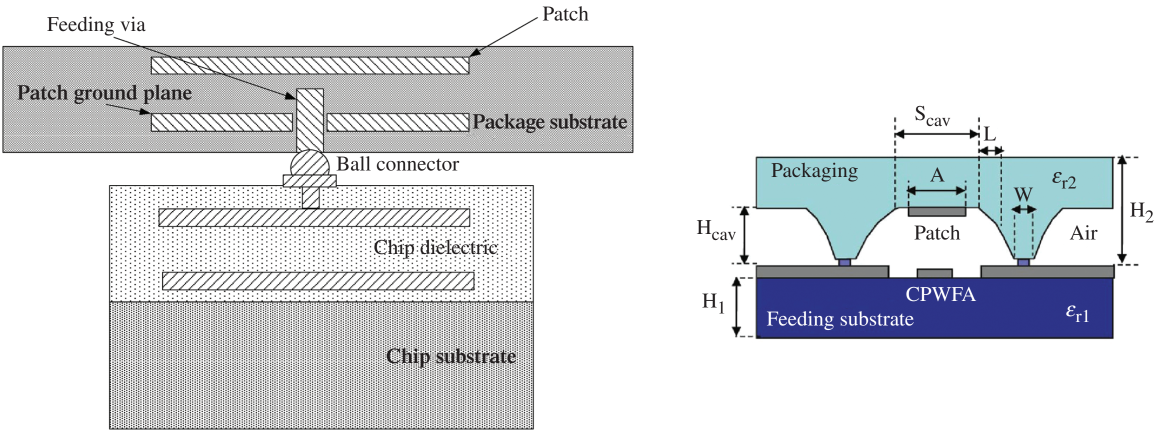

Figure 4.27 There are various methods for feeding an in-package patch from a packaged chip. The ball connector (left) may, for example, be used in a flip chip connection. [KLN+11] found that this type of ball connector improves with a smaller radius of the ball and a smaller metal pad for the ball (represented here as a small rectangular piece of metal below the ball) [right portion from [HRL10] © IEEE].

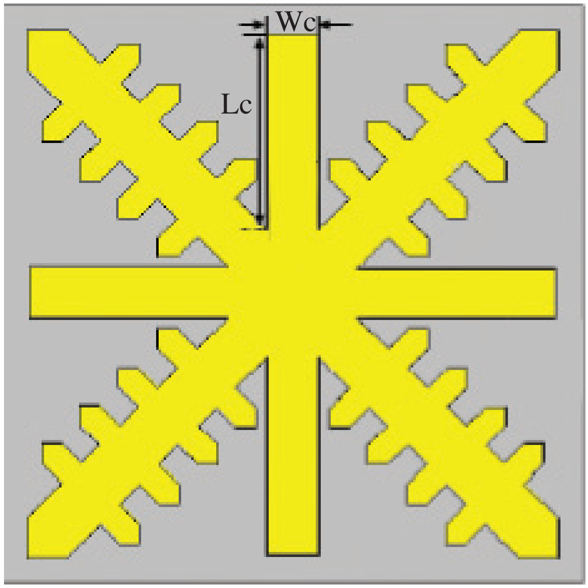

Figure 4.34 This element was cascaded periodically below an on-chip microstrip antenna to form an AMC to achieve a gain of −1.5 dBi [from [CGLS09] © IEEE].

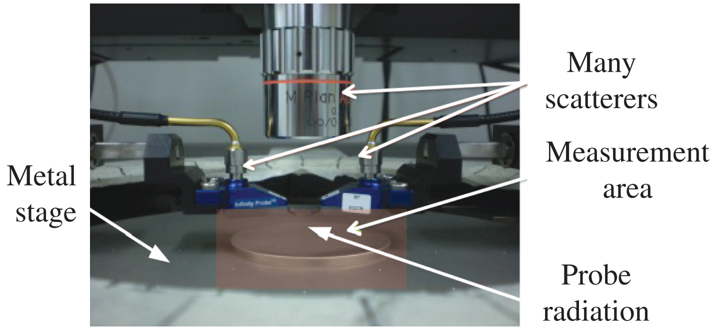

Figure 4.58 A probe station is often used to characterize mmWave antennas. These measurements may be inaccurate due to radiation from probes and scattered fields from the many surrounding metal objects [from [MBDGR11] © IEEE].

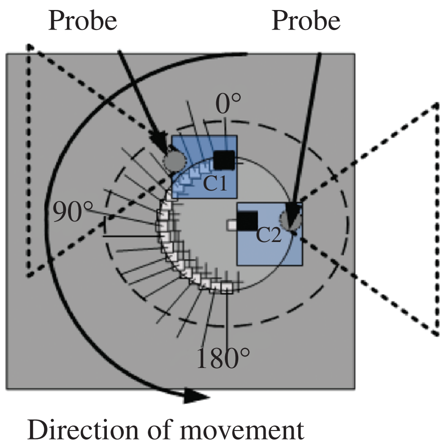

Figure 4.59 The two antennas were swept in angle across each other. The chips on which the antennas were fabricated are represented by squares, and the antennas are represented by smaller black boxes [from [MBDGR11] © IEEE].

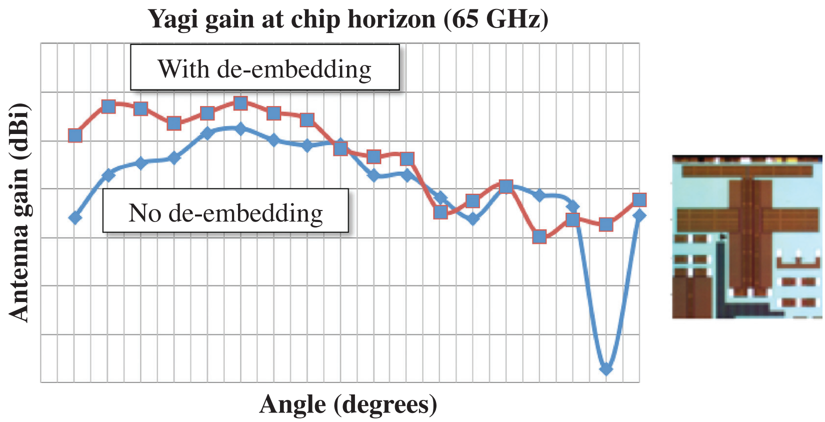

Figure 4.60 The de-embedding method indicates that the on-chip Yagi pattern was distorted by the presence of other nearby metal structures [from [MBDGR11] © IEEE].

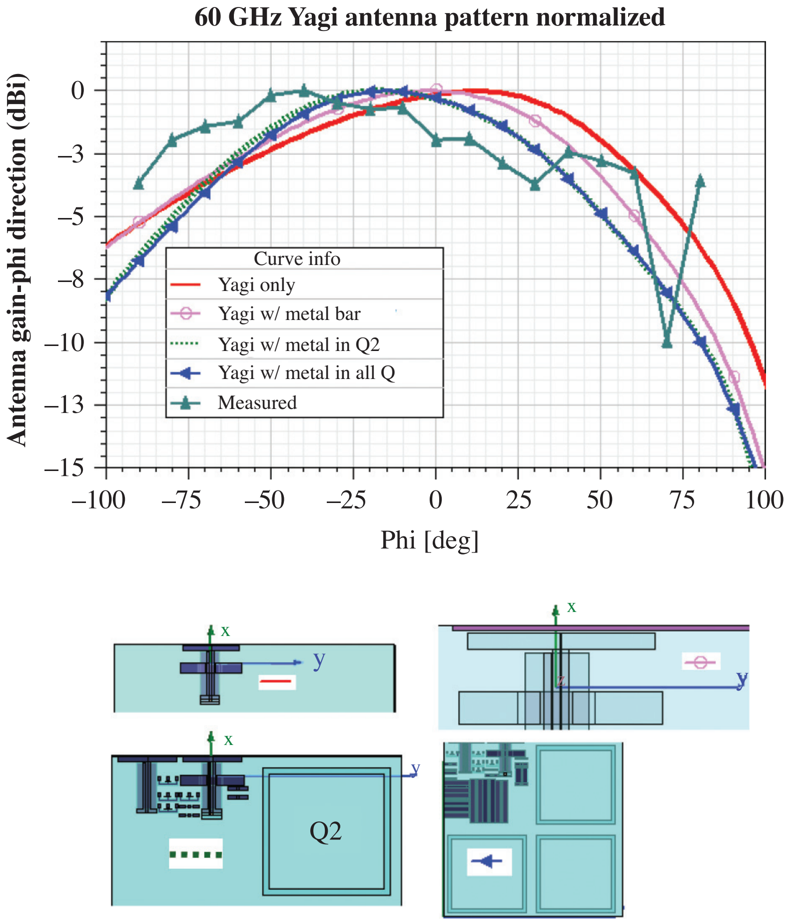

Figure 4.61 Simulations confirmed measurements that indicated the distortion of the antenna pattern was caused by surrounding metal structures. This indicates that isolation between integrated antennas and other nearby structures on the chip or in the package is key to successful design [from [MBDGR11] © IEEE].

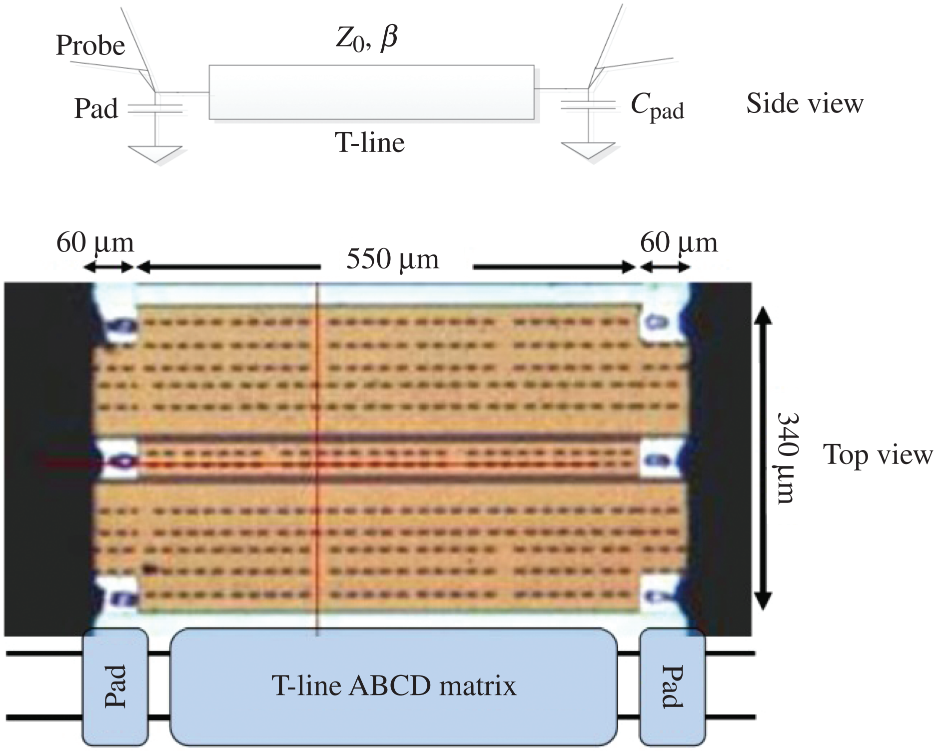

Figure 5.7 The S-parameters of a transmission line can be used to determine the effective relative permittivity and loss tangent of a CMOS process. The effects of the probe pads must be de-embedded for this measurement to be accurate [from [GJRM10] © IEEE].

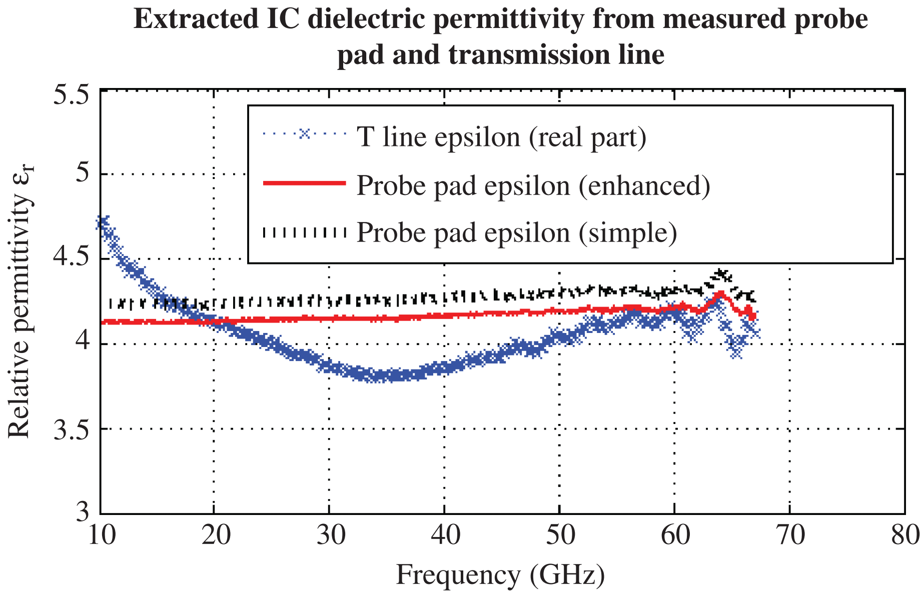

Figure 5.8 The effective relative permittivity may be measured in a number of ways and is a vital parameter for the design of passive structures [from [GJRM10] © IEEE].

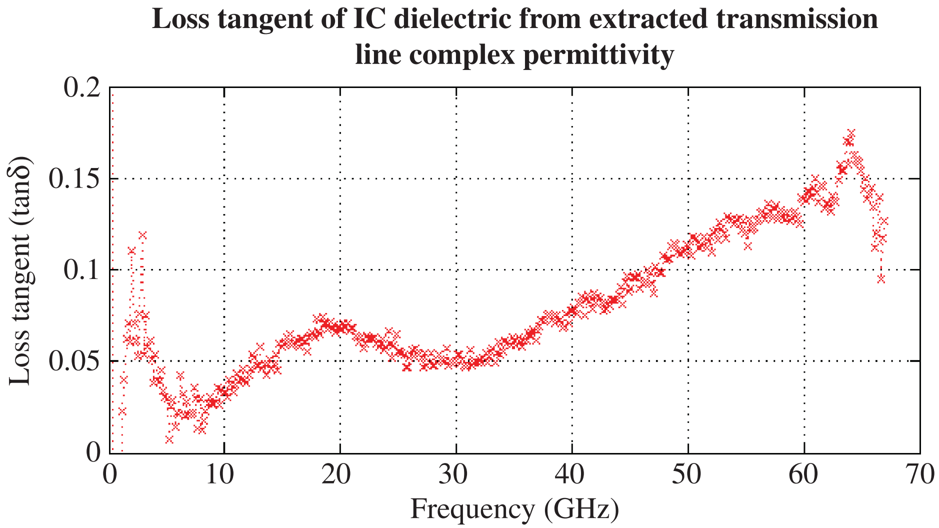

Figure 5.9 The effective loss tangent is a vital parameter to predict loss of passive structures [from [GJRM10] © IEEE].

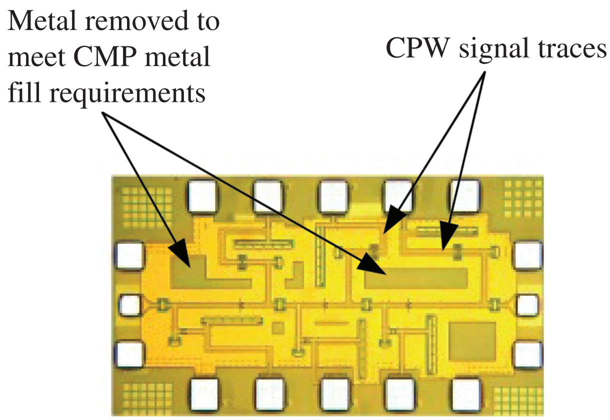

Figure 5.26 A common ground plane is evident in this layout. Portions of the metal have been removed in order to meet metal fill requirements [based on a figure from [MTH$^+$08] © IEEE].

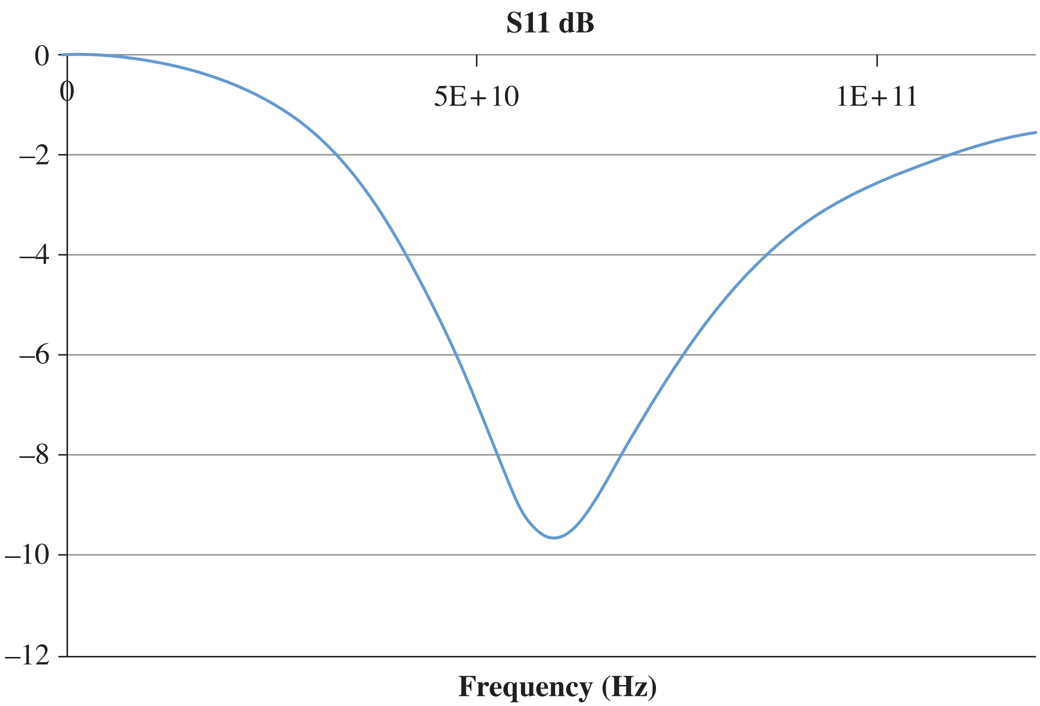

Figure 5.42 The amplifier accepts energy in only a certain range of frequencies.

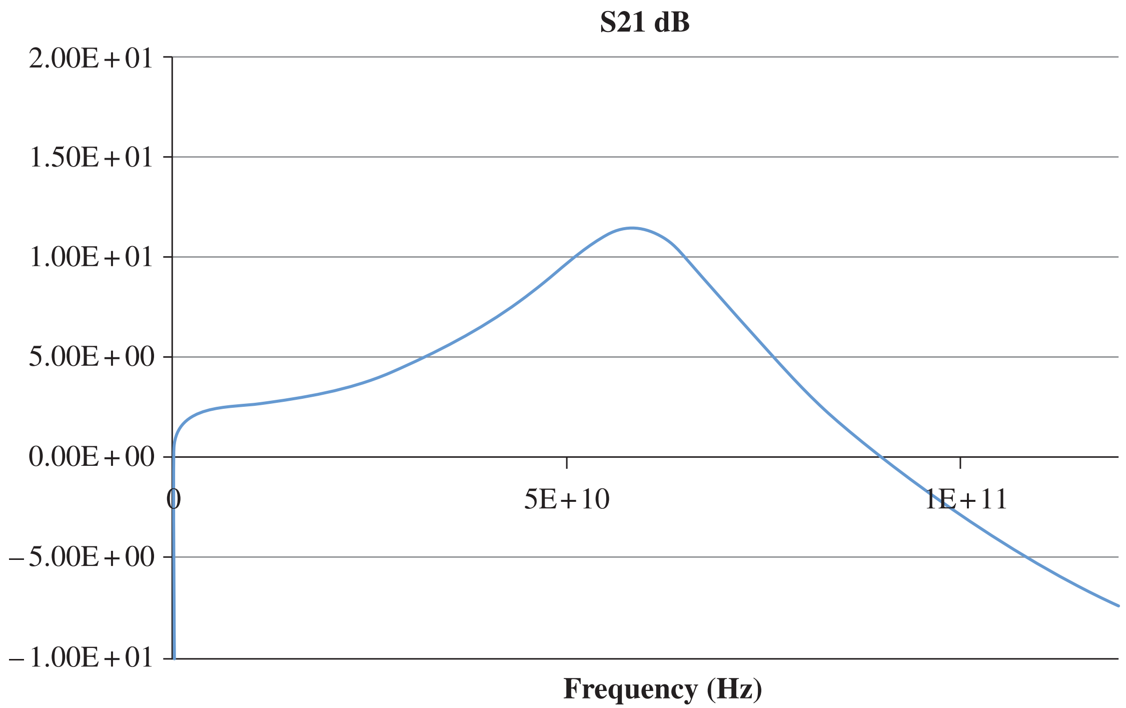

Figure 5.43 The value of S_{21} gain is only high in a certain band of frequencies.

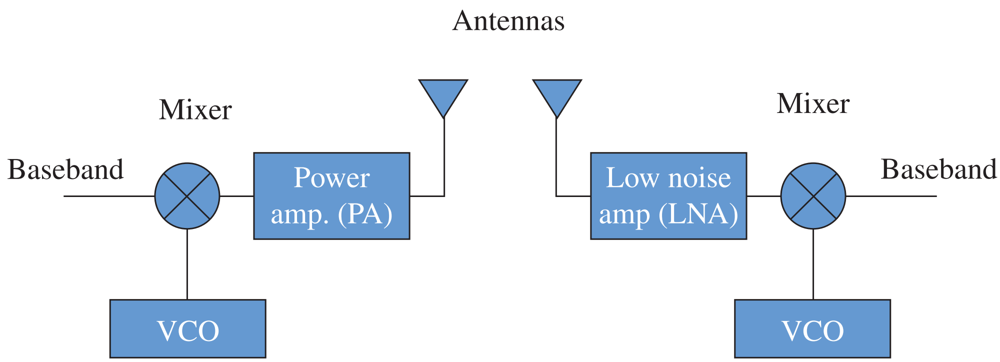

Figure 5.44 A direct conversion architecture for a transmitter and receiver. This is a popular architecture for today's cellphones. In many designs, the VCO is part of a phase-locked loop (PLL).

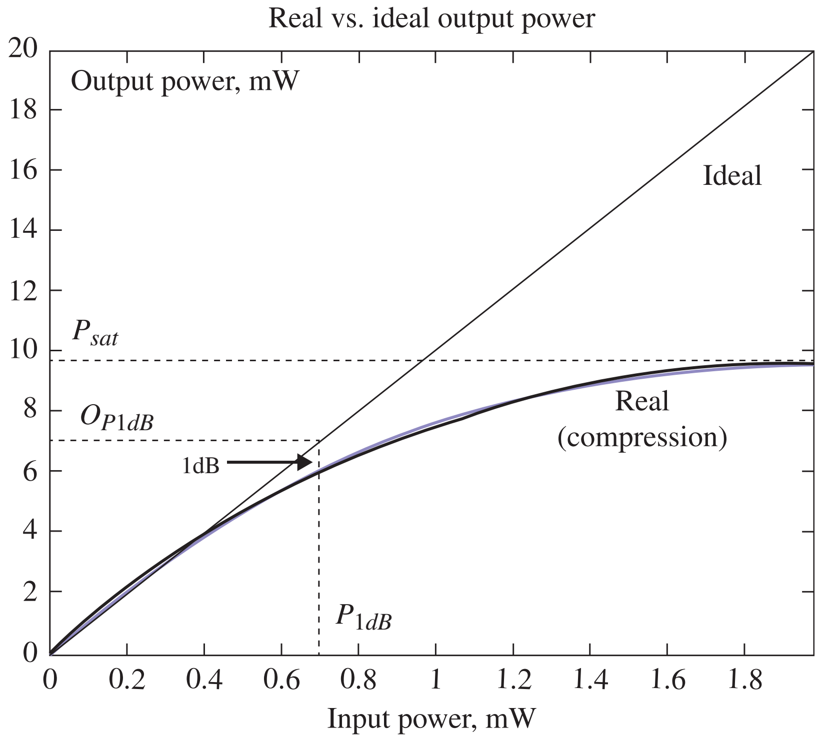

Figure 5.46 The non-linearity of most devices results in the compression of the output power of the fundamental harmonic.

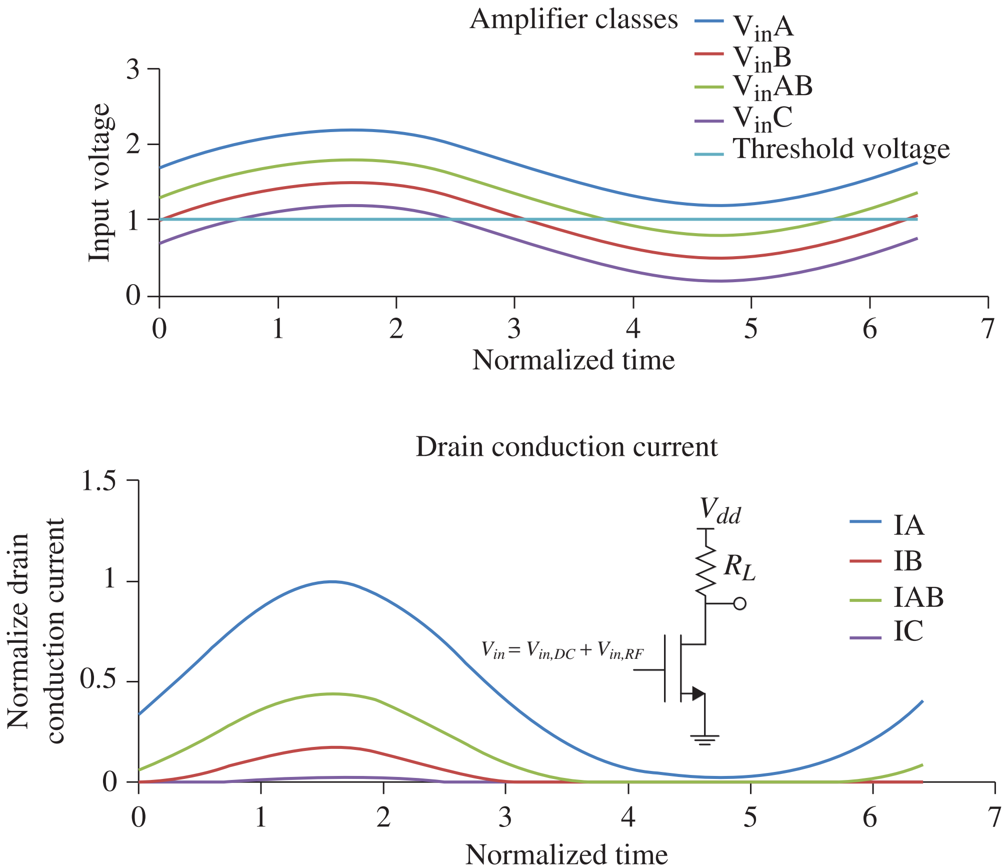

Figure 5.50 The bias point of the amplifier determines the amplifier's class. Class A amplifiers conduct current over the entire period. Class B amplifiers conduct over half the period, Class C conduct over less than half the period, and Class AB conduct over more than half the period, but less than the entire period.

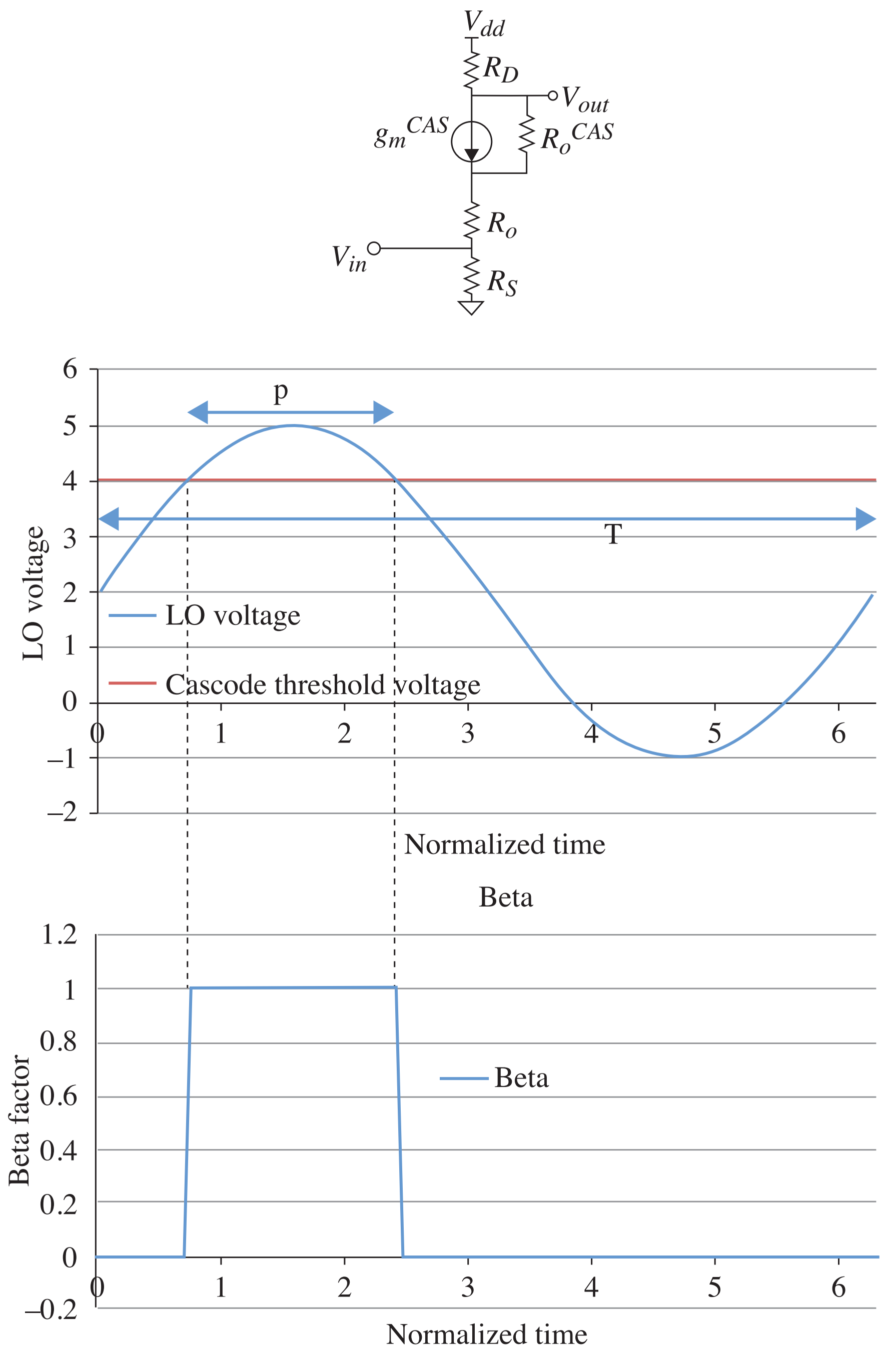

Figure 5.60 Based on the nature of the LO signal magnitude and bias point, we may treat the transconductance of the cascode as a square wave that switches on and off. This figure shows how the gain of the switching mixer is gated by the LO voltage to create the switching effect of the mixer. This approach is used in double balanced mixers, such as Gilbert cells.

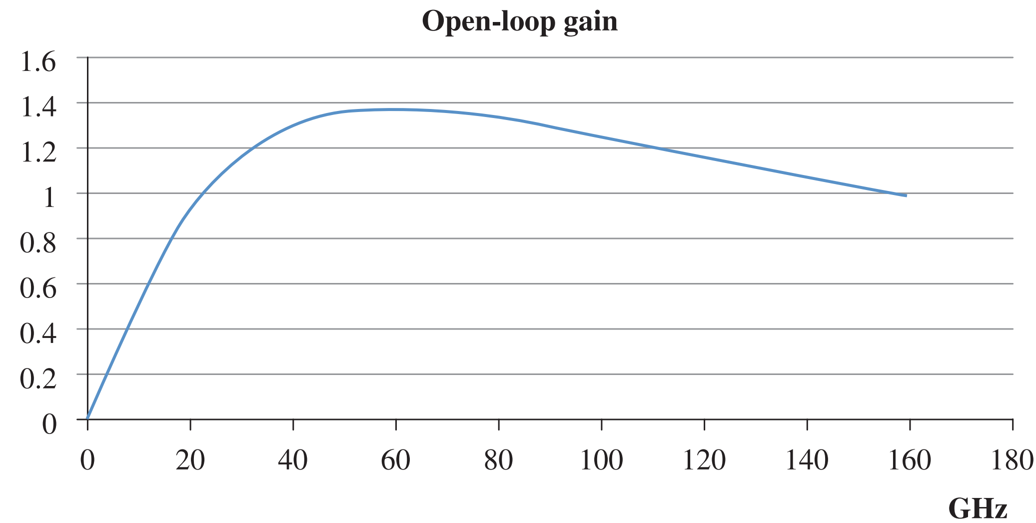

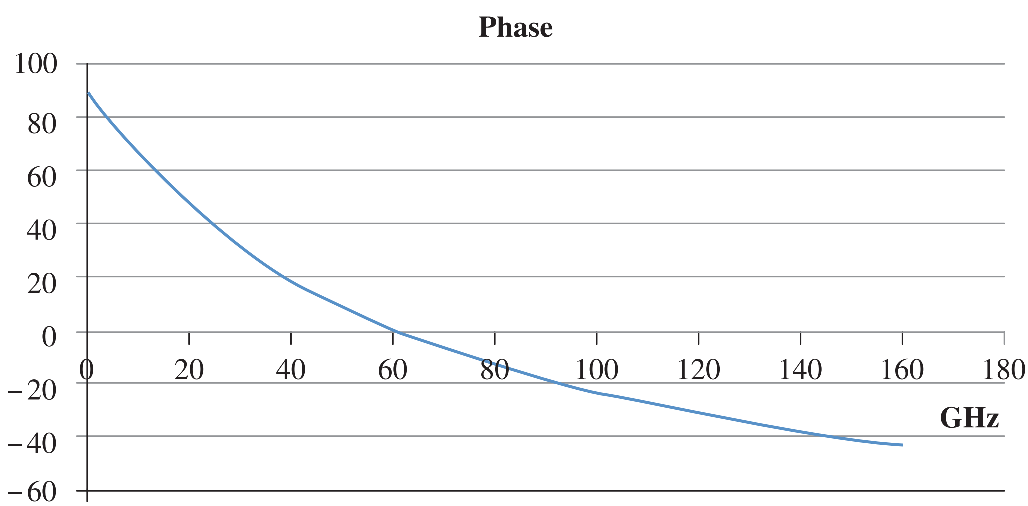

Figure 5.63 The open-loop gain (top) and phase shift (bottom) of the oscillator in Fig. 5.62.

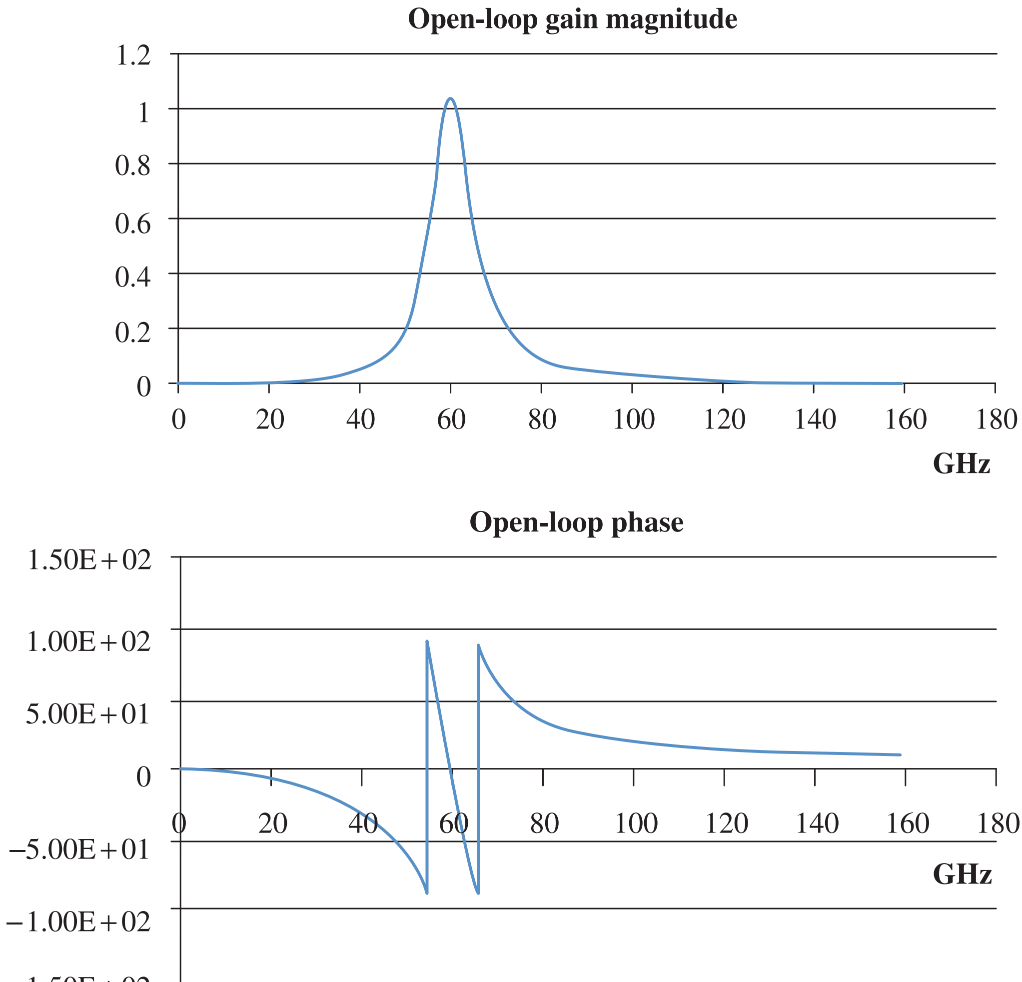

Figure 5.65 The gain and phase of a simple LC tank oscillator.

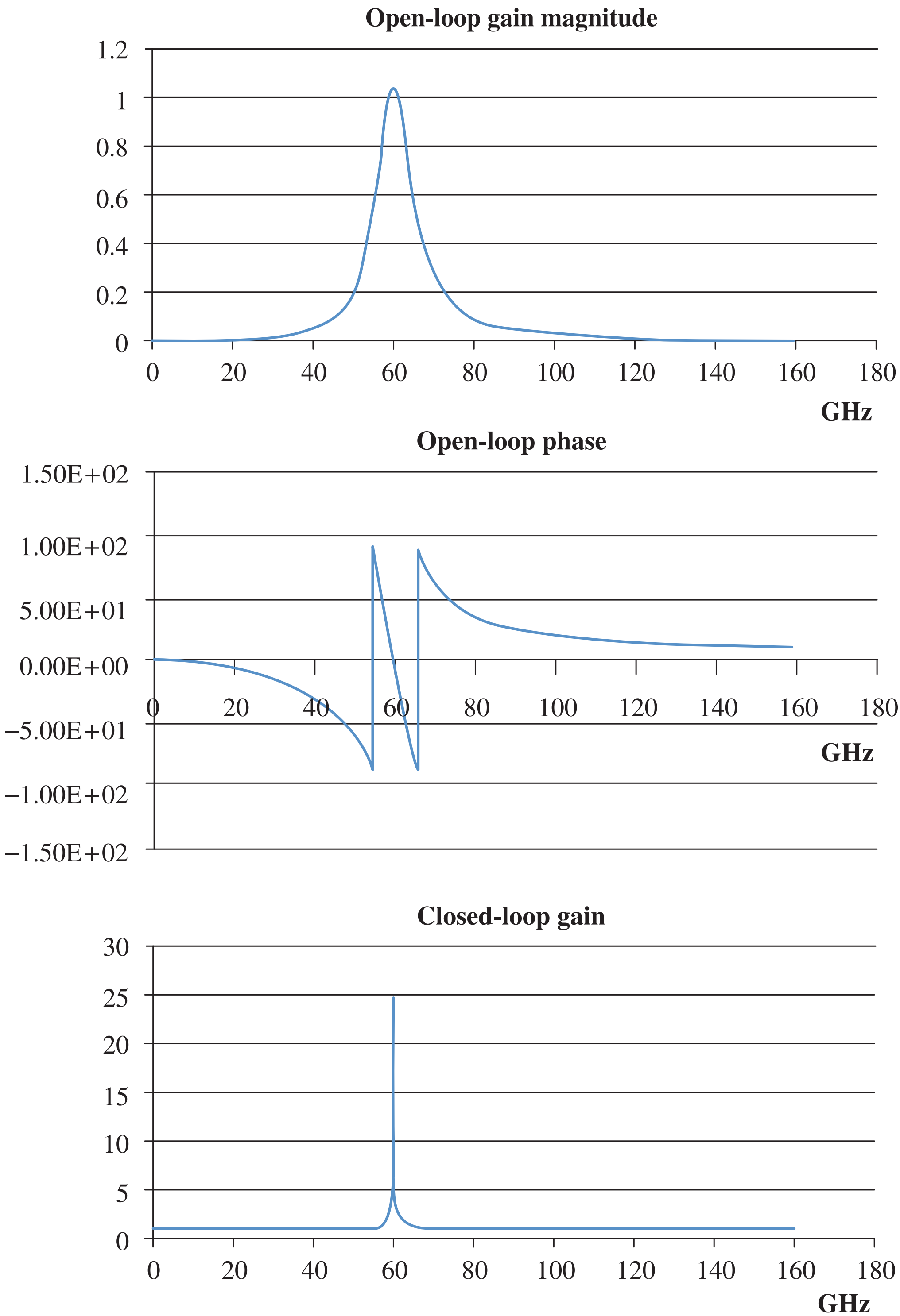

Figure 5.71 For real-world oscillator circuits, the output spectrum will be polluted by power at frequencies other than the intended operating frequency.

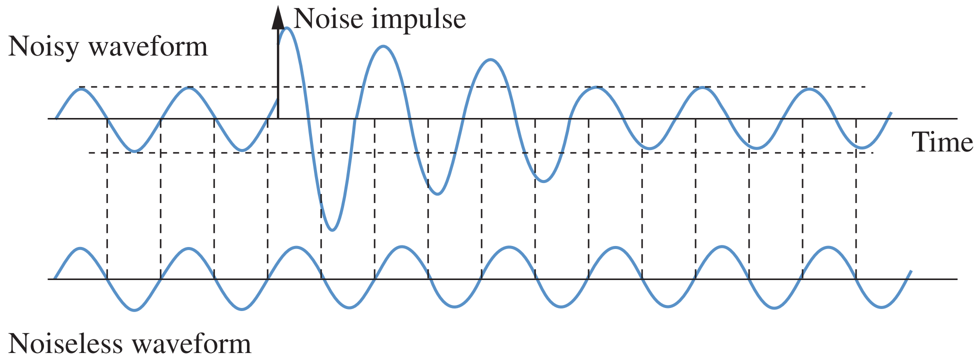

Figure 5.72 Noise events, such as the noise impulse represented here, will affect both the amplitude and phase of a circuit. In general, the amplitude impulse response of the circuit will act to remove amplitude noise over time. But phase noise persists, as is evident when we compare the phase of the noisy waveform to the noiseless waveform.

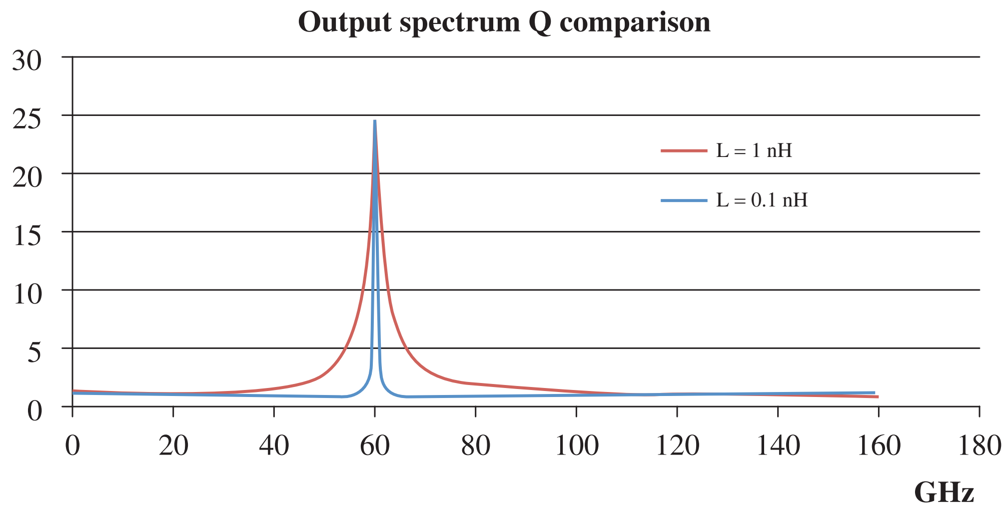

Figure 5.73 The output spectrum of an LC oscillator becomes more spectrally pure as the quality factor of the tank increases.

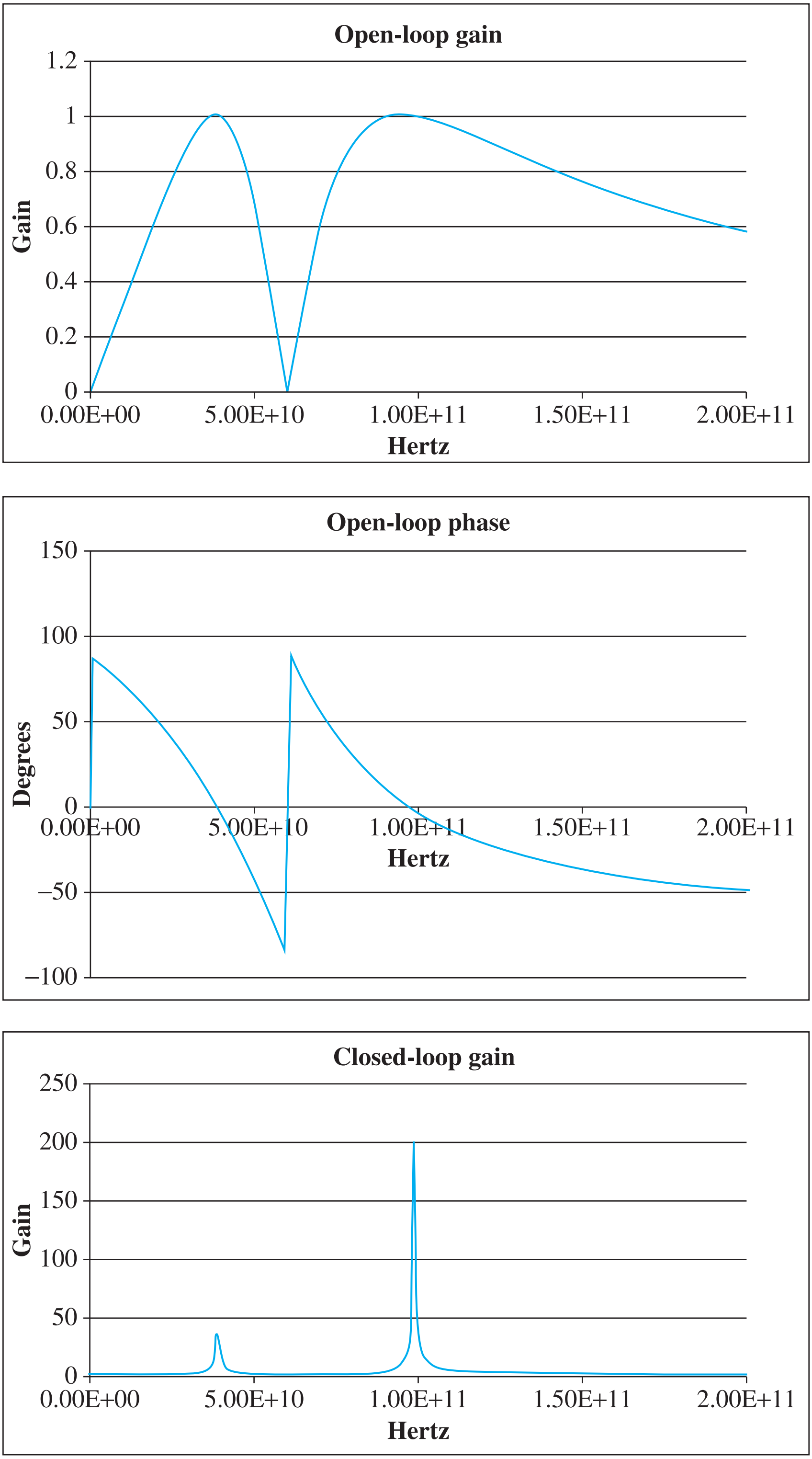

Figure 5.76 The transfer characteristics of a subharmonic oscillator.

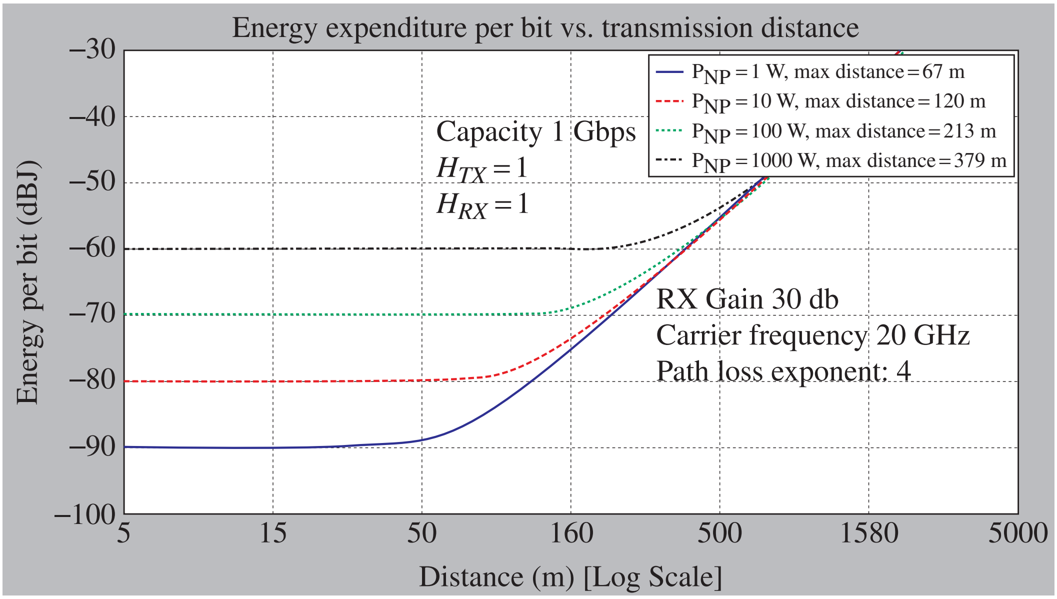

Figure 5.86 For a system with high signal path efficiency and high non-path power consumption, we see that the energy expenditure per bit is dominated by non-path power, indicating little advantage to shortening transmission distances [from [MR14b] © IEEE].

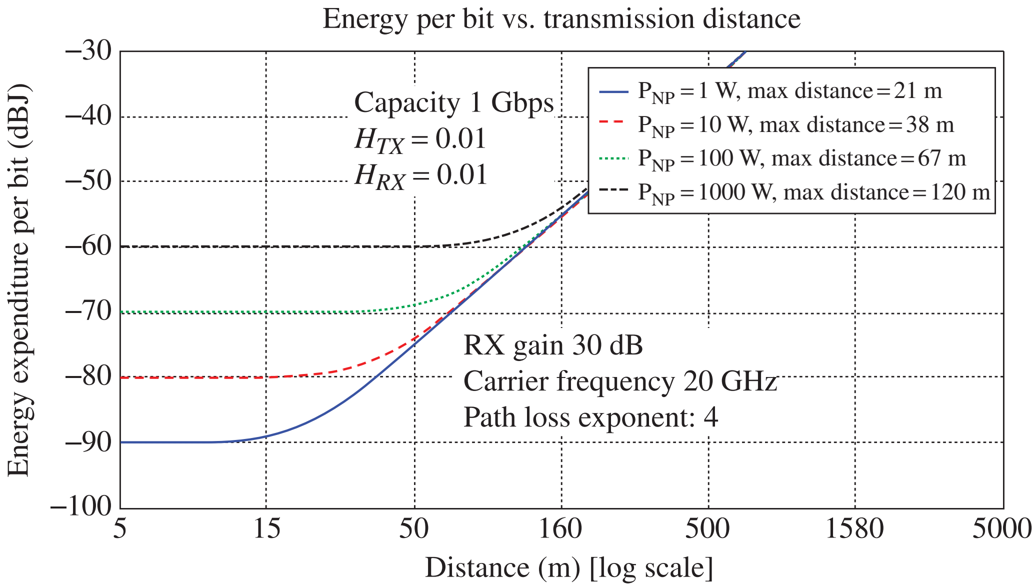

Figure 5.87 When signal path components are less efficient, as illustrated here, then shorter transmission distances start to become advantageous, as signal path power starts to represent a larger portion of the power expenditure per bit [from [MR14b] © IEEE].

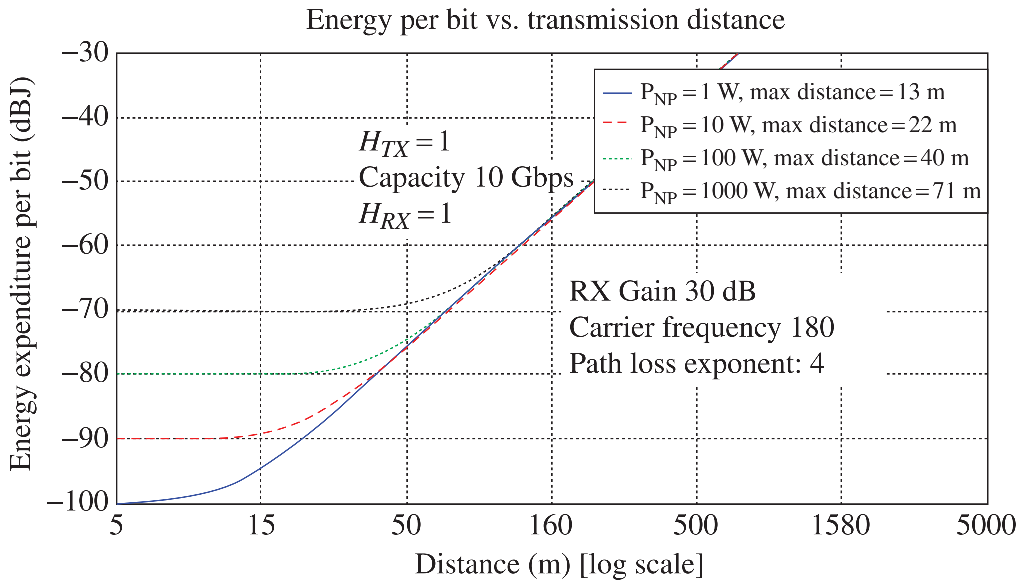

Figure 5.88 A higher frequency system that can provide a much higher bit rate capacity without substantially increasing non-path power consumption may result in a net reduction in the energy price per bit [from [MR14b] © IEEE].

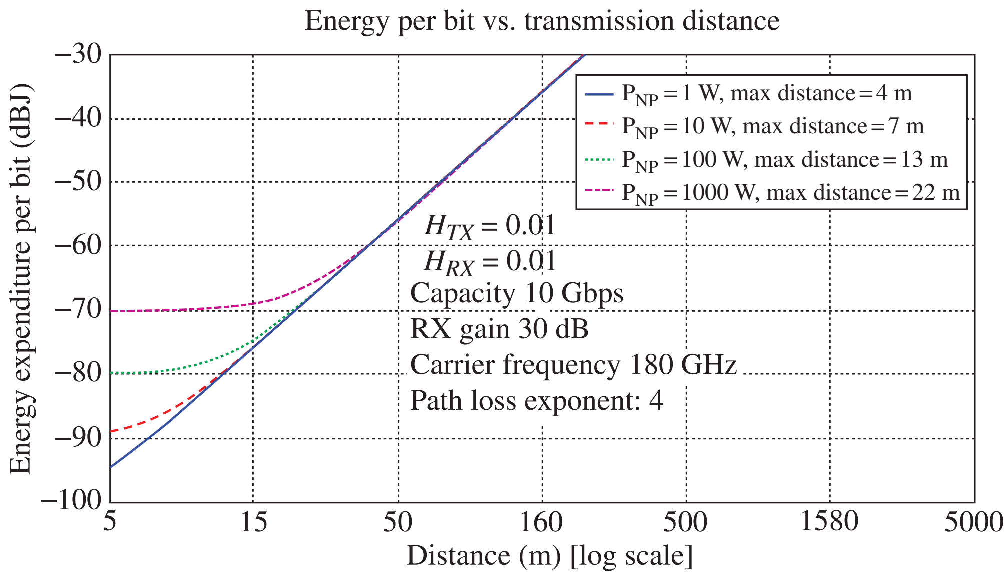

Figure 5.89 Lower efficiencies of signal path components motivate the use of shorter transmission distances [from [MR14b] © IEEE].

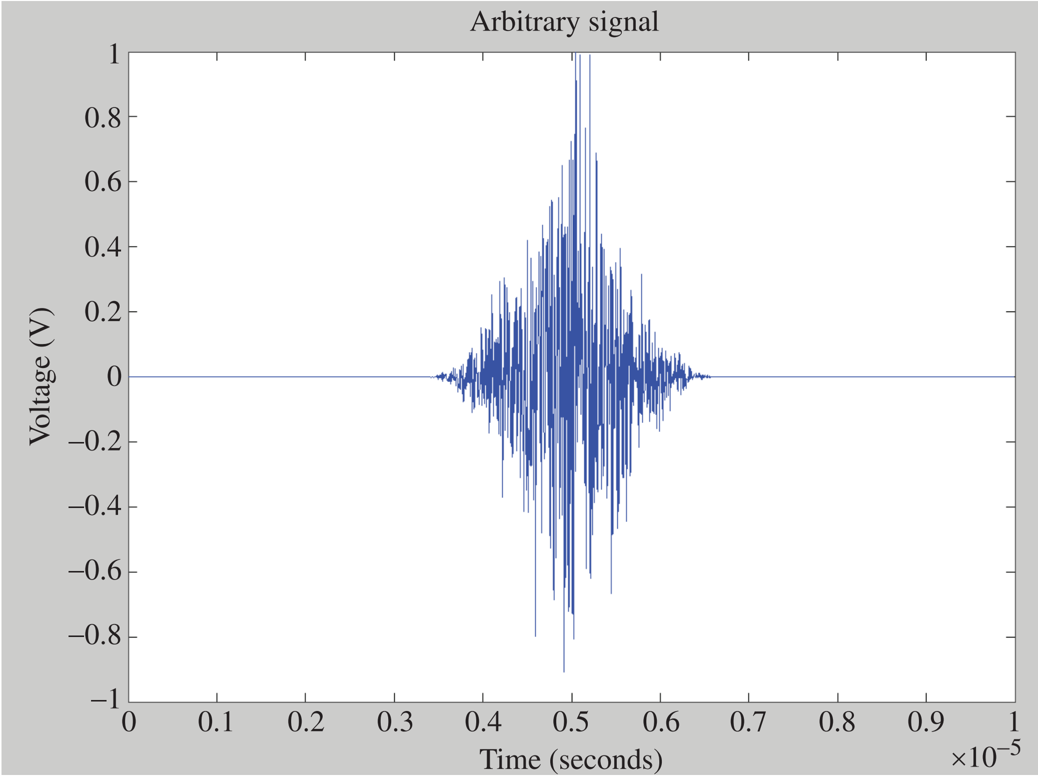

Figure 6.1 An arbitrary baseband analog signal having an approximate bandwidth of 100 MHz.

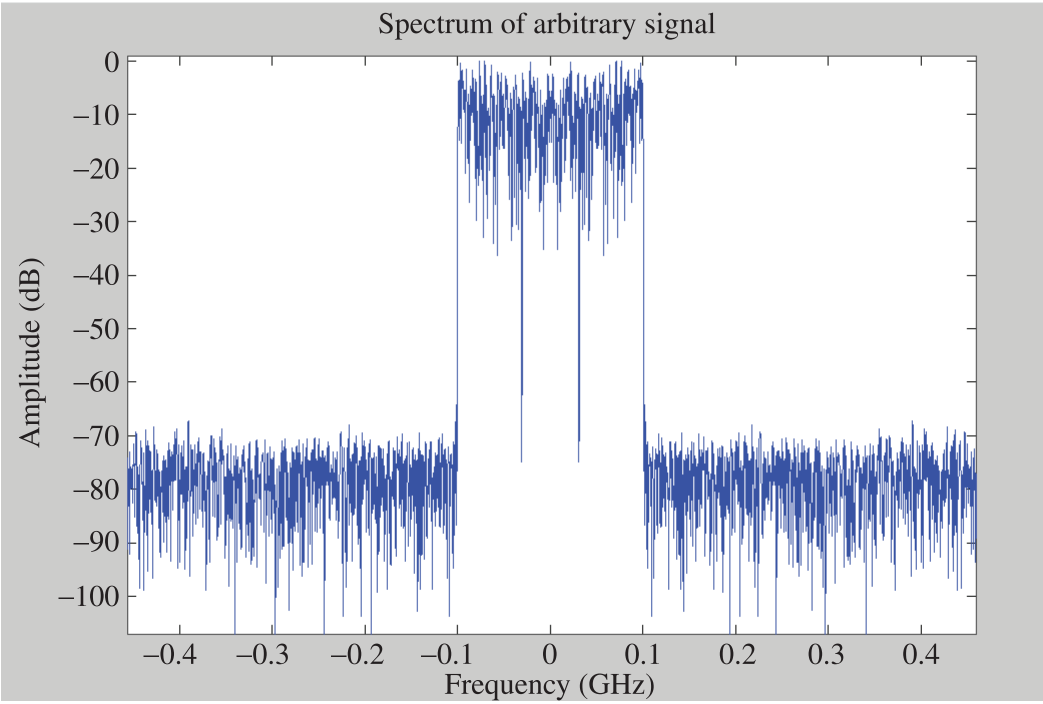

Figure 6.2 The spectrum of the arbitrary analog waveform shown in Fig. 6.1. The spectrum has been normalized such that the strongest spectral component has an amplitude of 0 dB.

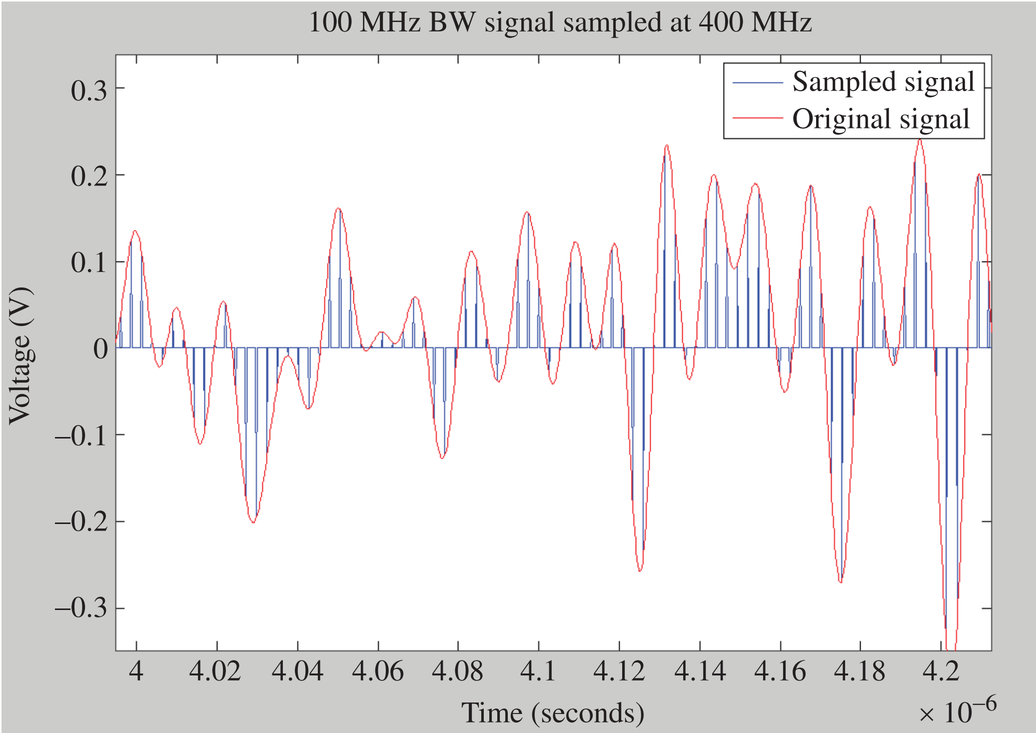

Figure 6.3 A zoomed-in version of the arbitrary signal in Fig.6.1 showing how it has been sampled. The bandwidth (BW) of the original signal is 100 MHz, and the sampling rate is 400 MHz.

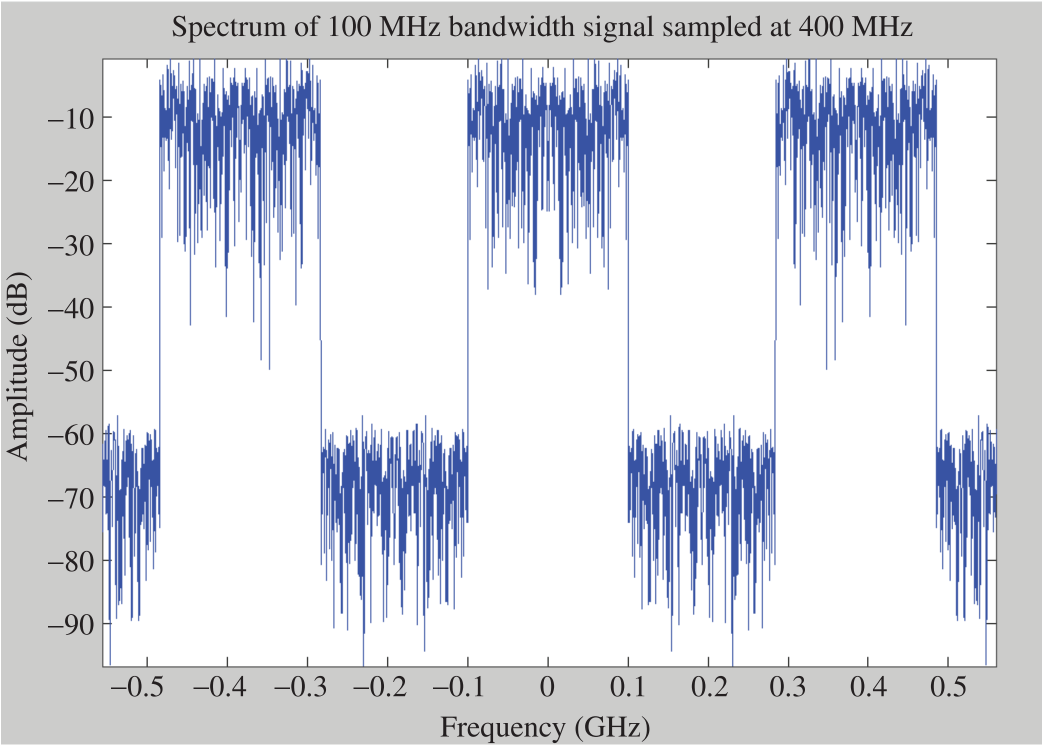

Figure 6.4 The result of sampling the signal in Fig. 6.1 in the time domain is to make the spectrum periodic in the frequency domain.

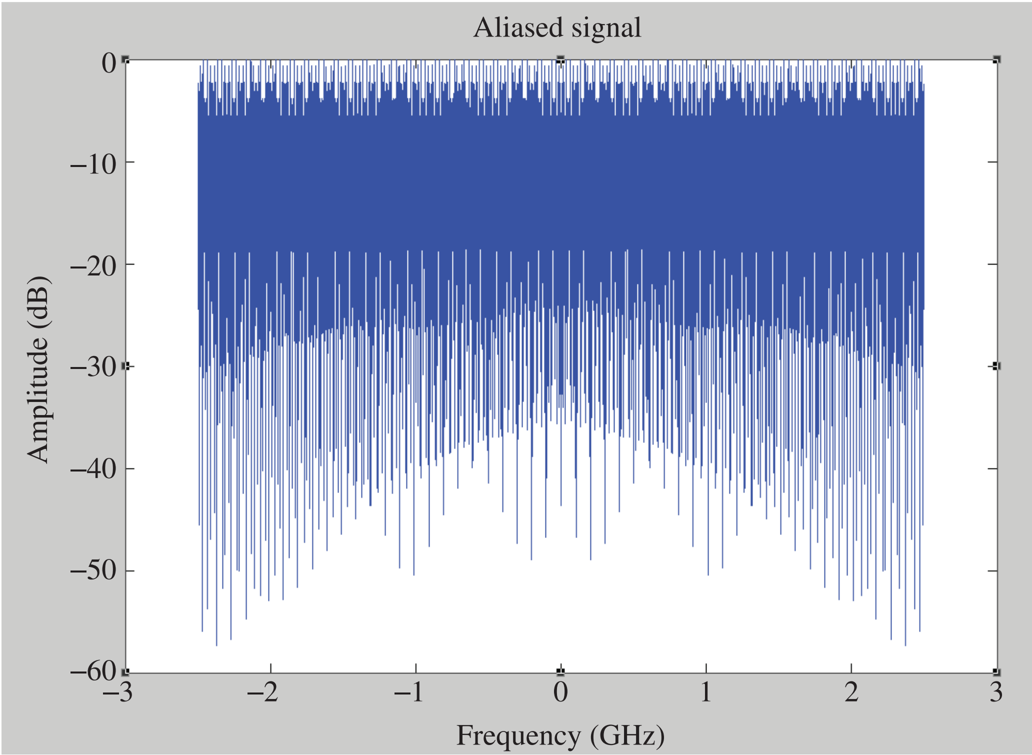

Figure 6.5 If the signal of Fig. 6.1 with a baseband bandwidth of 100 MHz is sampled at 100 MHz, the result is an aliased signal. In the frequency domain, overlapping copies of the original signal's spectrum completely distort the resulting sampled signal.

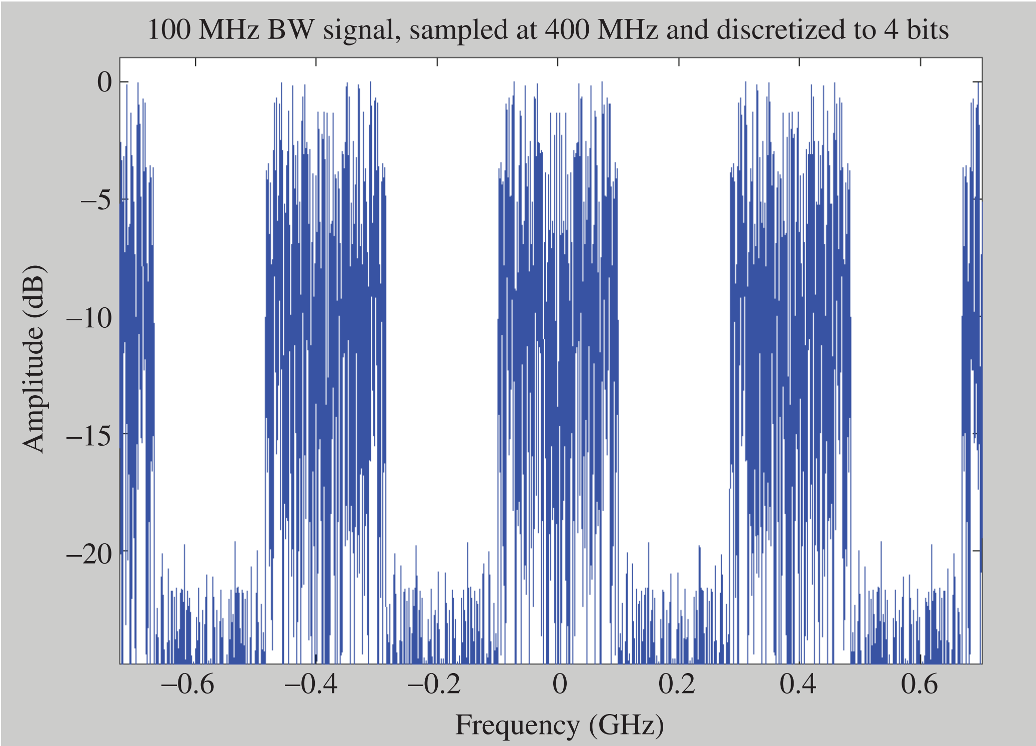

Figure 6.6 Quantizing the signal of Fig. 6.1 with 4 bits reduces the dynamic range to 24 dB.

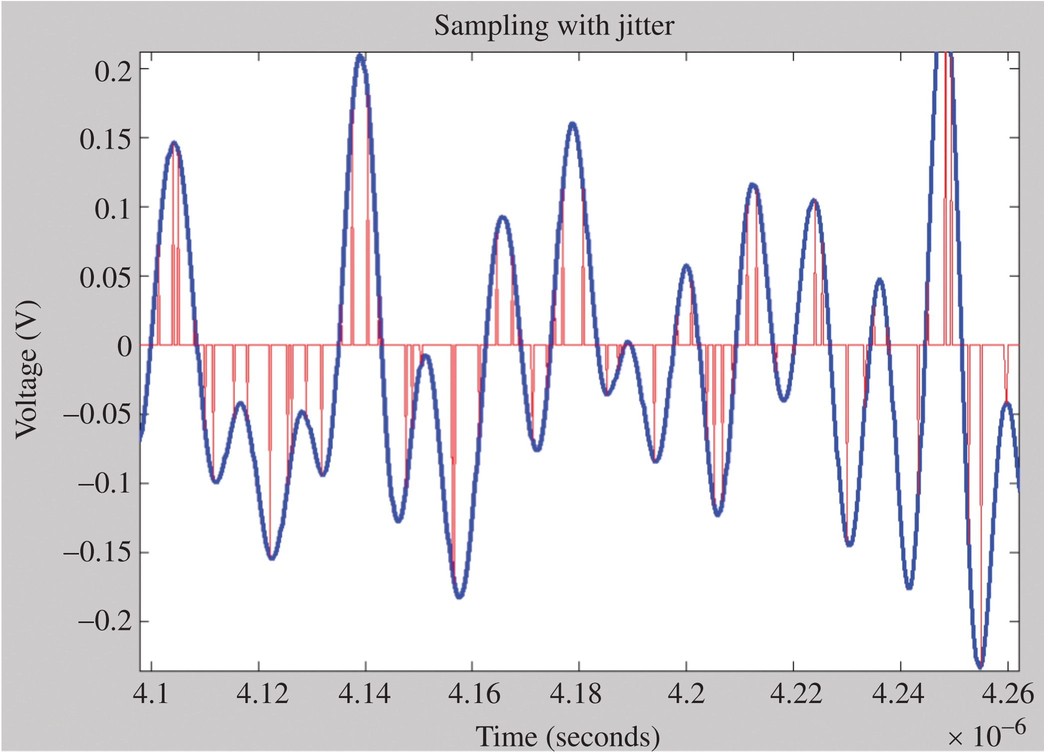

Figure 6.7 An example of sampling with jitter, where uncertainty in the time interval between samples results in decreased dynamic range.

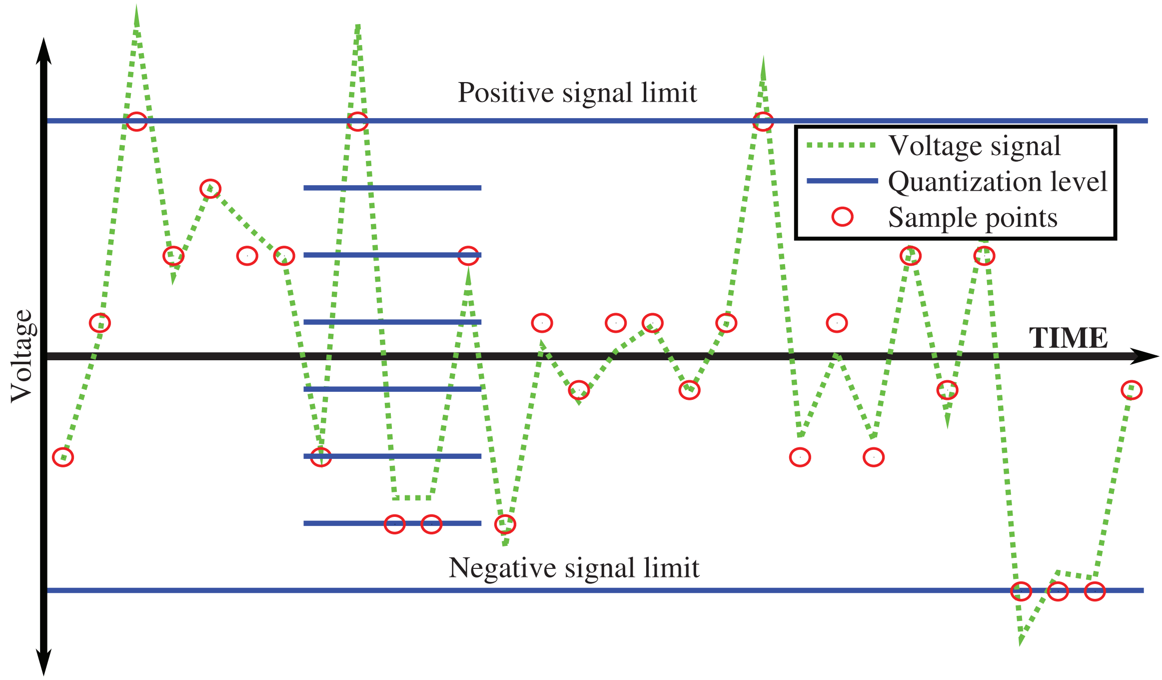

Figure 7.2 Amplitude thresholding and quantization for a 3-bit ADC with uniform quantization levels in the receiver. In a wireless communications receiver, ADCs quantize both the in-phase and quadrature channels independently. Automatic gain control (AGC) is used to normalize the energy of the received complex baseband signal so that the ADC thresholds and quantization levels can be fixed (i.e., do not depend on fading). As shown in Chapter 3, fading will be less pronounced with directional antennas.

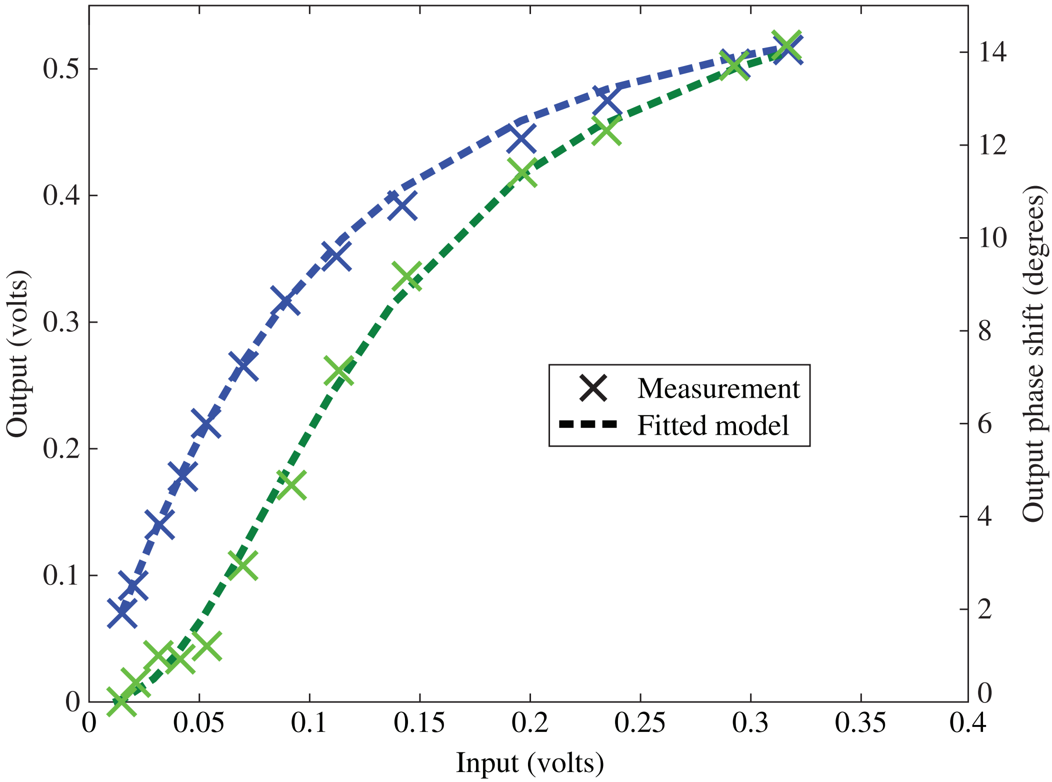

Figure 7.3 AM-PM and AM-PM measurements and modified Rapp model for a CMOS 65 nm PA. For more detail on mmWave PA statistics, please consult the tables provided in Chapter 5 [plot created with data from [EMT+09] © IEEE].

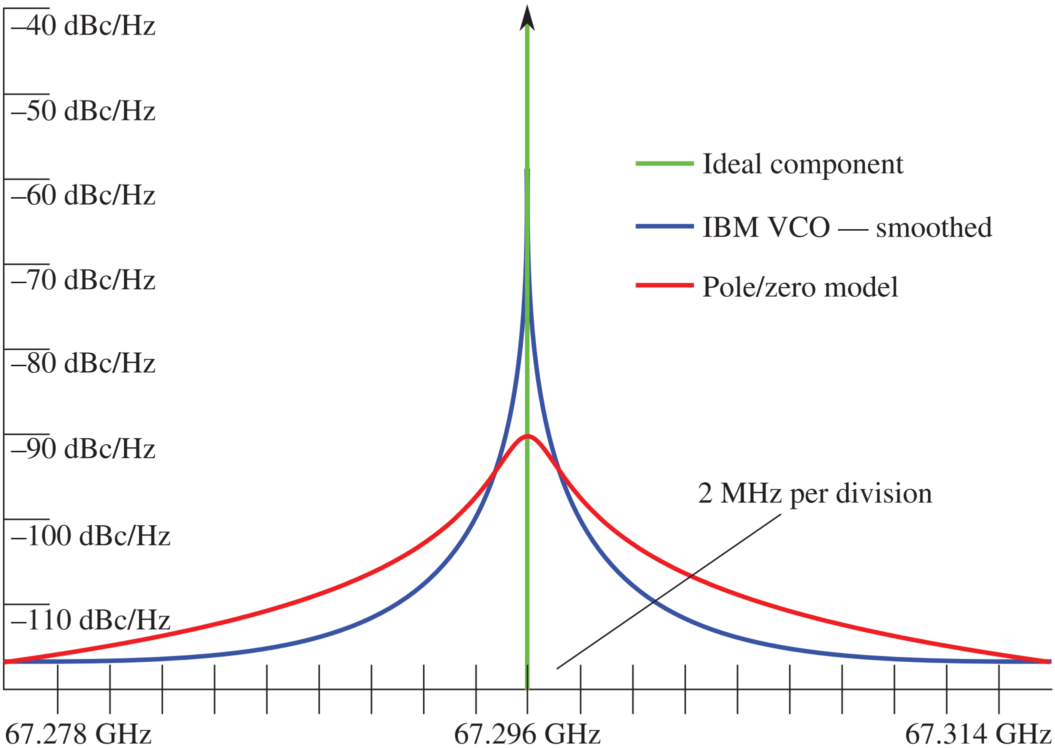

Figure 7.4 Measured power spectral density of single sideband (SSB) VCO output for desired signal at 67.3 GHz. PSD measurements normalized to desired carrier output power (represented by dBc/Hz). A similar figure is shown in Chapter 5. Here, however, we have included a comparison to a pole/zero model that facilitates physical layer performance simulations [data taken from [FRP+05] and smoothed to create the plot © IEEE].

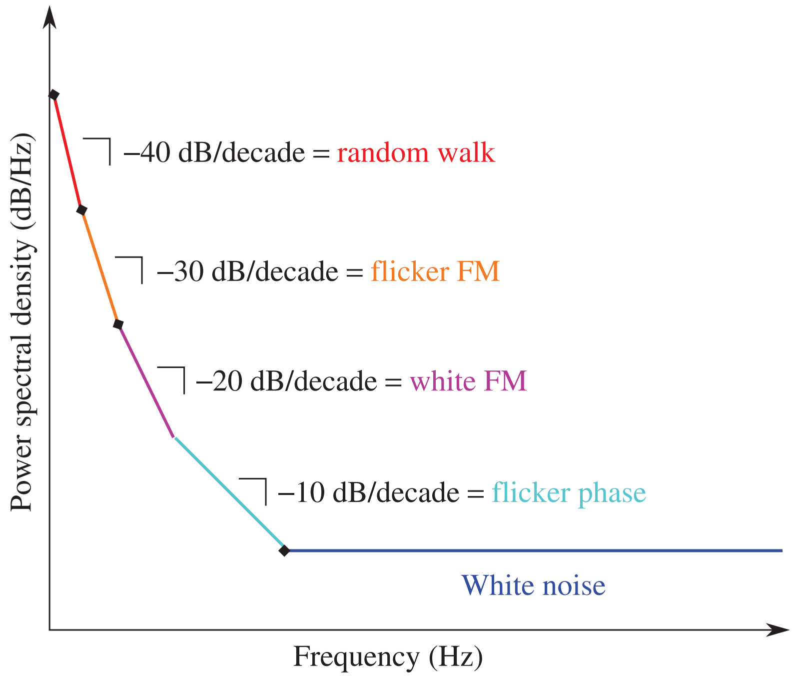

Figure 7.5 Different phase noise effects and their contribution to the power spectral density in the Leeson model [Lee66].

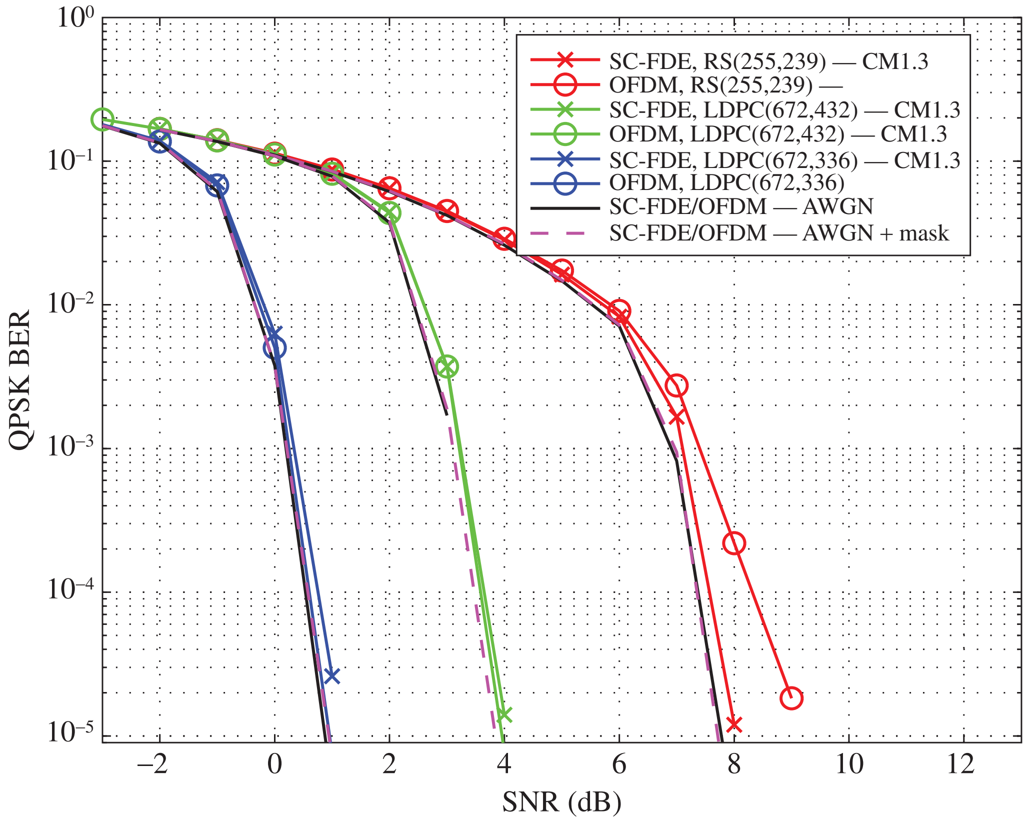

Figure 7.6 Bit error rate as a function of SNR for OFDM and SC-FDE in AWGN and LOS channels with QPSK constellations. The coding options are RS(255,239) and LDPC(672,336). The 802.15.3c spectral mask is added to the AWGN channel to demonstrate bandwidth conservation of each modulation strategy. Hardware impairments are not considered.

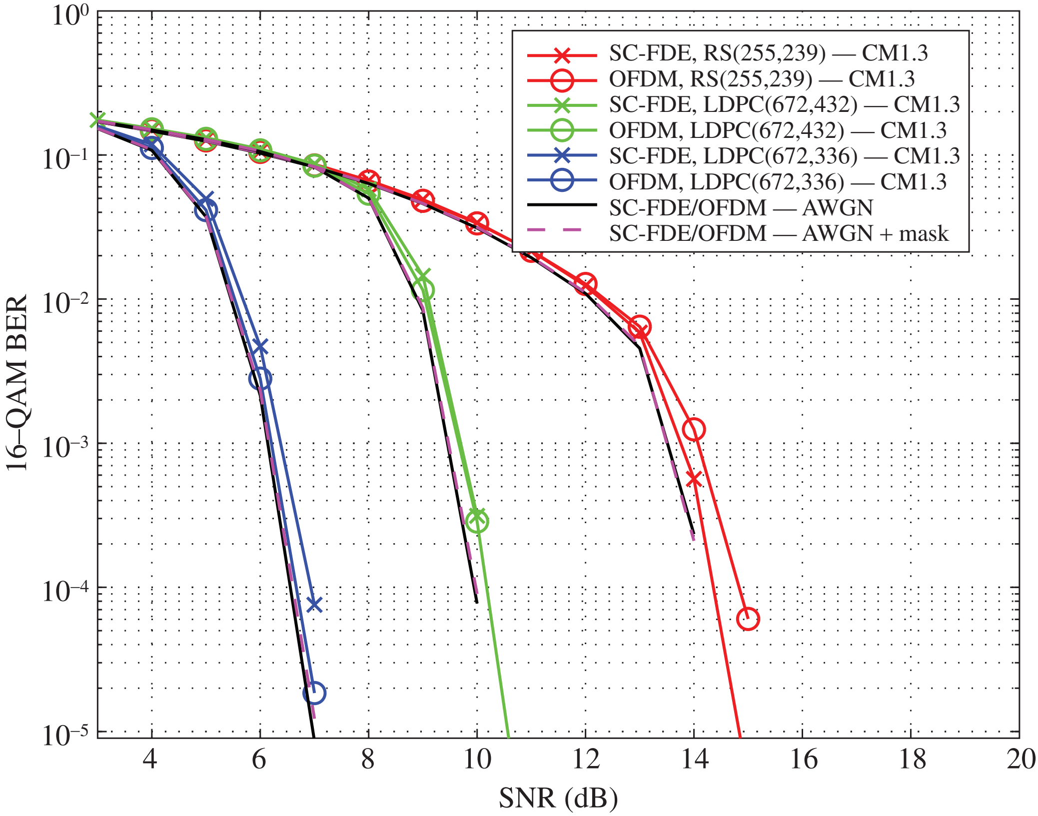

Figure 7.7 Bit error rate as a function of SNR for OFDM and SC-FDE in LOS CM1.3 channels with 16-QAM constellations. Hardware impairments are not considered.

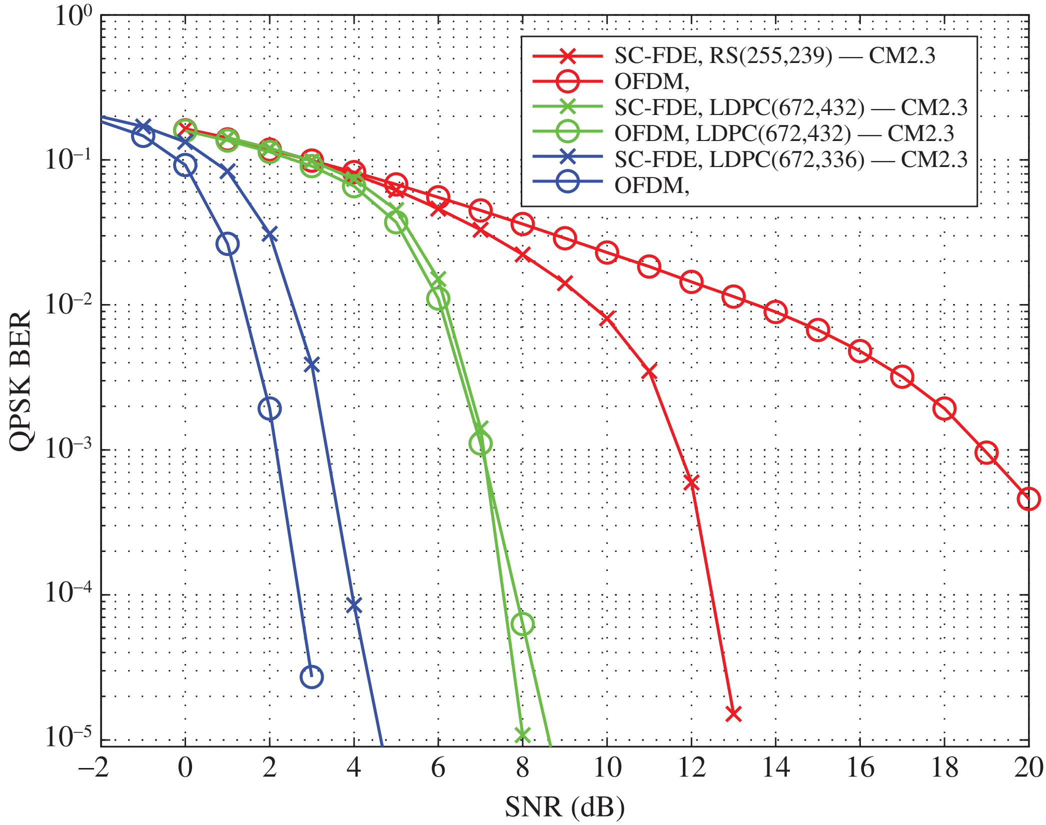

Figure 7.8 Bit error rate as a function of SNR for OFDM and SC-FDE in NLOS CM2.3 channels with QPSK constellations. No hardware impairments are considered.

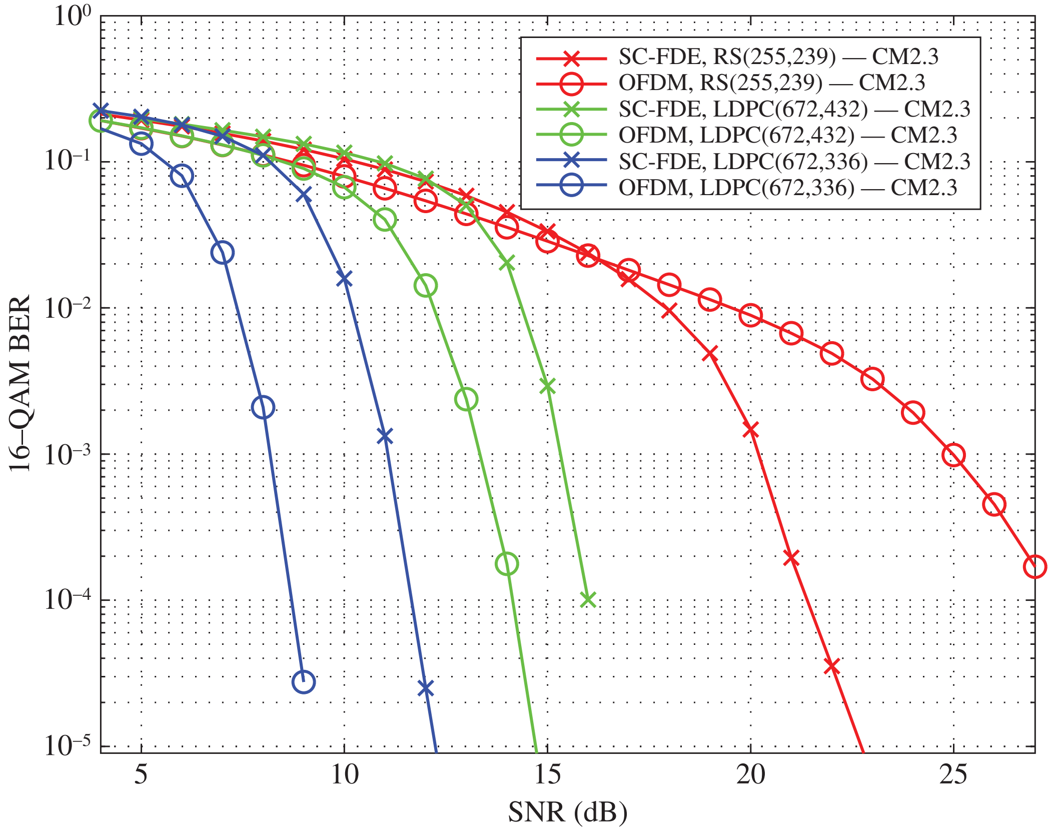

Figure 7.9 Bit error rate as a function of SNR for OFDM and SC-FDE in NLOS CM2.3 channels with 16-QAM constellations. No hardware impairments are considered.

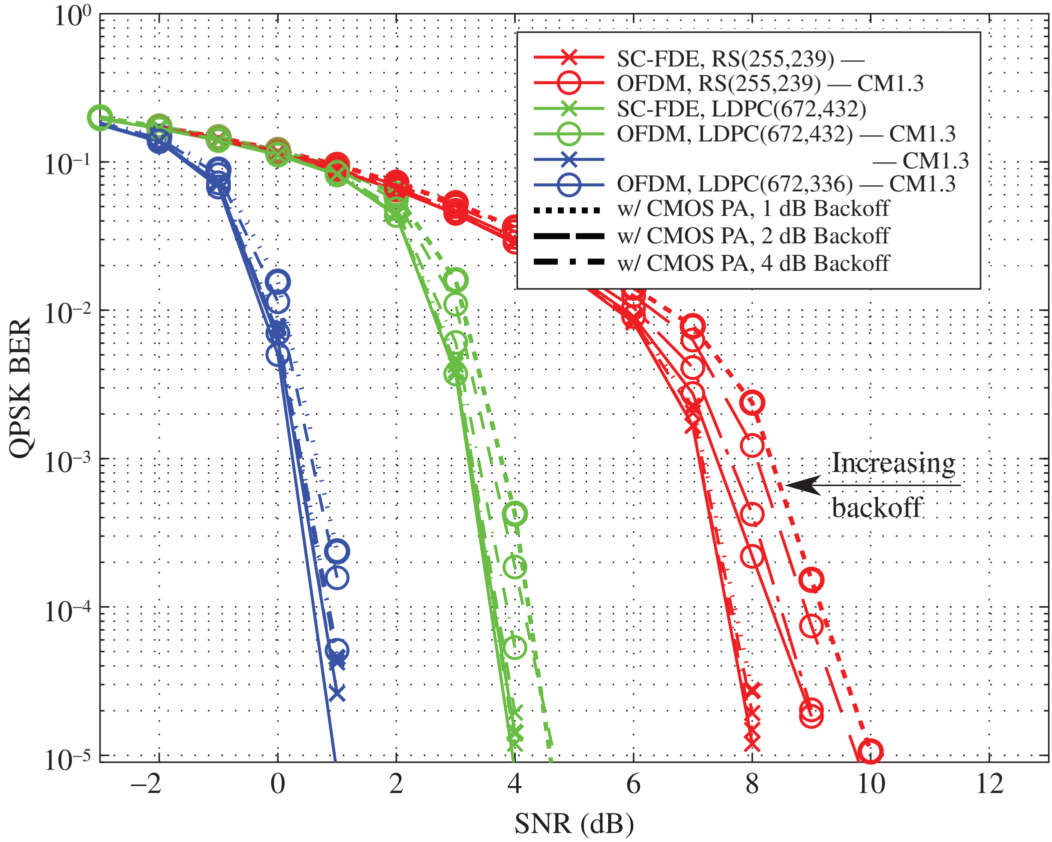

Figure 7.10 Bit error rate as a function of SNR for OFDM and SC-FDE in LOS CM1.3 channels and CMOS PA non-linearity with QPSK constellations.

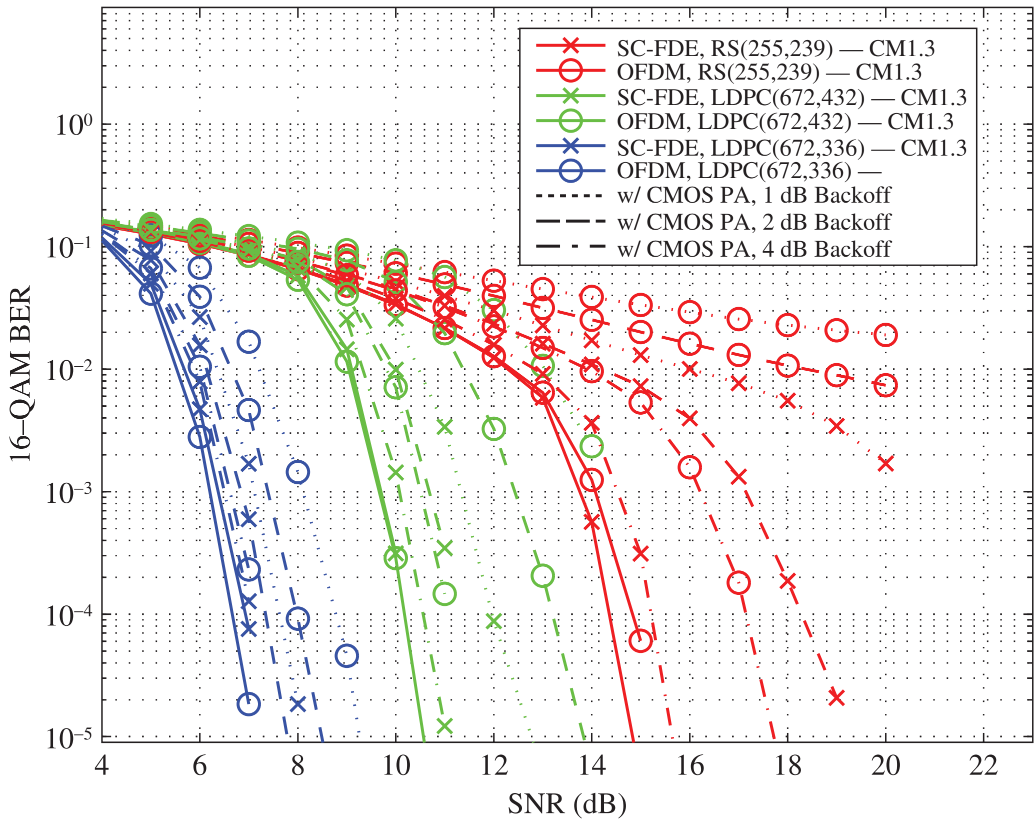

Figure 7.11 Bit error rate as a function of SNR for OFDM and SC-FDE in LOS CM1.3 channels and CMOS PA nonlinearity with 16-QAM constellations.

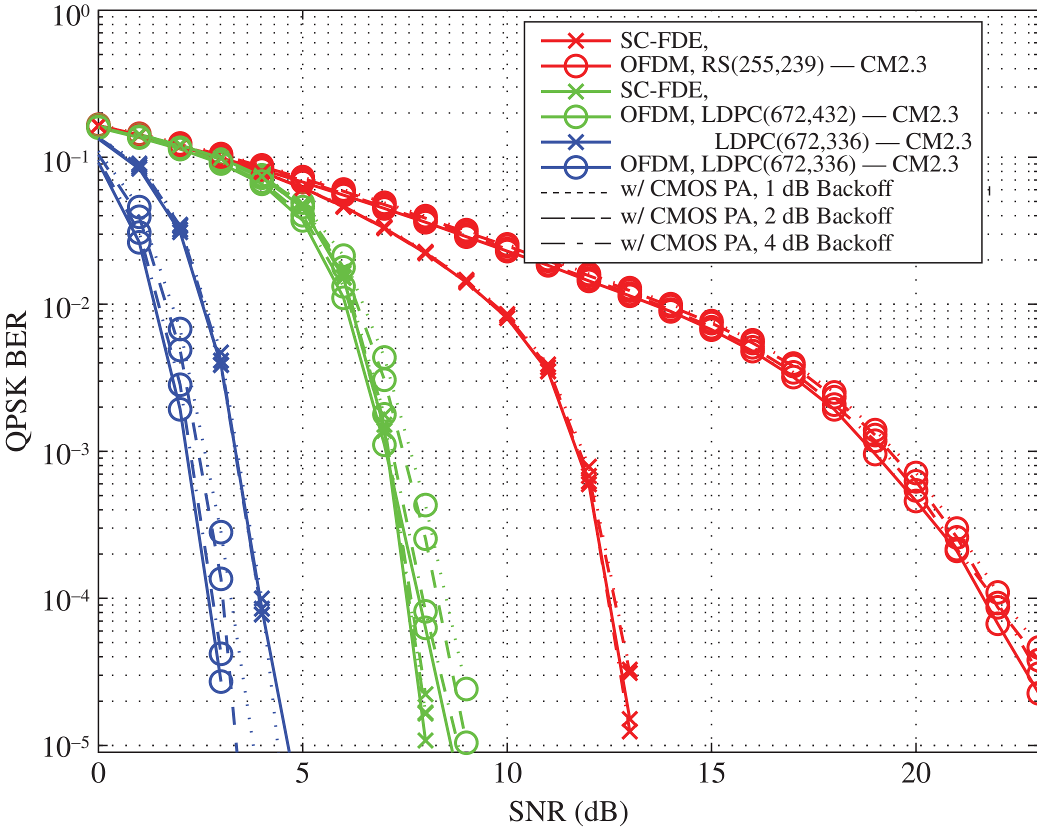

Figure 7.12 Bit error rate as a function of SNR for OFDM and SC-FDE in NLOS CM2.3 channels and CMOS PA non-linearity with QPSK constellations.

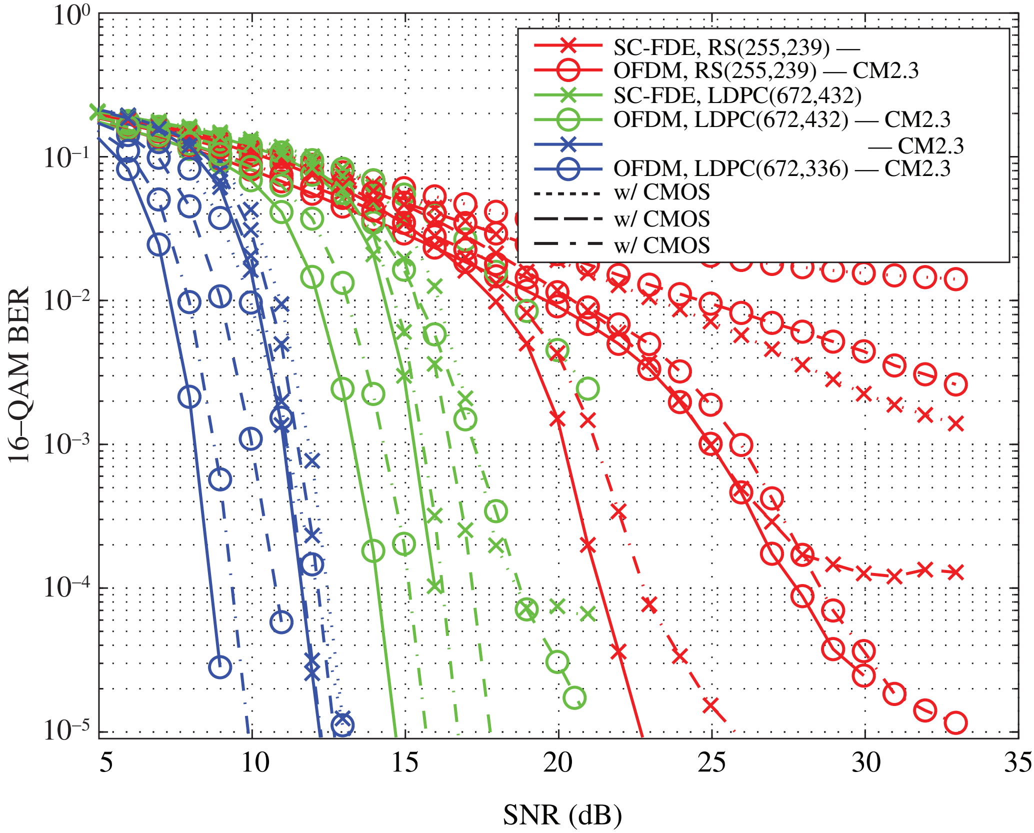

Figure 7.13 Bit error rate as a function of SNR for OFDM and SC-FDE in NLOS CM2.3 channels and CMOS PA non-linearity with 16-QAM constellations.

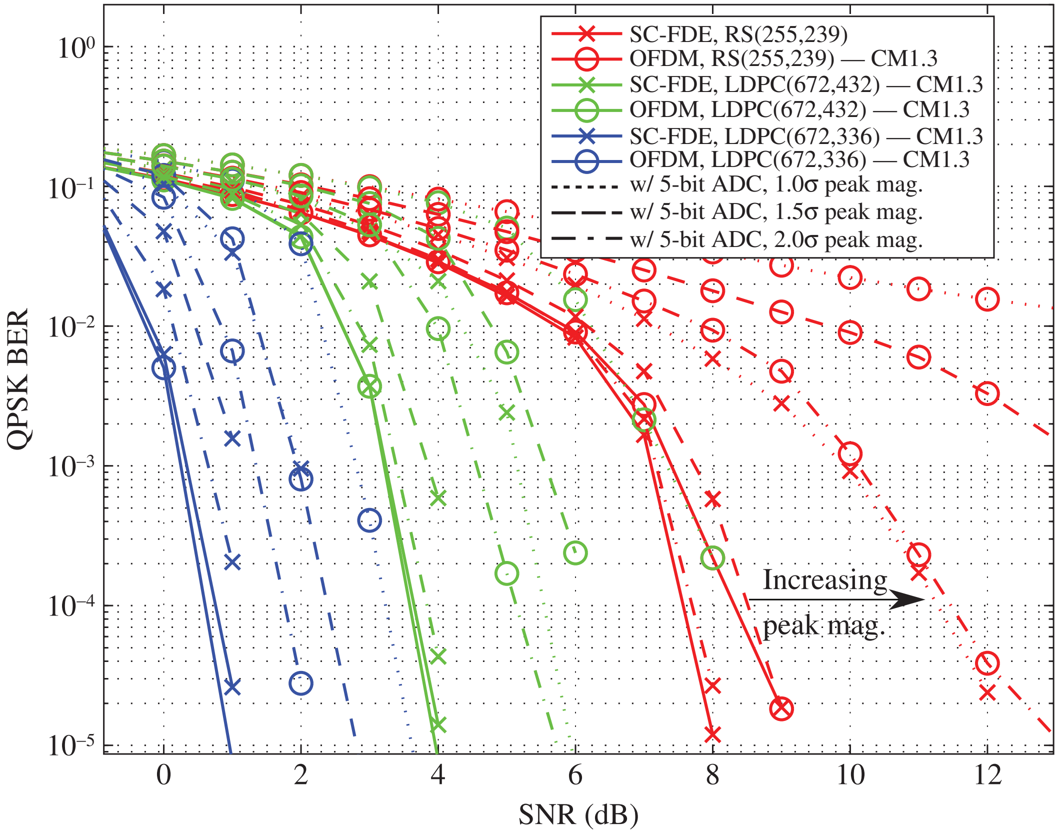

Figure 7.14 Bit error rate as a function of SNR for OFDM and SC-FDE in LOS CM1.3 channels and 5-bit ADC samples with QPSK constellations.

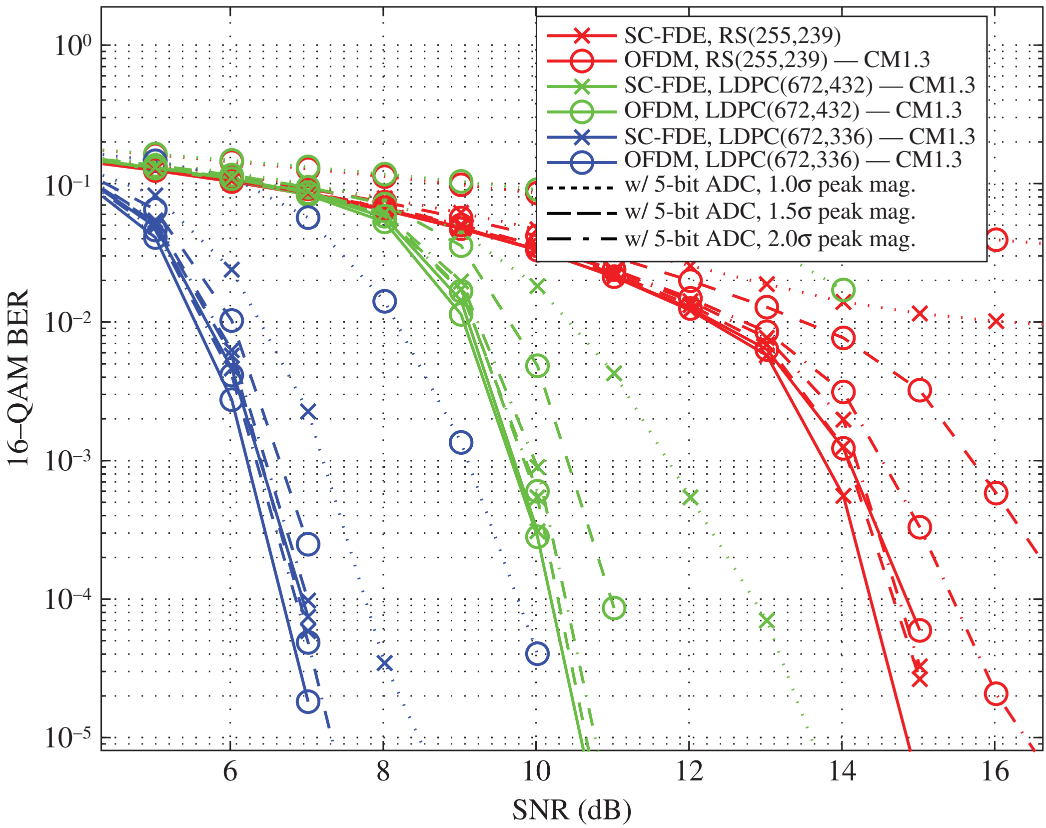

Figure 7.15 Bit error rate as a function of SNR for OFDM and SC-FDE in LOS CM1.3 channels and 5-bit ADC samples with 16-QAM constellations.

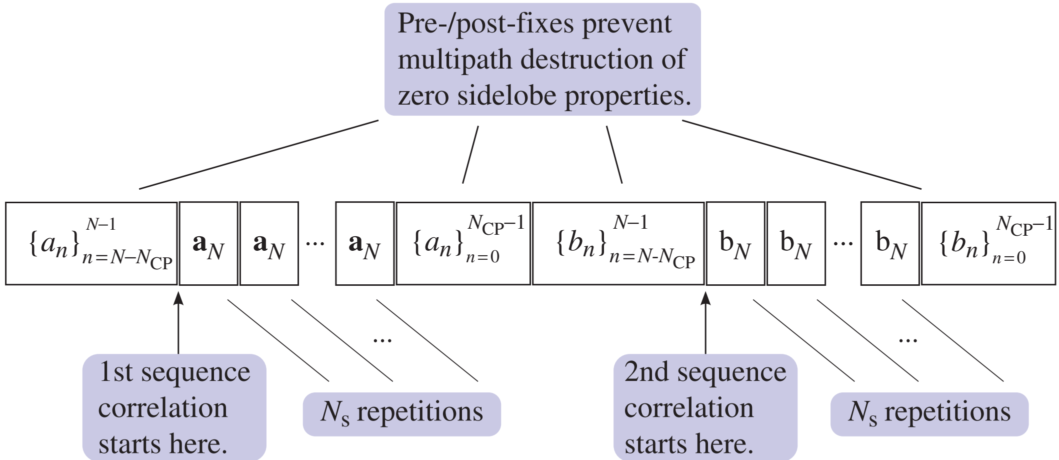

Figure 7.16 Illustration of how length-N complementary Golay sequence pair, $\mathbf{a}_N$ and $\mathbf{b}_N$, may be used to construct a training sequence that enables channel impulse response estimation through complementary correlation. Pre- and post-fixes are added before and after N_s repetitions of each complementary sequence to prevent excess multipath from disrupting zero-sidelobe properties. At the receiver we correlate with the channel distorted versions of each N-length complementary sequence and add them together to yield an estimate of a single tap. Delayed correlations are computed for each tap, and each of the N_s repetitions is used to improve estimate robustness in the presence of noise.

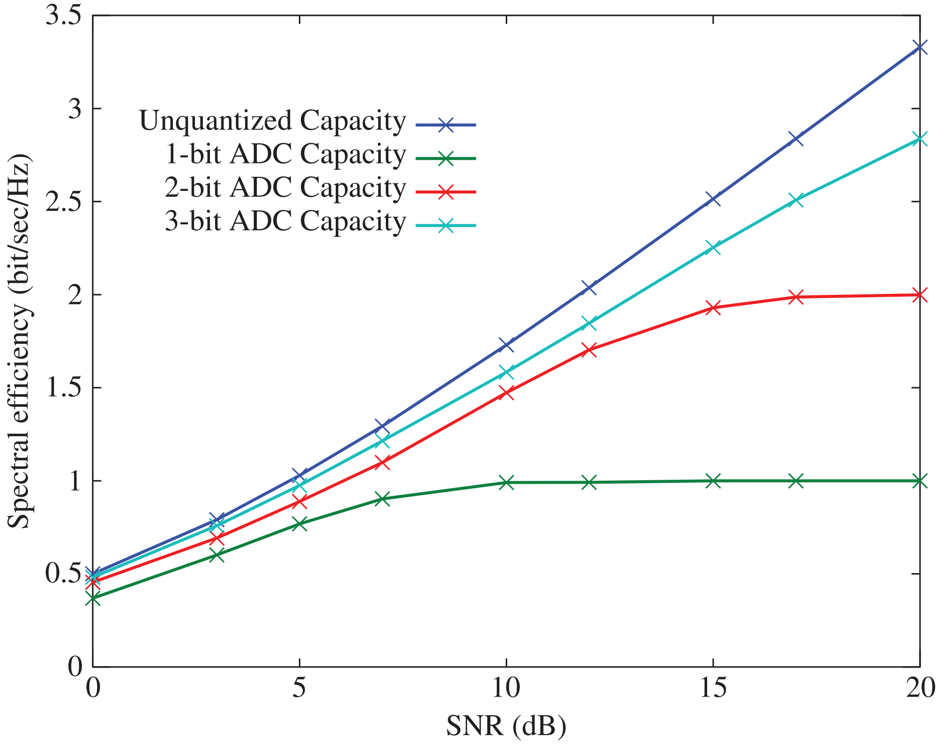

Figure 7.18 Capacity comparison with 1-, 2-, 3-, and, ∞-bit ADC precision for a discrete memoryless channel with perfect synchronization [SDM09].

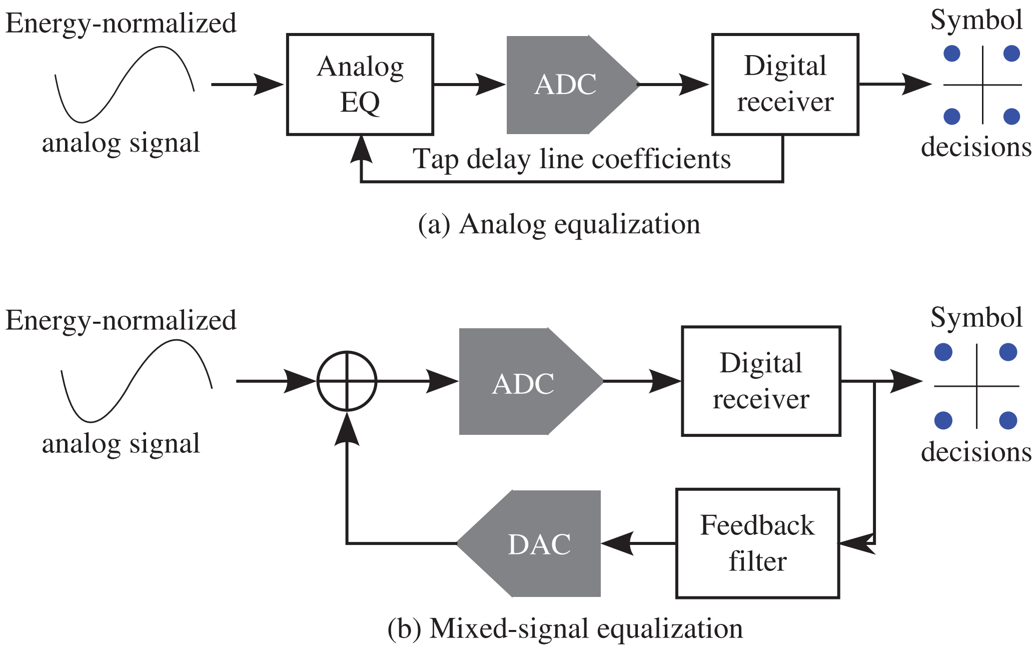

Figure 7.19 Analog and mixed signal equalization architectures can reduce the ADC bit resolution of the overall receiver (assuming that synchronization and other receiver functionality can be maintained). Mixed signal equalization can be considered a DFE with an analog feedback filter and a digital feedforward filter.

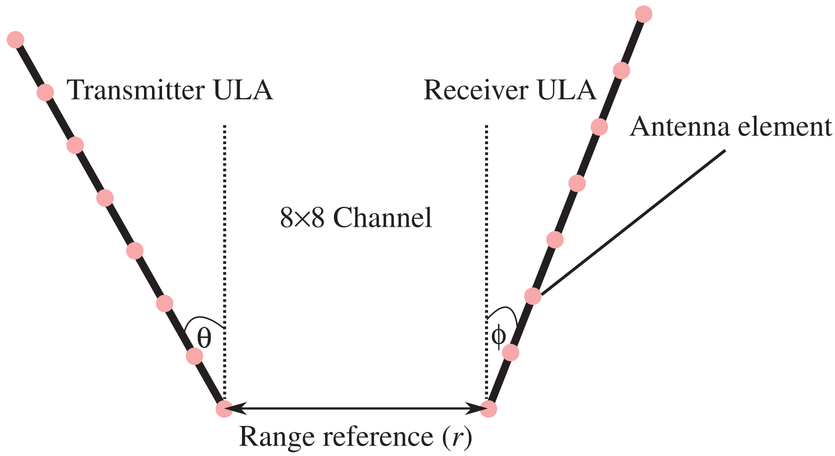

Figure 7.20 LOS MIMO channel with arbitrary uniform linear array (ULA) alignment and $N_\mathrm{r} = N_\mathrm{t} = 8$ elements on each ULA. The range reference of the link is denoted by r, and the total antenna array lengths at the receiver and transmitter are L_r and L_t, respectively.

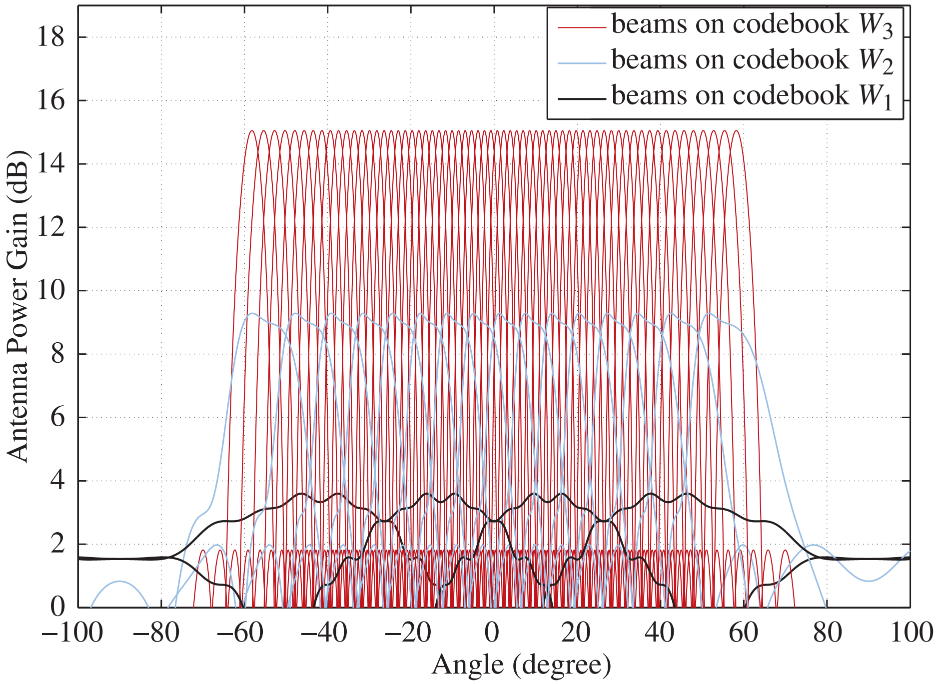

Figure 8.7 A multilevel codebook proposed in [HKL$^+$11] for wireless backhaul. Higher levels of the codebook have narrower beams, thus enhanced resolution [from [HKL$^+$11, Figure 2] © IEEE].

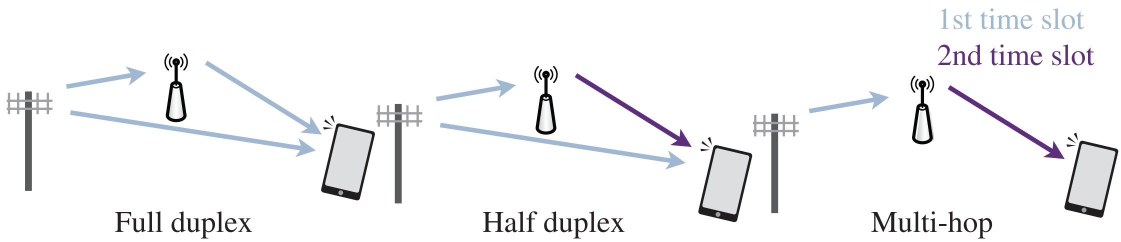

Figure 8.9 Different relay configurations with source, relay, and destination. In theory, a communication link with a relay may exploit both the direct link from the source to the destination and the indirect link through the relay. With a full duplex relay, the relay listens and retransmits at the same time. A practical example of a full duplex relay is a repeater. With a half duplex relay, the relay either transmits or receives and communication may be broken into two phases: transmission from the source, and transmission from the relay. In a multi-hop channel, the relay is half duplex and the source to destination link is not exploited (from [Hea10]).

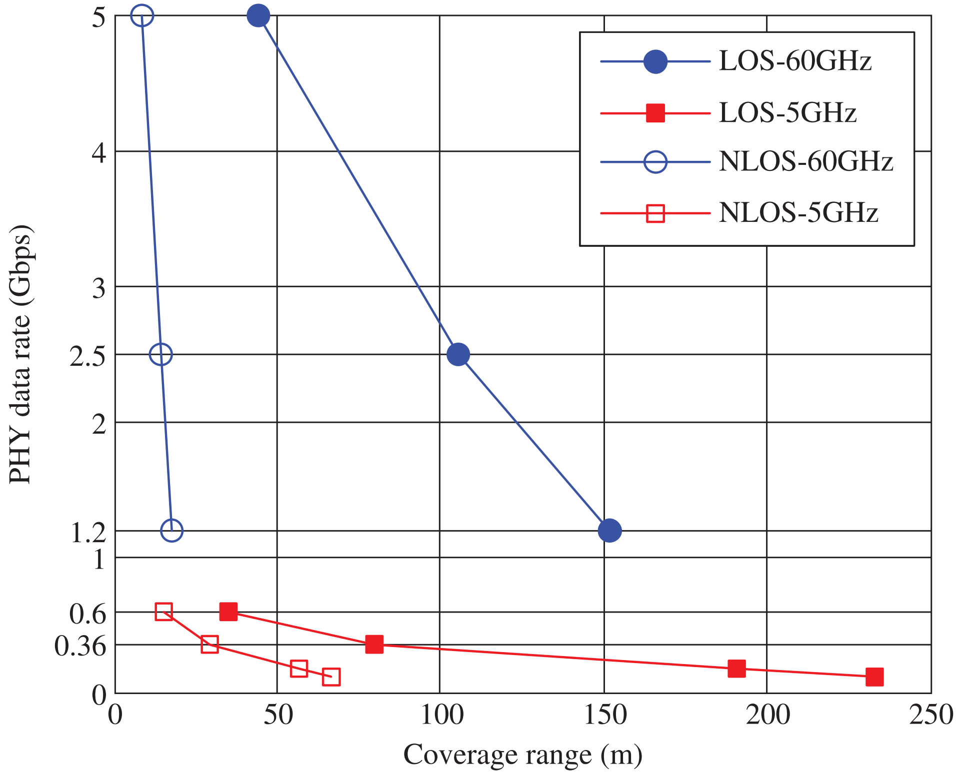

Figure 8.12 Coverage range and data rate at the physical layer for a 5 GHz link and 60 GHz link under two different channel conditions: LOS and NLOS. It can be seen that the microwave link provides higher coverage at the expense of smaller data rates. A multi-band protocol could obtain the rate benefits of 60 GHz and the coverage benefits of lower frequencies [from [YP08, Figure 1] © IEEE].

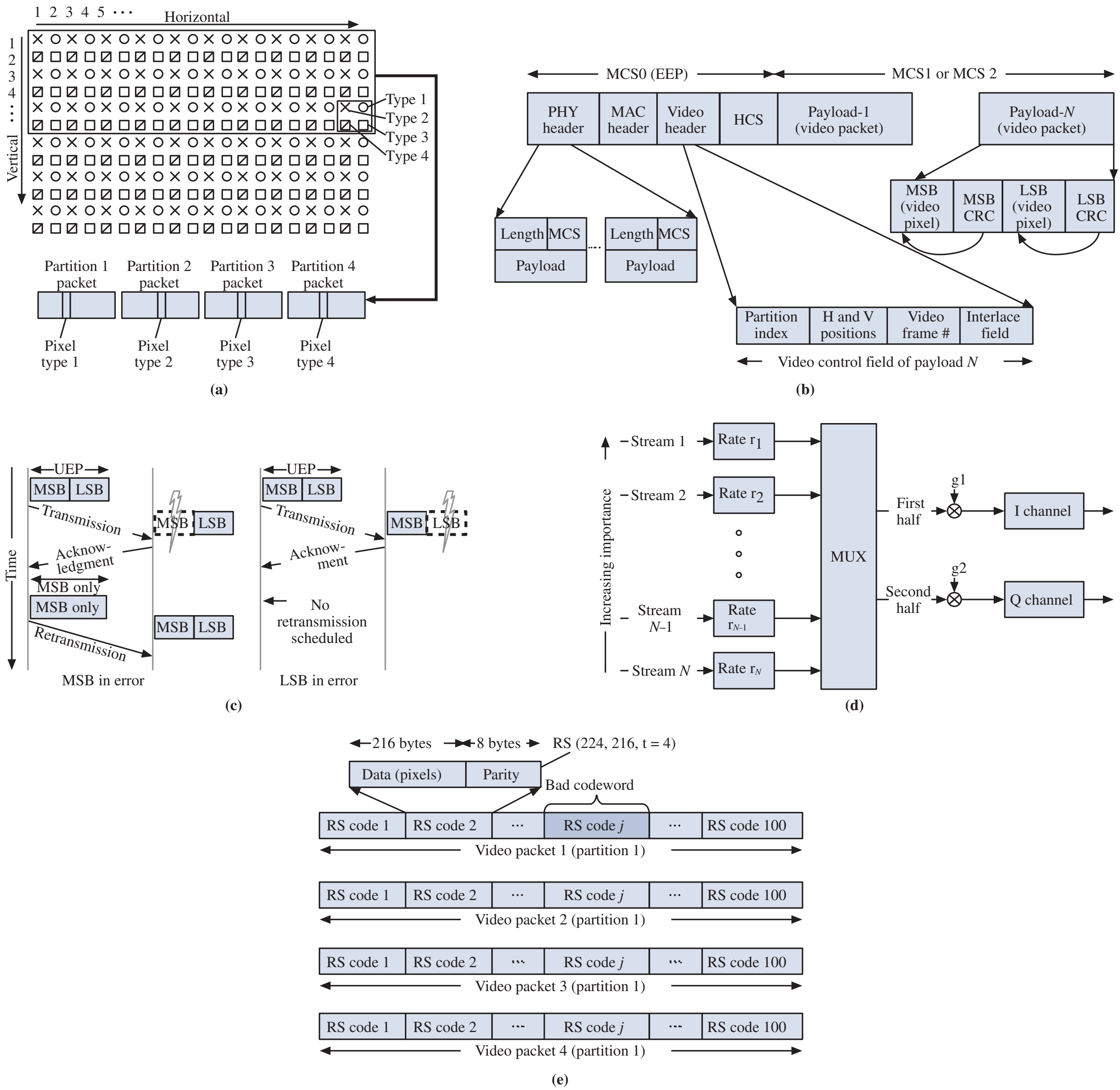

Figure 8.13 Different strategies for supporting video in mmWave systems. (a) Pixel partitioning. (b) Frame format. (c) Uncompressed video with automatic repeat request. (d) Unequal error protection. (e) Error concealment using Reed-Solomon codes. [From [SOK+08, Figure 13] © IEEE]

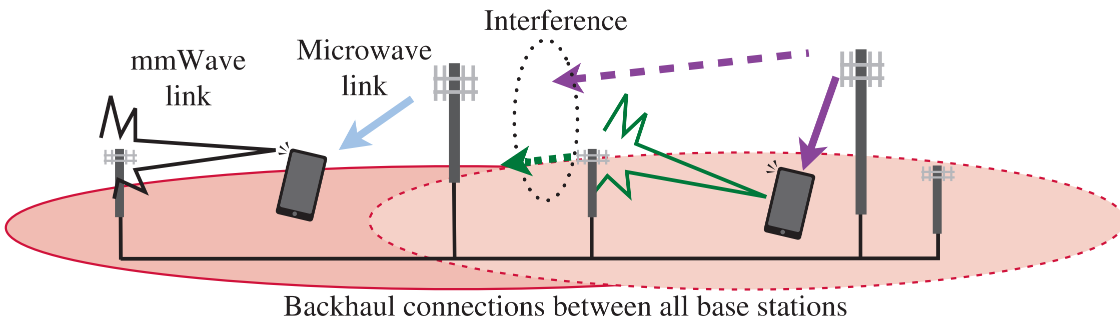

Figure 8.14 A model for coexistence between mmWave and microwave cellular where the microwave cellular network forms an umbrella network to facilitate the management of many mmWave communication links and to simplify functions like handoff. On the left side, a mobile device may connect either to a microwave or mmWave base station or to both simultaneously using the phantom cell concept. Interference on the microwave frequencies comes from other microwave base stations and on the millimeter wave frequencies from other millimeter wave small cells. As shown in Chapter 3 and elsewhere, the directionality of the beam patterns reduces the impact of mmWave interferers [BAH14][SBM92][RRE14][RRC14][ALS$^+$14].

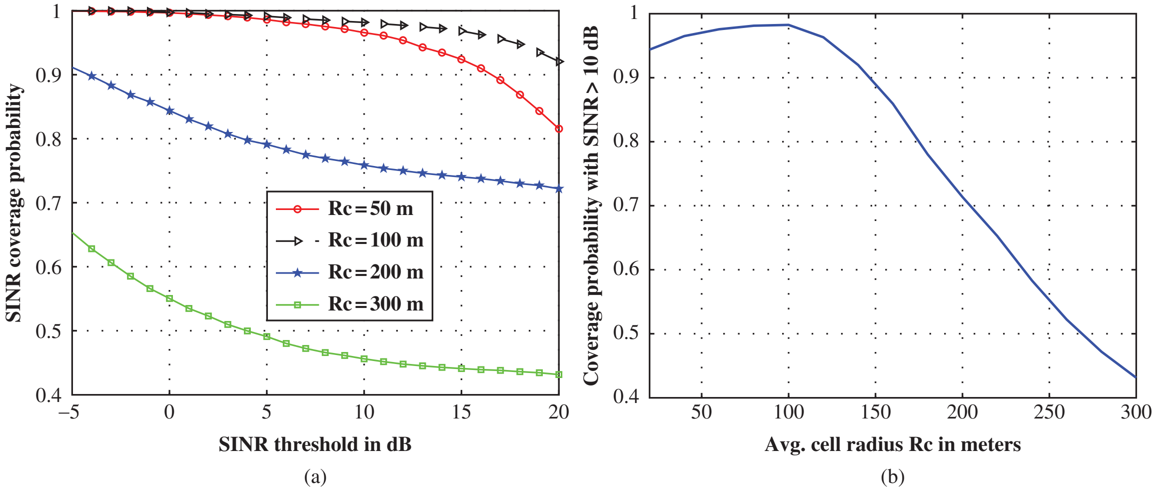

Figure 8.15 SINR coverage probability with different base station densities, where $R_c = \sqrt{1/\pi\lambda}$ and λ is the density of base stations.

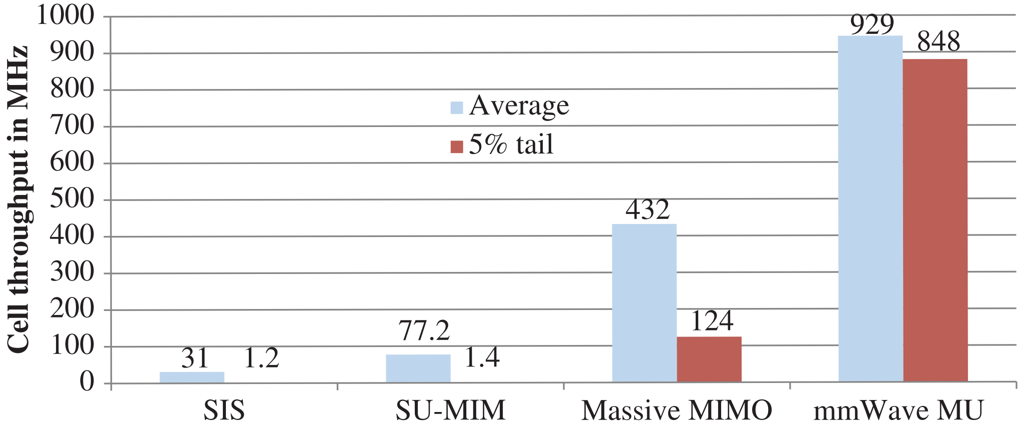

Figure 8.16 Comparison of cell throughput of mmWave networks and microwave networks.

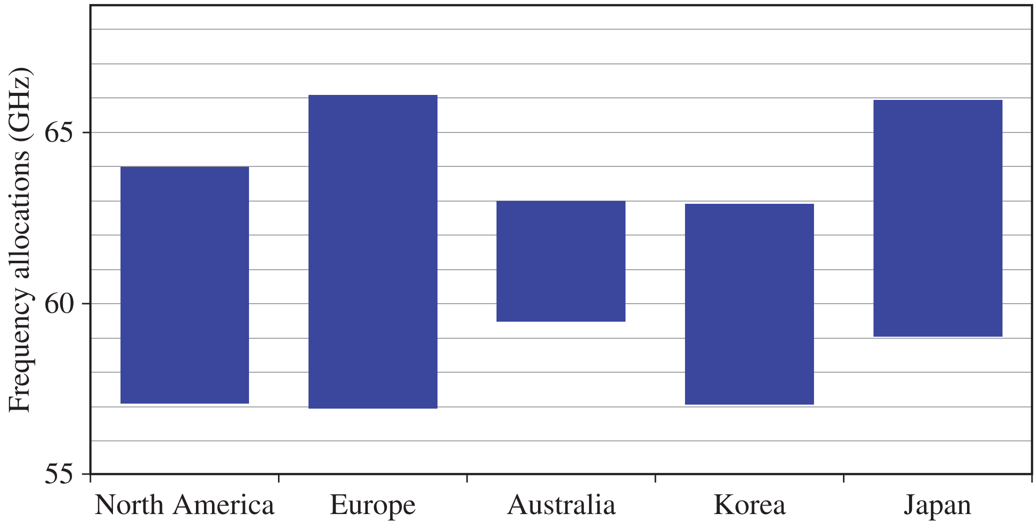

Figure 9.1 International frequency allocation for 60 GHz wireless communication systems.

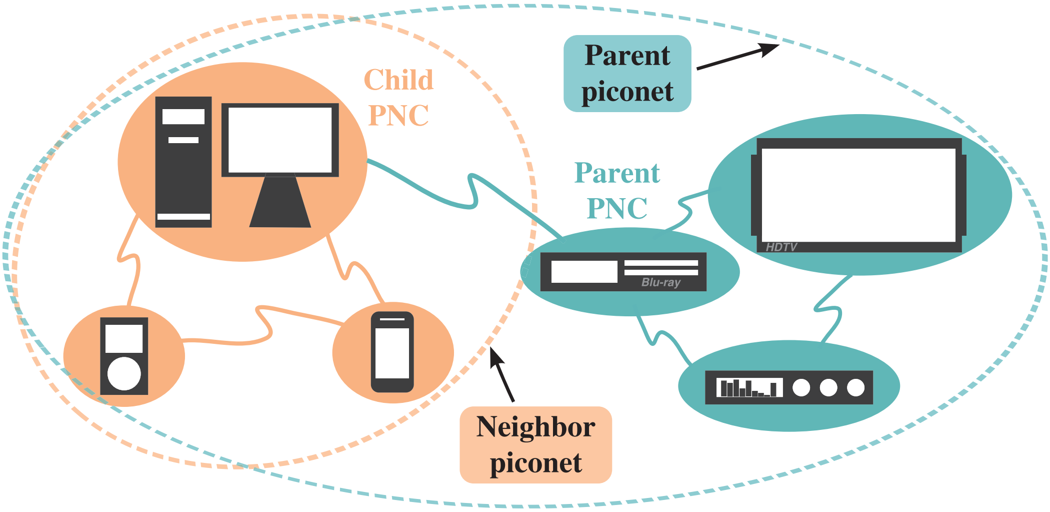

Figure 9.7 Neighbor piconet. The parent piconet (controlled by the set-top box) manages coexistence with the neighbor piconet (controlled by the personal computer).

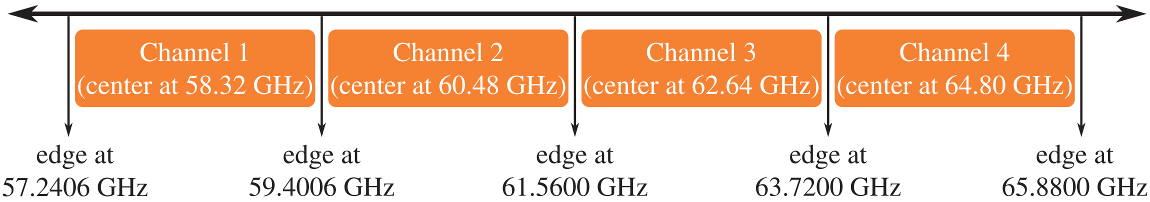

Figure 9.8 Channelization in IEEE 802.15.3c provides four different channels for mmWave PHY.

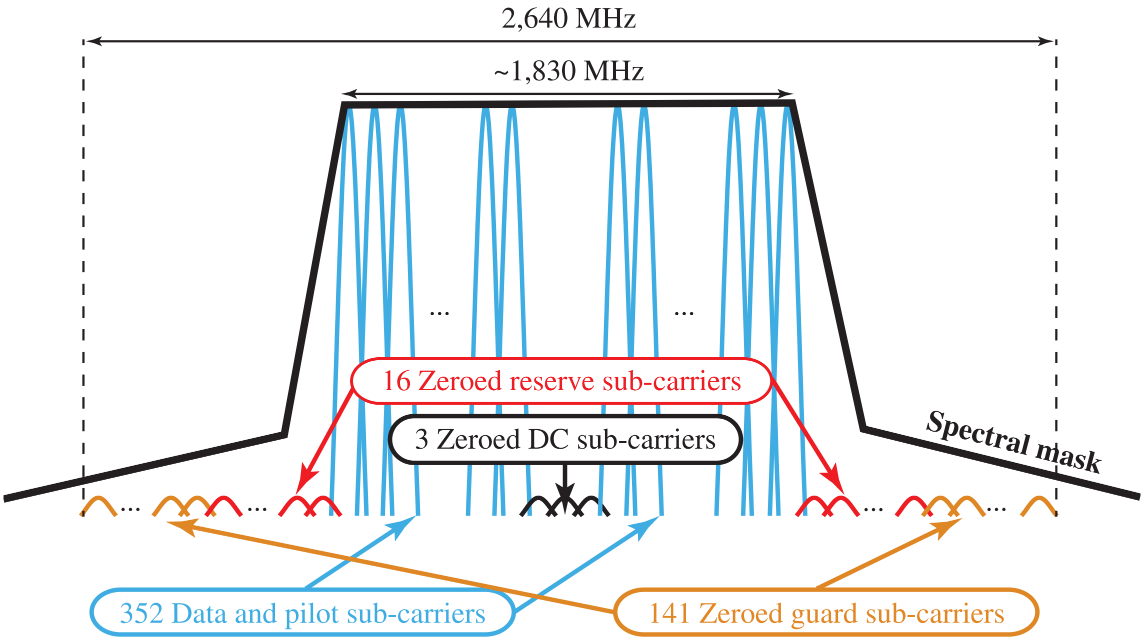

Figure 9.15 OFDM symbol formatting in the HSI PHY in IEEE 802.15.3c. The sub-carrier frequency spacing is 5.15625 MHz for all 512 sub-carriers. Three null DC tones prevent carrier feed through as well as ADC/DAC offset problems. The guard tones are usually nulled to meet spectral mask requirements, although customized guard tone values may optimize front end effects.

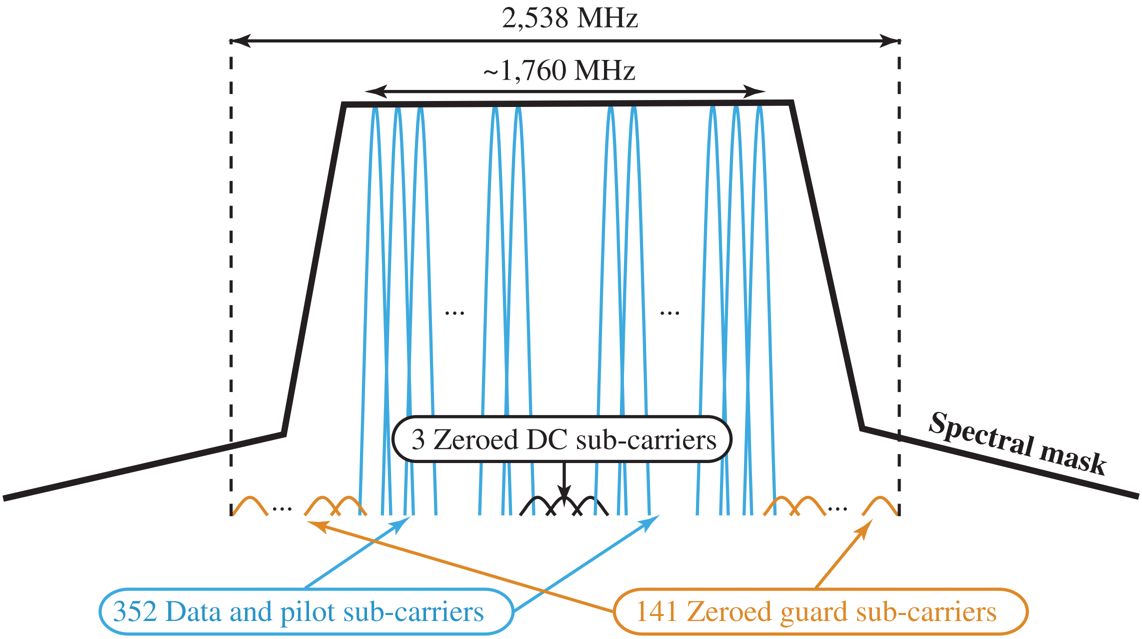

Figure 9.16 OFDM symbol formatting for the HRP. The sub-carrier frequency spacing is $\approx$ 4.96 MHz for all 512 sub-carriers. Three DC tones and all guard tones are nulled.

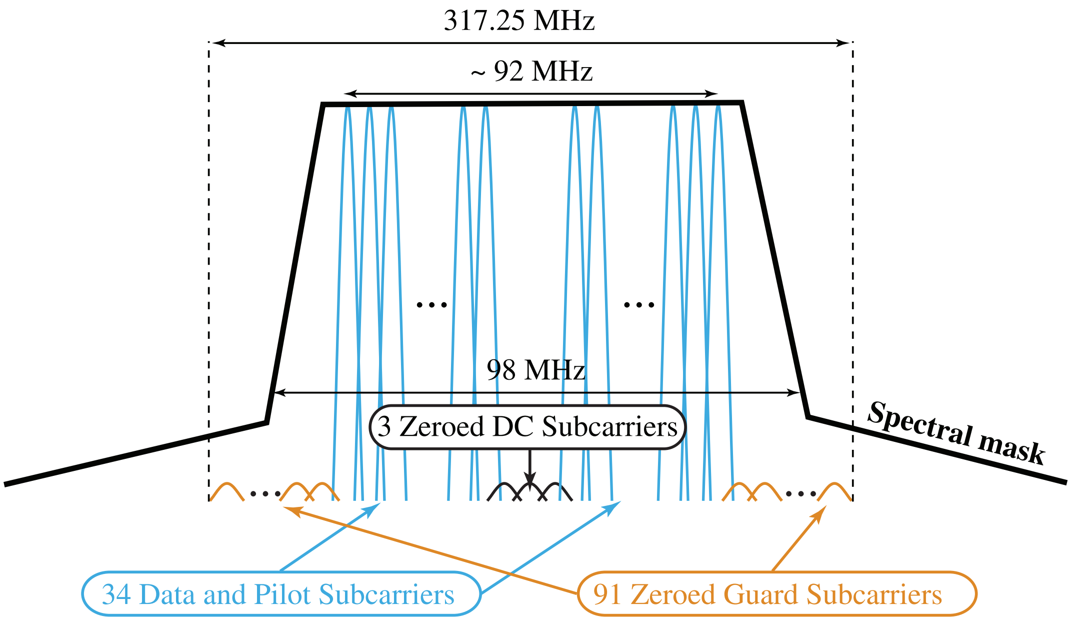

Figure 9.18 OFDM symbol formatting for the LRP. The sub-carrier frequency spacing is 2.48 MHz for all 128 sub-carriers. There are 37 data and null subcarriers, each with a subcarrier width of 2.48 MHz, resulting in an occupied bandwidth of 91.76 MHz ($\sim$ 92 MHz). The specified spectral mask passband bandwidth (at 10 dB down) is 98 MHz, allowing for roll-off in the LRP mode. Three DC tones and all guard tones are nulled.

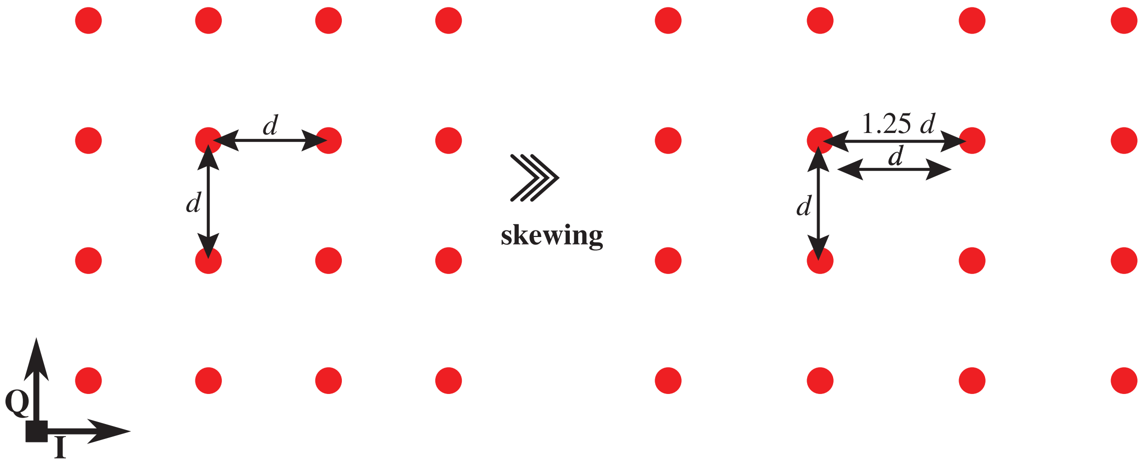

Figure 9.24 UEP Type 3 through skewing of 16-QAM. Here, the minimum distance between in-phase constellation points (where MSB bits are mapped) is increased by a factor 1.25.

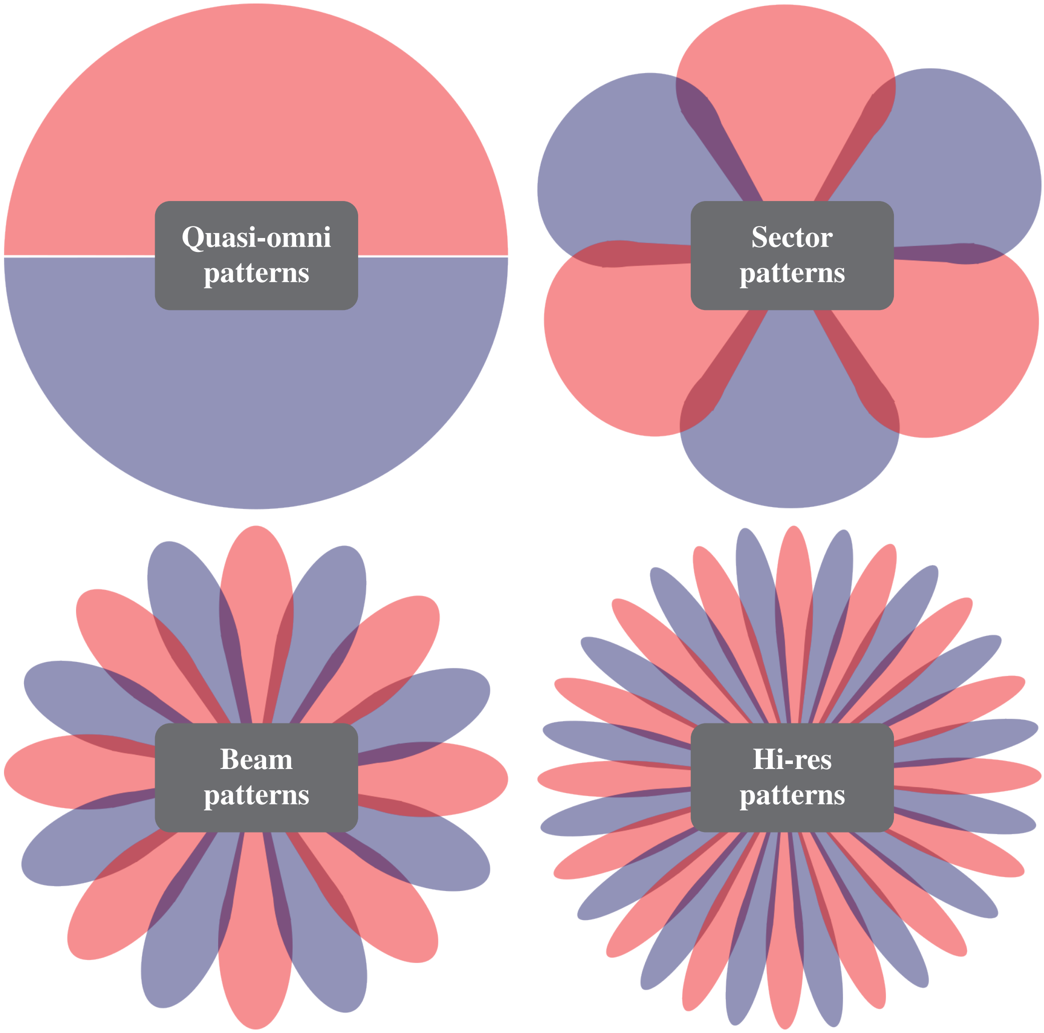

Figure 9.29 Four levels of patterns in antenna beamforming codebook for eight-element uniform linear array (patterns visualized on the azimuthal plane (top view) for a vertical array orientation) [802.15.3-09].

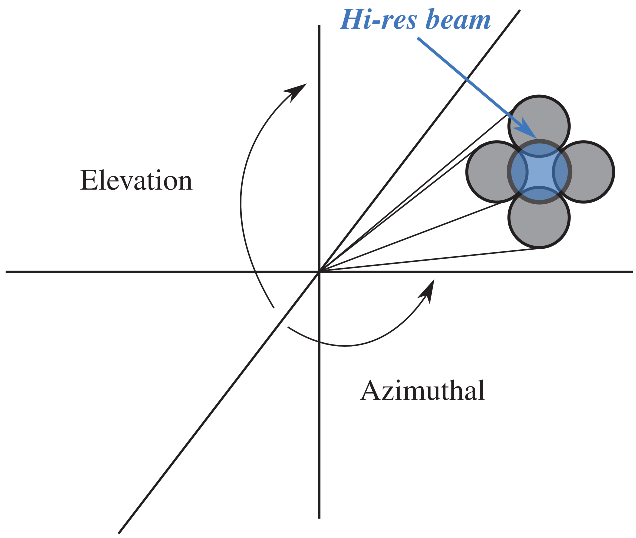

Figure 9.30 High-resolution beam cluster in 3-dimensional space.

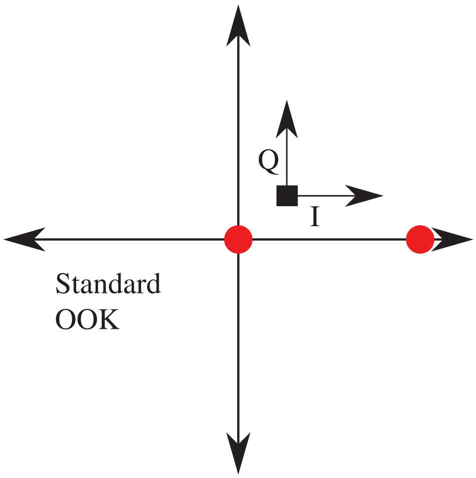

Figure 9.32 OOK and DAMI constellations for optional use within the SC-PHY [802.15.3-09].

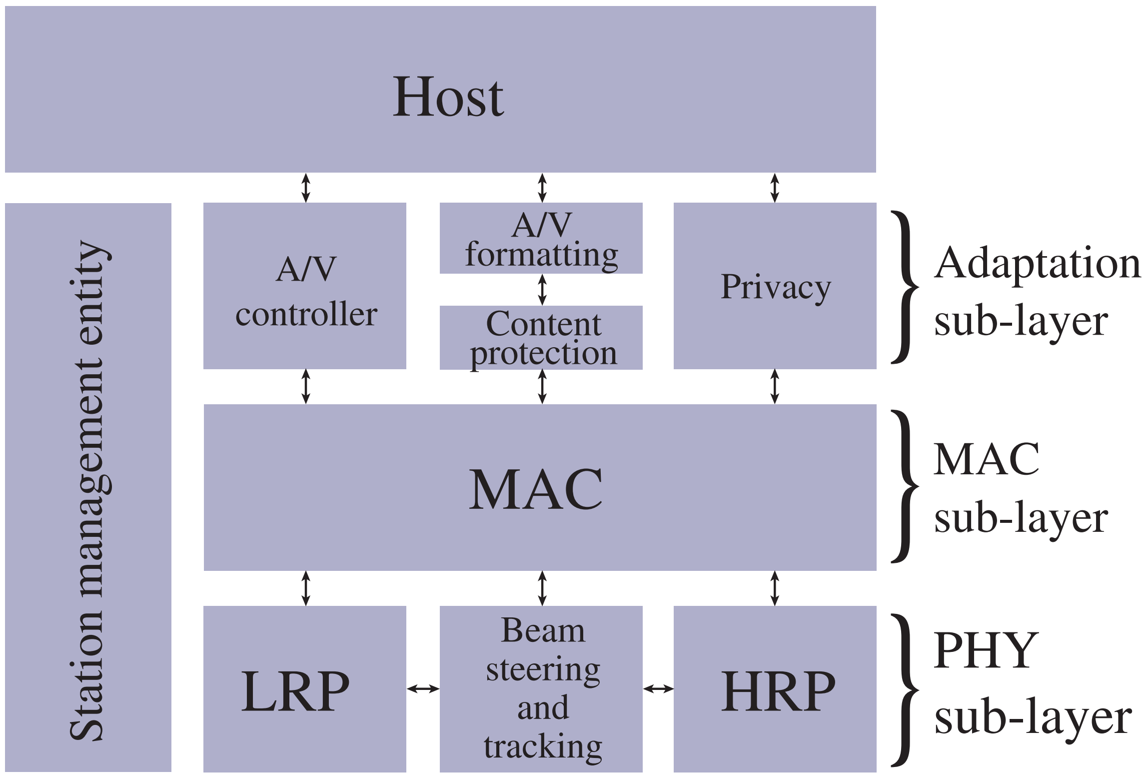

Figure 9.33 Layering of WirelessHD device.

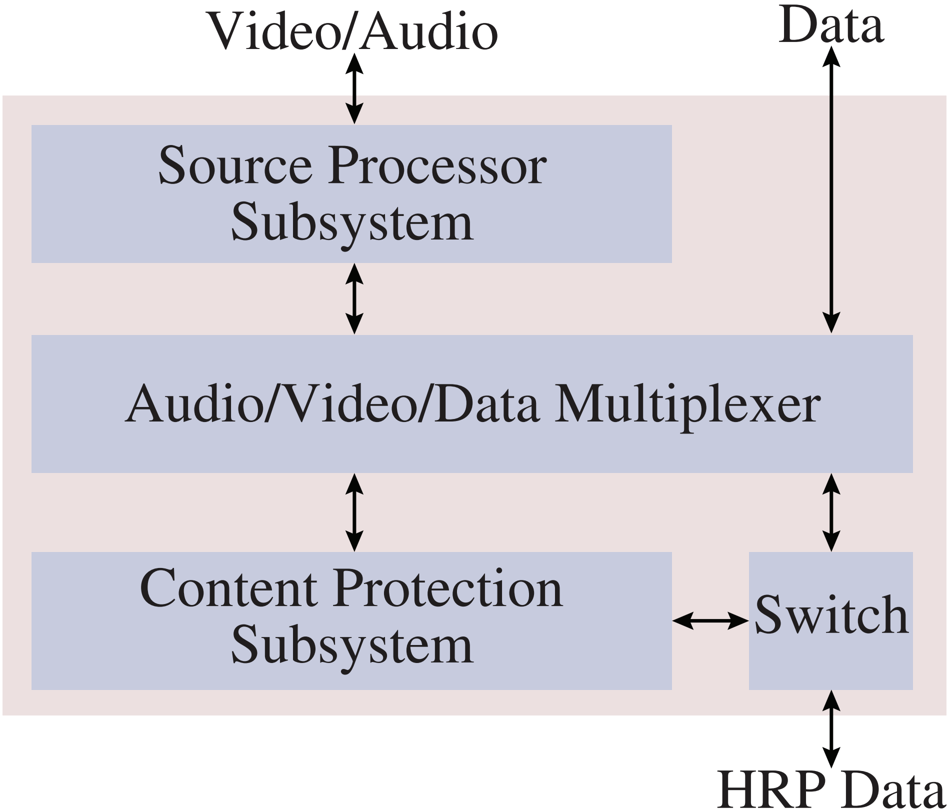

Figure 9.34 WirelessHD packetizer diagram [Wir10].

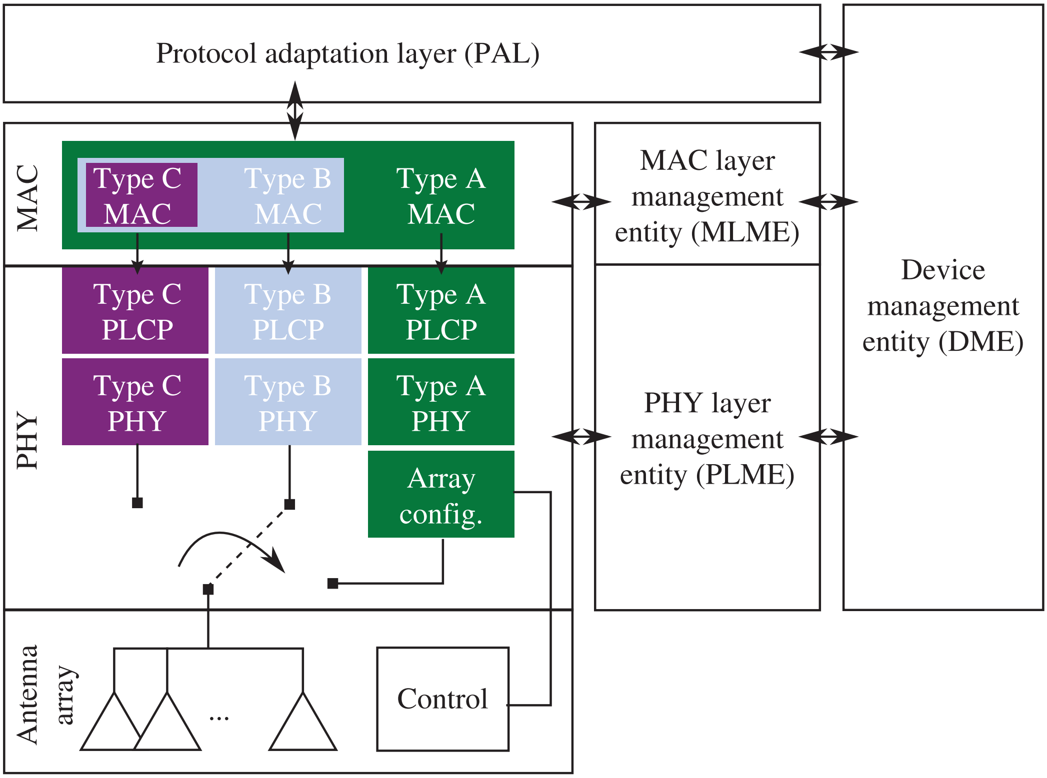

Figure 9.35 Protocol structure of ECMA-387 [ECMA08].

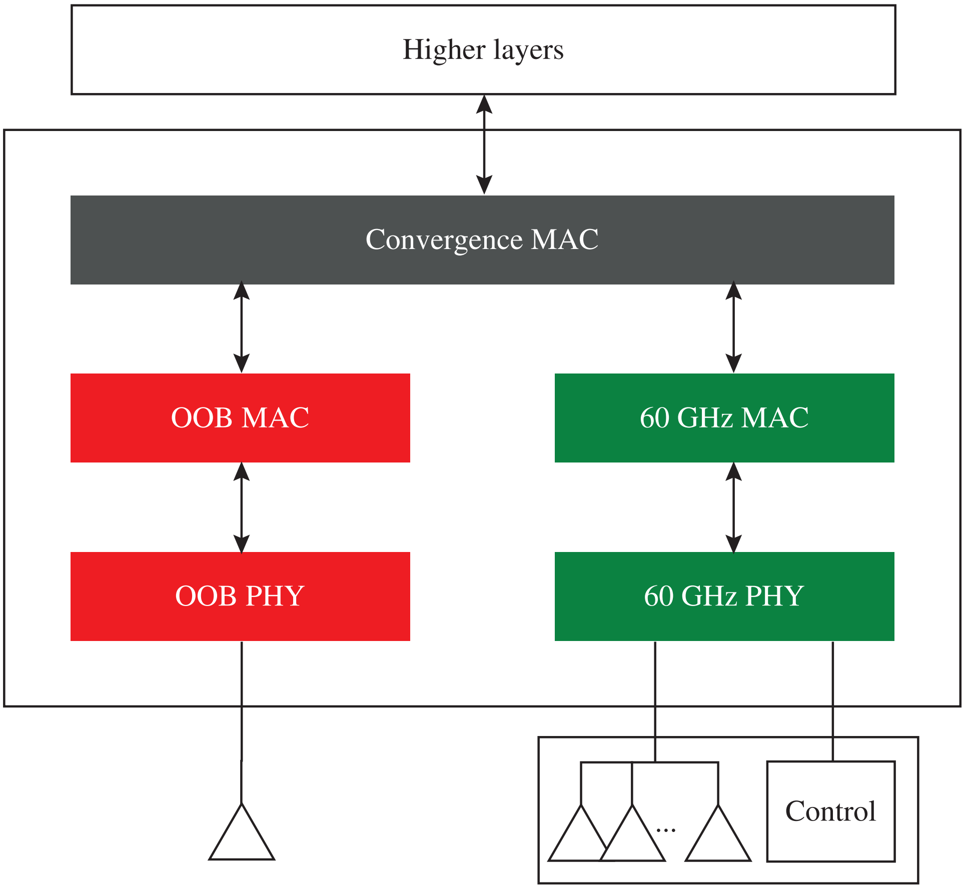

Figure 9.36 Out-out-band (OOB) control channel layered architecture in ECMA-387 [ECMA08].

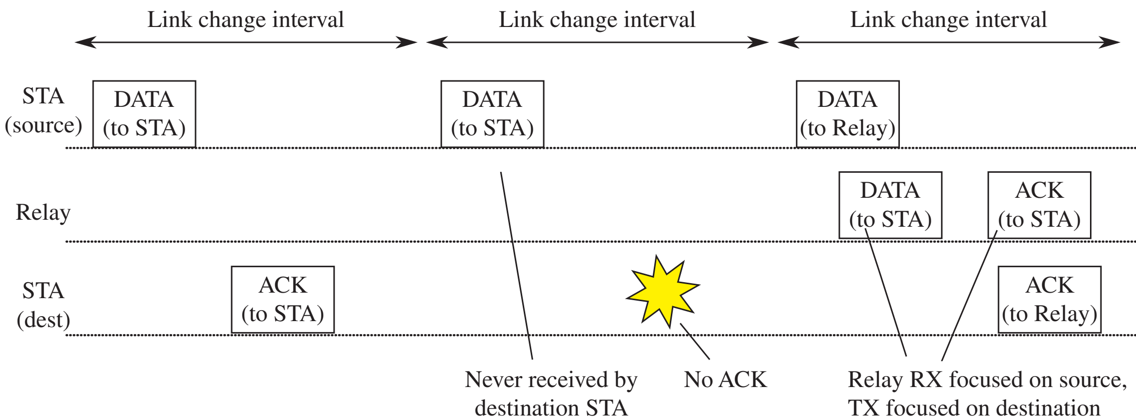

Figure 9.46 Transmissions by source STA, amplify-and-forward relay, and destination STA in a link switching example in normal mode.

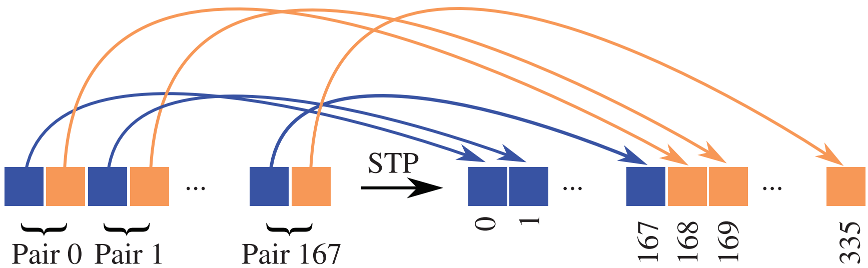

Figure 9.53 Static tone pairing (STP) in MCS 13-17. Even and odd sub-carriers are paired (out of 336 sub-carriers total) and mapped to maximize the minimum sub-carrier distance between even and odd sub-carriers (168 sub-carrier distance).

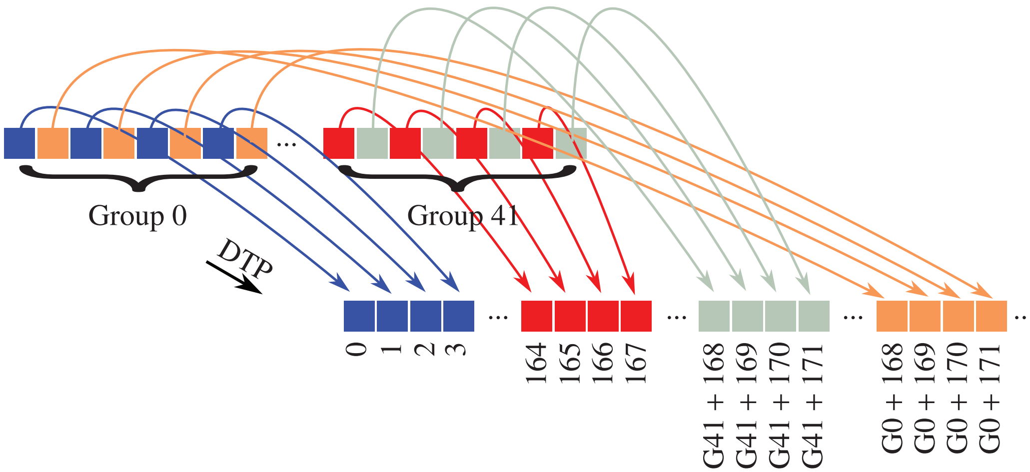

Figure 9.54 Dynamic tone pairing (DTP) in MCS 13-17. For DTP, the *group pair index* (GPI) is given to the PHY and is defined by the transmitter. The mapping GPI is hence a permutation where GPI : $\{0, 1, \ldots, 41\} \rightarrow \{0, 1, \ldots, 41\}$ and GPI : $k \mapsto G_k$. Note that although the even elements of each group have a fixed mapping, the odd elements may be mapped more generally. In other words, G_k may vary for a fixed k, depending on the link configuration. The ends of the DTP transformed sub-carriers are not shown to maintain generality, although one of the 42 groups must be mapped to the last DTP group in practice.